Direct Numerical Simulation of Transition Induced Vibration over a Flexible Hydrofoil Section

Sijo George

Sijo George. Direct Numerical Simulation of Transition Induced Vibration over a Flexible Hydrofoil Section. Fluids mechanics [physics.class-ph]. École centrale de Nantes, 2021. English. NNT : 2021ECDN0014 . tel-03267691

HAL Id: tel-03267691
https://theses.hal.science/tel-03267691

Submitted on 22 Jun 2021

THESE DE DOCTORAT DE

L'ÉCOLE CENTRALE DE NANTES

ECOLE DOCTORALE N° 602
Sciences pour l'Ingénieur
Spécialité : Mécanique des milieux fluides

Par
Sijo GEORGE

Simulation Numérique Directe de la Transition Laminaire Turbulent sur un Hydrofoil Flexible

Thèse présentée et soutenue à Nantes, le 18/02/2021
Unité de recherche : UMR6598, Laboratoire de recherche en Hydrodynamique, Énergétique et Environnement Atmosphérique (LHEEA)

Rapporteurs avant soutenance :

Elie RIVOALEN	Professeur des universités	INSA Rouen Normandie
Xavier AMANDOLESE	Maître de conférences HDR	Le CNAM, Paris

Composition du Jury :

Président :	Jacques-André ASTOLFI	Professeur des universités	École navale - IRENAV, Brest
Examinateurs :	Marie-Laure GOBERT	Maître de conférences	INSA Centre Val de Loire, Blois
	David LE TOUZÉ	Professeur des universités	École Centrale de Nantes
Dir. de thèse :	Antoine DUCOIN	Maître de conférences HDR	École Centrale de Nantes

Acknowledgements

First and foremost, praises and thanks to God, the Almighty, for showering his graces and endless blessing throughout my research work and for it's successful completion.

I would like to express my sincere gratitude to my director of the thesis Dr. Antoine Ducoin for his motivation, enthusiasm and immense knowledge. His guidance and understanding of problems helped me in all time of research and I could not have imagined having a better thesis director for my PhD study. Whenever I required any help or I was in trouble to solve my issues, you were willing to sort it out with great patience. Moreover, I have learned the human qualities of being a leader, mentor and a family man from you. I would also like to thank Prof. David le Touzé for the technical and non technical discussions related to my research activity within your busy schedule.

My sincere thanks then go to Prof. Elie Rivoalen and to Dr. Xavier Amandolese for having accepted to be my rapporteurs, as well as to Prof. David Le Touzé, Prof. Jacques-André Astolfi and Dr. Marie-Laure Gobert for having accepted to be examiners. Special thanks to Prof. Jacques-André Astolfi and Dr. Marie-Laure Gobert for reviewing my scientific papers and valuable comments.

I would like to thank Ecole Centrale de Nantes and the entire doctoral school right from accepting my Ph.D application, giving me a platform to use my knowledge and until bringing out the results and defending it. I express my sincere gratitude to my colleagues in the same office Dr. Zhenrong and Mr. Gael Clodic for the quick suggestions and support. Also, I would like to thank the IT team and administrative team of LHEEA for the technologies and facilities to carry out my research work efficiently.

Never can I forget to express gratitude to my parents and my brother. I would like to really appreciate and thank my parents for the effort and hard work they paid to bring me up until this stage. They always tried to provide the best for me to help me do better in my studies. My brother and his wife were my constant pillars of support and strength through my journey of research . Anytime I felt low, they were there to constantly build my motivation and give me strength to overcome my flaws. During my final year, I got an additional pillar to understand and provide me more support, my wife. Her positively and vibrant thinking helped me boost my energy and urge to work. She acted as my fuel of energy and helped me fight this battle of research.

Last, but not the least, I would like to express my sincere gratitude to my wife's parents, her brother and my friends especially ”malayalees” group. Their little tips,

positivity, their prayers and love helped me a lot for the completion of this research work.

Contents

List of Figures

List of Tables

Nomenclature

m	Mass of the fluid
t	Time
Ω	Fluid domain
$\partial\Omega$	Boundary of fluid domain
u, U	Velocity of the fluid
dV	Discretized volume of a domain
dS	Discretized area of domain
f_{ext}	External force such as gravity
σ	Stress tensor in fluid
p	Dynamic pressure
ν	dynamic viscosity
I	Identity matrix
Re	Reynolds number
c	Chord (m)
u_∞,U_∞	Free stream velocity of the fluid
ρ_l	Density of the fluid
ρ_s	Density of the structure
w	Mesh velocity
v, q	Test functions in Nek5000
Δt	Time step (s)
β, γ	The coefficient of temporal scheme in Nek5000
m_s	Mass of structure
$I_{xx},I_{yy},I_{zz},I_{xy},I_{yx}I_{yz},I_{zy}$	Moment of inertia in rotational frame
c_x, c_y, c_z	Damping coefficients in translation directions
D_x, D_y, D_z	Damping coefficients in rotational frame
k_x, k_y, k_z	Spring stiffness in translation directions
K_x, K_y, K_z	Spring stiffness in rotational frame
x,y,z	Displacement in translation directions
$\dot{x}, \dot{y}, \dot{z}$	Velocity in translation directions
$\ddot{x}, \ddot{y}, \ddot{z}$	Acceleration in translation directions
$\alpha_x, \alpha_y, \alpha_z$	Angle of twist in rotational directions
$\dot{\alpha}_x, \dot{\alpha}_y, \dot{\alpha}_z$	Angular velocity in rotational directions

$\ddot{\alpha}_x, \ddot{\alpha}_y, \ddot{\alpha}_z$	Angular acceleration in rotational directions
f_x, f_y, f_z	Force applied in translation directions
$T_{EAx}, T_{EAy}, T_{EAz}$	Torque applied at elastic axis in rotational frame
α	Angle of twist/attack with respect to Z-axis
$\dot{\alpha}$	Angular velocity with respect to Z-axis
$\ddot{\alpha}$	Angular acceleration with respect to Z-axis
I_α	Moment of inertia with respect to Z-axis
D_α	Rotational damping coefficient with respect to Z-axis
K_α	Rotational spring coefficient with respect to Z-axis
T_{EA}	Torque applied at elastic axis with respect to Z-axis
EA,ea	Elastic axis
D	Diameter of the cylinder
H	Cross sectional height of the computational domain
E	Elasticity of the structure
U_R	Reduced velocity
A	Amplitude ratio
M	Mass ratio
S_T	Stokes number
T	Time bar
C_Y	Cauchy number
f_N	Natural frequency
f_s	Shedding frequency
F	Frequency ratio
ϕ	Modal shape of the motion
f_{st}	Standard force from fluid
m_a	Added mass
f_g	Base force from unsteady stokes
$\overline{m}_a$	Artificial added mass
n	Time step number
τ	Correction factor
u_{st}	Standard velocity from NS updated
p_{st}	Standard pressure from NS updated
u_g	Base velocity from unsteady stokes
p_g	Base pressure from unsteady stokes
$\hat{n}$	Unit normal to the surface of the object
Γ	Diffusivity parameter
u_D	Deformation velocity coefficient
V_{min}	Volume of the smallest element in the whole domain

V_{max}	Volume of largest element in the whole domain
V^e	Volume of current element
η	Normal distance from surface of the body to grid points
η_{mid}	Mid point of the slope
Δ	Slope required for the blending function
ω_s	$2 \times \pi \times f_s$
C_L	Coefficient of lift
C_D	Coefficient of drag
C_P	Coefficient of pressure fluctuation
C'_P	Coefficient of pressure
C_f	Coefficient of friction
C_M	Coefficient of moment
C'_L	Fluctuation of lift coefficient
C'_D	Fluctuation of drag coefficient
N	order of spectral element
ω_z	Vorticity in Z-direction
F_N	Reduced natural frequency
t_o	Time period of oscillation of the object
t_{shed}	Time period of vortex shedding
$\dot{\alpha}*$	Non dimensional pitching velocity
A_θ	Non dimensional pitching amplitude
θ_{sep}	Momentum thickness
$\dot{\alpha}$	Angular velocity
α	Angle of attack or Angle of twist
N_{crit}	Value indicates the free flow turbulence
$t_{TS(Exp)}$	Time period of TS waves from experiment
$f_{TS(Exp)}$	Frequency of TS waves from experiment
t_{TS}	Time period of TS waves from static DNS
f_{TS}	Frequency of TS waves from static DNS
H	Shape coefficient
$\tilde{m}_a$	Analytical solution of added mass
a	Distance between the centre of pressure and elastic axis
λ_z	Span-wise width of Λ structure
δ_d	Displacement thickness (δ_d)
$\Delta x^+_{min}, \Delta y^+_{min}, \Delta z^+_{min}$	The mesh resolution parameters in X, Y and Z directions
I_{corr}	Correction inertia for extra added mass
λ_z	Span-wise width of Hair-pin (Λ) structure
I'_α	Moment of inertia with respect to Z-axis (2-D)

D'_α	Rotational damping coefficient with respect to Z-axis (2-D)
K'_α	Rotational spring coefficient with respect to Z-axis (2-D)
T'_{EA}	Torque applied at elastic axis with respect to Z-axis (2-D)
ζ_α	Damping coefficient
$\dot{\alpha}^*_{(max)}$	Maximum of non-dimensional pitching velocity
$A_{\theta(max)}$	Maximum of non-dimensional pitch angle

List of Symbols

DNS	Direct Numerical Simulation
LES	Large Eddy Simulation
ILES	Implicit Large Eddy Simulation
FEM	Finite Element Method
FVM	Finite Volume Method
FDM	Finite Difference Method
N-S	Navier Stokes
BDF	Backward differentiation Formula
DOF	Degree of Freedom
CFD	Computational Fluid Dynamics
FEA	Finite Element Analysis
FSI	Fluid Structure Interaction
CSS	Conventional Seriel Staggered
ISS	Improved Seriel Staggered
CPS	Conventional Parallel Staggered
IPS	Improved Parallel Staggered
ALE	Arbitrary Lagrangian-Eulerian
VIV	Vortex Induced Vibration
LCO	Limit Cycle Oscillation
LDV	Laser Doppler Velocimetry
EOM	Equation of Motion
URANS	Unsteady Reynolds Averaged Navier Stokes
TS	Tollmien-Schlichting
LSB	Laminar Seperation Bubble

Introduction

Maritime transportation is the main mode of handling freights internationally. Enormous transportation requirements around the world are facilitated through the operation of thousands of ships on a daily basis and it is responsible for 2-3% of global greenhouse gas emissions. Marine propellers are one of the key components of the ships, as it is used to produce thrust. The Fig. 1 shows a 4 blade marine propeller attached to a ship.

FIGURE 1: Propeller of a Ship (The picture is taken from `https://www.marineinsight.com/`

Currently, there are many researches conducted on the development of advanced marine propellers, with sensors, electric drive, flexible and composite blades. The conventional marine propellers are commonly made of Steel or Nickel-Aluminum-Bronze (NAB) or Manganese-Nickel-Aluminum-Bronze (MAB) (Liu and Young, 2009, Young, 2008). The alloys of these materials protect the propellers from corrosion, erosion due to cavitation and the environmental conditions imposed by the sea. The improvements in the field of computational fluid dynamics and experimental techniques provides a promising outlook, for the design of optimised lifting profiles in terms of performance and durability. The recent developments in flexible and lighter materials has attracted marine industries to manufacture composite propellers. These flexible marine propellers can be designed to deliver higher performance in comparison to the conventional propellers, by using the fluid structure interaction to obtain passive control of deformations under steady and unsteady loads (Motley and Young, 2011,Young, 2008, Pernod et al., 2019, Young, 2008, Pluciński et al., 2007,Lin et al., 2009, Andersen et al., 2009). The angle of attack of propellers can be adjusted with respect to the flow conditions using their flexibility. The propeller blades must be strong enough to withstand the thrust generated and the vibratory force arises due to the unsteady flow fields. The presence of transitional regimes can negatively affect the performance of the propellers and control surfaces. For instance, propellers on vehicles such as AUV's (Autonomous Under water Vehicles), small boats, or lab scale marine propellers lies at relatively moderate Reynolds numbers ($100,000 < Re < 1,000,000$) and transitional regimes may appear.

In order to study the the boundary layer flow over propellers, hydrofoils are often considered. It allows to investigate the fundamentals of flow regimes around a propeller's section, without considering factors such as 3D flow developing along the surface, tip vortex of the propeller, cross flow due to rotation etc. Therefore, the hydrofoils are widely used in experimental and numerical setups to study academically the hydrodynamic characteristics of marine propellers. The Fig.2 shows one blade from the Carlton propeller book (Carlton, 2012) with different regimes of fluid flow along the blade.

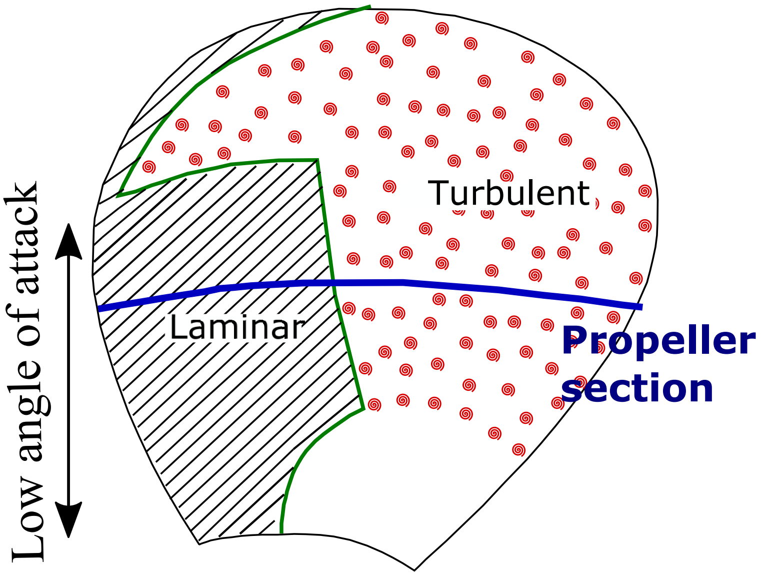

FIGURE 2: Typical boundary layer regime on a propeller blade, inspired by Carlton (Carlton, 2012)

The green line represents the laminar to turbulent transition point along the propeller blade whereas the blue line shows the cross-section of a hydrofoil in which the transition happens at about the mid of the chord. It is well known that the laminar to turbulent transition is often induced by laminar separation bubble (LSB). LSB is a laminar separated flow region that develops due to an adverse pressure gradient, which is then followed by turbulent reattachment (O'Meara and Mueller, 1987). The Fig. 3 shows the sectionnal view of a laminar separation bubble. The flow is approximately divided into two regions by a dividing stream line. The first region is enclosed in between the airfoil surface and stream line $ST'R$. This region shows the re-circulating region of the flow and core of the bubble. The second region is the flow in between $S''T''R''$ and $ST'R$. It consists of separated shear layer flow which undergoes transition due to the unstable laminar shear layer. The transition happens at location T which is close to the core of the LSB. Later, the flow is re-attached due to the momentum transfer. In some cases the effect of free-stream turbulence can cause the disappearance of LSB and leads to by-pass transition. This phenomena can also be applied to laminar propeller blades. The laminar propeller blades are designed by shifting the maximum thickness near the centre of the chord. This, in turn, delays the adverse pressure gradient acting over the section and increases the critical Reynolds number for transition. In airfoils, the transition comprises of a large portion of the chord and dominates the boundary layer flow.

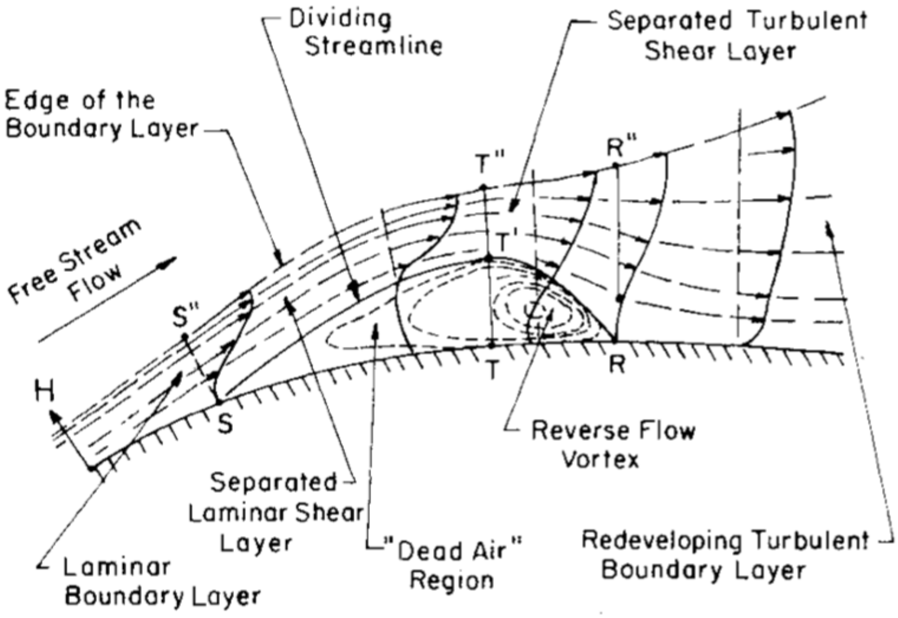

FIGURE 3: A section view of laminar separation bubble over an airfoil, O'Meara and Mueller, 1987

The Fig.4 shows the pressure contours with coherent structures along the chord at Re =450, 000 over a NACA66 hydrofoil, which is taken from a laminar propeller blade. The LSB induces strong, periodic vortex shedding, which induces the transition to turbulent. Moreover, Ducoin et al., 2012 observed that the transitional boundary layer induces some vibrations due to the strong periodic vortex shedding/ TS waves and affects the hydrodynamic efficiency of the hydrofoil.

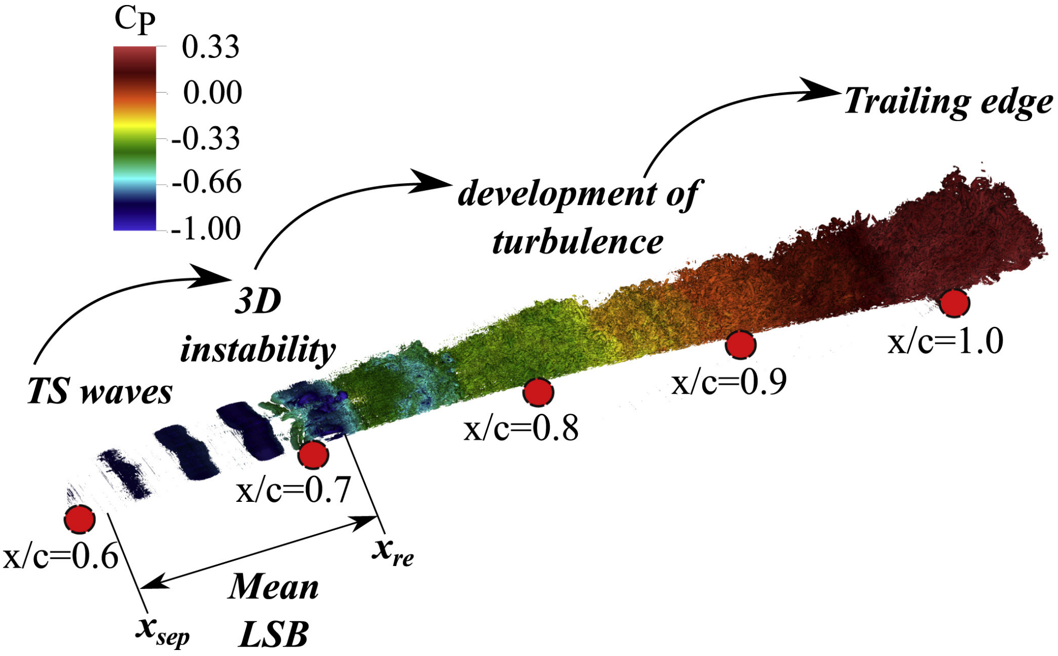

FIGURE 4: Coherent structures downstream of the LSB, iso surface of λ_2 coloured with pressure coefficient, Re = 450,000 over NACA6612 hydrofoil, Ducoin and Astolfi, 2019

With regards to hydroelastic applications, few studies have addressed the prediction and impact of transitional flows on flexible hydrofoils, in particular when Reynolds number is relatively high , i.e. around lab scale propellers Reynolds number (300,000 to 1,000,000). To the authors' knowledge, no numerical studies have addressed fully resolved transition-induced vibration over hydrofoils. Hydroelasticity of lighter materials can be more challenging to simulate than aeroelasticity due to the added mass, which classically causes numerical instability. It should be noted that many of the aeroelastic problems are mostly based on large aspect ratio or more flexible wings, leading to larger deformations and/or lower frequency oscillations. In marine propeller problems, the structure is more rigid and characterised by a vibratory response, i.e. at higher frequency oscillations (due to higher Reynolds numbers) with low amplitude deformations.

The present study is motivated by an experimental work done by Ducoin et al., 2012 at relatively high Reynolds numbers on a NACA6612 hydrofoil section. Fig.5, published in Journal of Fluids and Structures (JFS) in 2012, shows the effect of transition on the hydrofoil's vibrations: as Reynolds number increases, the transition frequency approaches the fourth mode (second torsional natural frequency) of the hydrofoil, and induces a possible fluid structure interaction problem. Moreover, the transition associated with wall pressure fluctuations induced by TS waves in the transition region, has been identified to a local single frequency. However, the hydrofoil's vibration seems to induce multi-scaled frequency components of the transition, which were not clearly characterized in the experimental study due to a lack of boundary layer flow measurements..

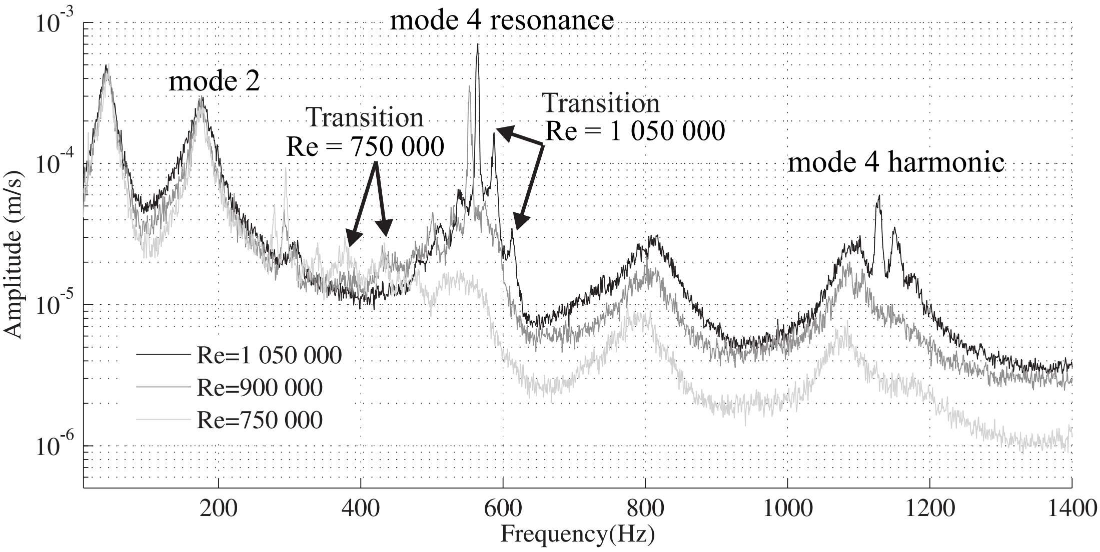

FIGURE 5: Comparison of flexible hydrofoil velocity spectra for $\alpha = 4°$ and various Reynolds numbers, Ducoin et al., 2012

Hence, it appears that experiments have limitations in extracting the transitional boundary layer flow from a very localized transitional region, which is submitted to small amplitudes oscillations at the surface. Similarly engineering numerical methods mostly based on RANS based codes do not capture unsteady transition mechanism and boundary layer regime accurately especially when the foil is likely to vibrate according to the hydrodynamic instabilities. Therefore, Direct Numerical Simulation (DNS) seems necessary to capture/ reproduce the transition induced vibration over flexible hydrofoils. Following this experimental work, a DNS was carried out by Ducoin and Astolfi, 2019 on a rigid NACA66 hydrofoil at a Reynolds number of 450, 000. The unsteady wall pressure fluctuations in the transition region were validated with measurements, and the mechanism of transition was investigated in detail.

Therefore, the objective of the current study is to develop an efficient coupling method and investigate the change in pressure distribution due to the small amplitude oscillations. Furthermore, this study aims at highlighting some possible coupling effects between the transition and the hydrofoil's vibrations. Therefore, DNS is coupled with 1 DOF pitching motion that reproduces the hydrofoil's deformation to the torsional mode. Hydroelastic simulations are performed at different degrees of flexibility and frequency ratio. The results are analyzed in the light of previous rigid hydrofoil results (experimental and numerical), in terms of wall pressure, boundary layer characteristics and hydrofoil's vibrations. Hence, the current work can be considered as a continuation of the numerical study of Ducoin and Astolfi, 2019.

The present thesis work can be summarized as the following 5 Chapters:

- **Chapter 1** : In order to begin this study, a state of the art is carried out, presenting numerical and experimental researches that investigated the fluid structure interaction phenomena over different bodies such as cylinders, flat plates, airfoils and hydrofoils over the past twenty years. Additionally, a summary of the boundary layer events at different Reynolds numbers over airfoils is also presented. Some of the research material in the Chapter 1 is also used for the validation of developed numerical fluid-structure coupling models in the following thesis work. Finally, the experimental study of a flexible hydrofoil by Ducoin et al., 2012 is introduced, which used as a basis of reference even though numerical results and measurements are not directly compared.

- **Chapter 2** : This chapter is dedicated to the mathematical models of fluid and structural parts. Navier-Stokes equations are solved for the resolution of the fluid part. A spectral element method (SEM) based fluid solver called Nek5000 is chosen for the resolution of the Navier-Stokes equations. Scalability test on this fluid solver is also presented in this chapter. Towards the end of this chapter, a set of general equations of motion are derived for the resolution of structural part.

- **Chapter 3** : This chapter provides an overall classification of the different fluid-structure interaction problems and associated non-dimensional numbers to characterise our current FSI simulations. We briefly introduce the details of different coupling methods between the fluid and structural parts along with its advantages and disadvantages. The equation of motion of the structural part is modified in this chapter with a correction factor to avoid added mass instability. A partitioned approach is selected to couple Nek5000 with the equation of motion. Within the partitioned approach, two different ways are chosen for the coupling. The first one is explicit coupling in which the temporal accuracy is of O(1) to have stability and the latter is a predictor-corrector method. It is an implicit scheme of higher temporal accuracy (O(3)). The time resolution of equation of motion of the structural part is discretized by using the same temporal scheme as in Nek5000. Finally, this chapter concludes with a study on mesh deformation schemes and demonstrates the validity of the existing methods using an example.

- **Chapter 4** : This chapter is dedicated to the validation of developments that are carried out in this thesis work. The developments mainly consist of implementation of an efficient mesh deformation method and a robust coupling scheme. A comparison study is also made between the implemented explicit and implicit coupling methods with a classical example of VIV of cylinder. The same case is also used for the validation of mesh deformation schemes. Lastly, a self sustained oscillation of NACA0012 at Re =64,000 is taken for the validation of our coupling method to test at higher Reynolds number.

- **Chapter 5** : In the final chapter, the numerical setup is first introduced including a near wall DNS domain which is taken from the previous work of Ducoin and Astolfi, 2019 to reduce the computational expense. Therefore, few validation studies in static and flexible cases are also carried out by comparing the results of near wall DNS with a full size DNS domain. The static validation includes the comparison of boundary layer velocity profiles, transition point and wall pressure signals. In the flexible case, the amplitude and frequency of hydrofoil's pitch velocity from near wall DNS case is compared against to the full DNS domain. Then, simulations obtained with the near wall domain are presented. The results are characterised and organised as follows : Boundary layer flow analysis, Wall pressure analysis and FSI analysis.

The author conclude the manuscript with a synthesis of the work that was executed, a discussion of the results obtained, and a presentation of the perspectives opened up by the thesis work.

Chapter 1

Bibliography

Summary

In this chapter, the effect of Reynolds number over different rigid and flexible bluff bodies such as cylinder and airfoil is presented. Then, the focus is on foils, which undergoes forced and free motions. Both numerical and experimental investigations are considered. The aim is is to get some insight into the understanding of the transition.

1.1 Introduction to flow induced vibrations

Flow over bluff bodies has always been the topic of many researches in fluid dynamics. The estimation of lift and drag forces, and its relationship with the wake flows is on primary importance in most of the cases. For instance, the flow over a cylinder at various Reynolds numbers often shows vortex shedding in the wake and induces periodic lift fluctuations over the body. In the case of flexible cylinder, these vortices induce vibration (VIV), which has been widely studied in Koopmann, 1967, Placzek et al., 2009, PRASANTH and MITTAL, 2007, Fischer et al., 2017, Tumkur et al., 2013. The Fig. 1.1 shows the VIV response of the cylinder at varying Reynolds number along with the wake structures. The upper and lower branches of amplitude responses are obtained due to the different modes of vortex shedding. 2S mode of vortex shedding is observed in lower amplitude of oscillation at Re $<$ 86. At 86$\leqslant$ Re $\geqslant$ 137, the vortex shedding frequency merges with the natural frequency of the cylinder and a lock-in phenomena is observed. As a result, the amplitude of oscillation is increased and C(2S) mode of vortex shedding is observed. Again, at Re $>$ 137 the amplitude oscillation is lower and flow structures are similar to the flow over stationary cylinder and 2S mode of vortex shedding is observed.

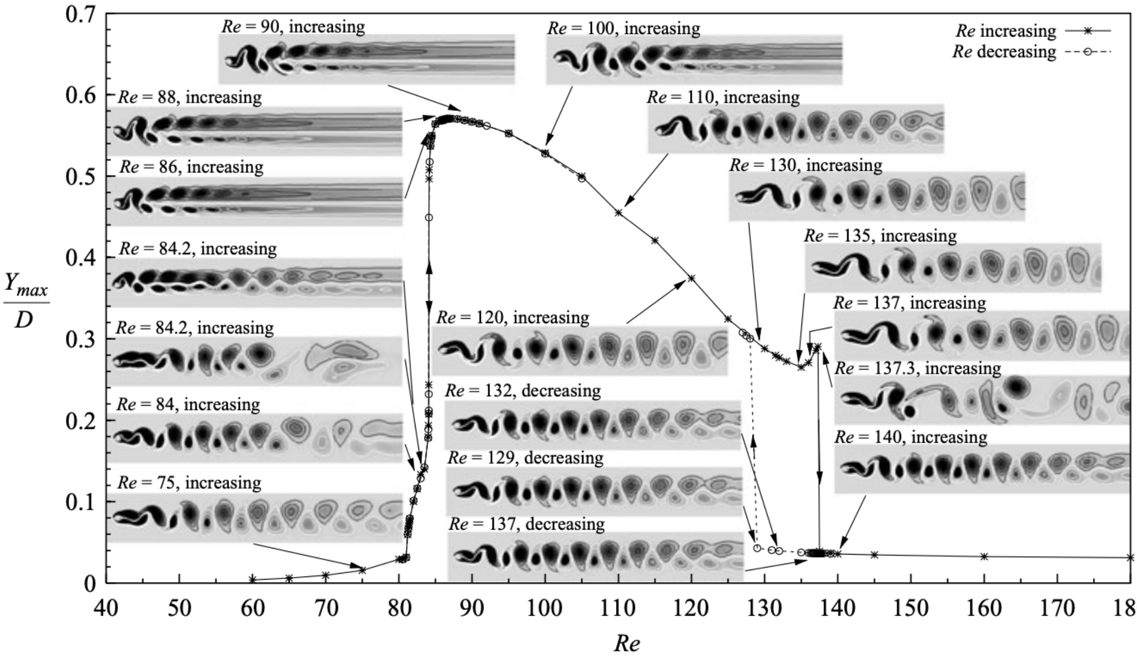

FIGURE 1.1: Amplitude response of the vibration of cylinder at different Reynolds numbers and the corresponding instantaneous vorticity field, PRASANTH and MITTAL, 2007

Similarly, flow induced vibrations can also occurs on airfoils due to wake vortices, laminar separation bubbles, turbulence depending up on the Reynolds number. The unsteadiness in the flow is directly linked with the operating conditions such as flow speed, angle of attack, curvature of the foil etc. Thus, before investigating the effect of FSI on airfoil, the physics behind laminar separation is briefly explained with respect to variation of Reynolds numbers and angle of attack (AoA) from the literature of Galbraith and Visbal, 2009 who investigated the flow dynamics over SD7003 airfoil at different configurations using ILES. The Fig .1.2(a) shows that at constant Re=60,000, as the angle of attack increases, the transition moves toward the leading edge due to the increase of the adverse pressure gradient, whereas the turbulent structures are at about the same scale. At 11°, the transition is right at leading edge, and stall occurs at 14°, characterized by large scale turbulent structures. When the angle of attack is fixed and the Reynolds number is increased (Fig .1.2(b)), the adverse pressure gradient is about the same. As a consequence, at 8°, the laminar separation always occurs near the leading edge. For the lower Reynolds number (Re=10,000), the flow does not reattach and a laminar stall is observed, and start to transition near the leading edge (see the 3D structures). As the Reynolds number increases, turbulent reattachment occurs and a turbulent regime is obtained over the airfoil. The increase of the Reynolds number then have two effects: it leads to smaller turbulent structures within the boundary layer, and advances the turbulent reattachment point i.e. reduces the laminar separation bubble length.

1.2 Unsteady flow over stationary foils

The author would like to mention that this review on stationary foils is not exhaustive, as many researches have been performed experimental and numerical investigation on LSB behaviour and transition mechanism which is now well known. Hence, it is focused on studies that are related to this thesis.

The physic of laminar to turbulent transition was investigated firstly in/for aerodynamic problems (airfoils), then applied to hydrodynamic studies. Over the past few decades, many experimental(Tani, 1964; Genç et al., 2012) and numerical (Rhie and Chow, 1983; Kenneth and Jansen, 1995; Shan et al., 2005; Delafin et al., 2014) investigations were carried out in order to characterise the behaviour of laminar to turbulent transition over foils at different operating conditions. It was shown that the location and type of transition mechanism is dependent on Reynolds number and angle of attack. It seems LES or DNS is necessary to capture the physics related to the dynamics of LSB, transition, vortex shedding and turbulence. Thus, some of the DNS based studies over a static foil are briefly reviewed here.

Ducoin et al., 2016 performed a study at Re = 20 000 over a SD7003 airfoil. The Fig. 1.3 shows an instantaneous vorticity field to detail the transition mechanism and wake interaction. They observed the transition point close to the trailing edge. The transition is induced by the Kelvin-Helmholtz instability that cause LSB shedding. C shape structures are formed, which then interact with trailing edge vortex to generate von Kármán wake vortices. At higher Reynolds number (Re = 66 000), the transition becomes sharper, however the Kelvin-Helmholtz instability is still observed.

Hosseini et al., 2016 investigated the flow around NACA4412 airfoil at a Reynolds number of 400,000 with more than 3.2 billions grid points. It shows the capability of

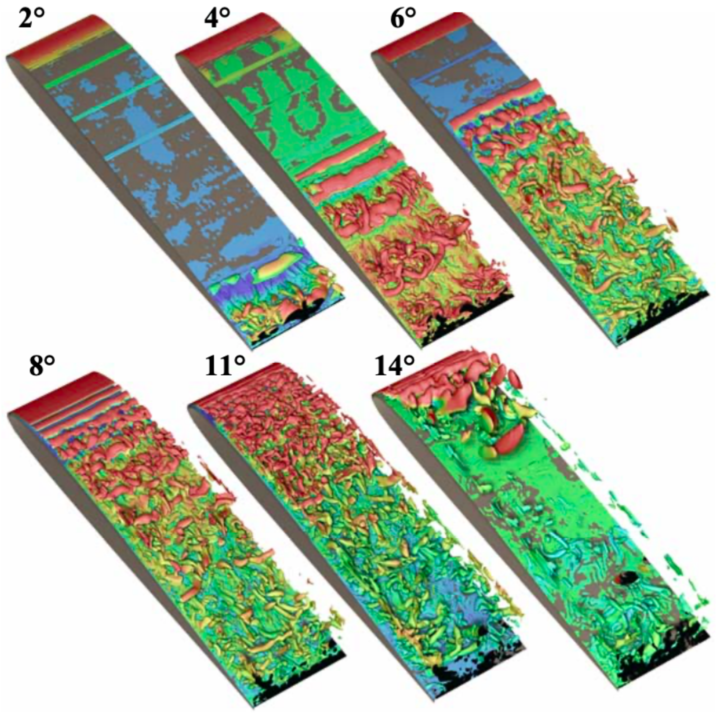

(A) Instantaneous three-dimensional vortical structures are visualized with an iso-surface of the Q-criterion at Re = 60000

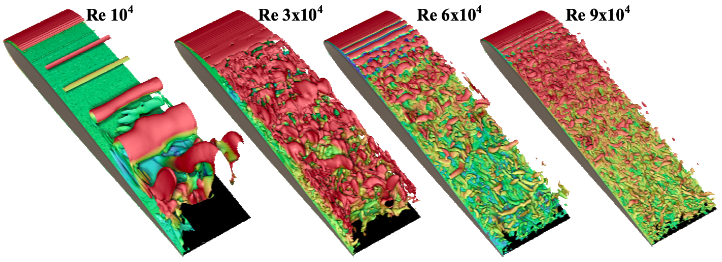

(B) Instantaneous three-dimensional vortical structures are visualized with an iso-surface of the Q-criterion at $8°$ and different Reynolds numbers

FIGURE 1.2: Effect of different Reynolds number regimes on laminar separation process below 10^6 over an airfoil, Galbraith and Visbal, 2009

the DNS code Nek5000 to reproduce the laminar to turbulent transition and turbulence particularly at relatively high Reynolds number. It also shows a strong relation between adverse pressure gradient and turbulent kinetic energy along with the boundary layer regime.

Later, Ducoin and Astolfi, 2019 studied flow around NACA66 hydrofoil at Reynolds number of 450,000 and $\alpha = 4°$. The simulation is performed using spectral element

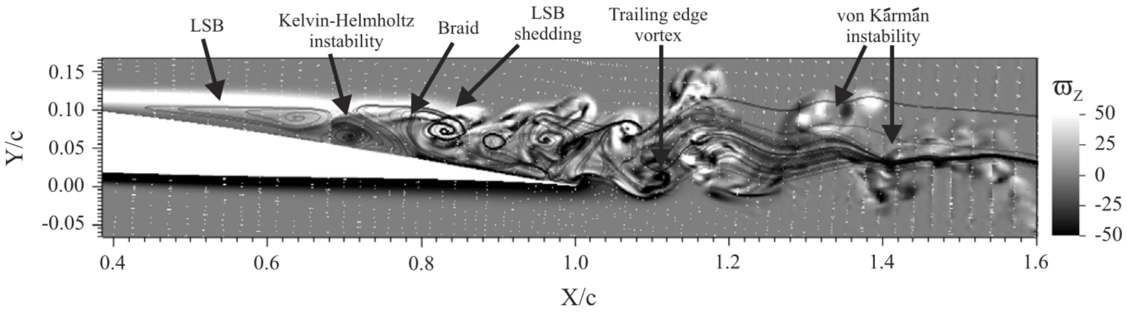

FIGURE 1.3: Instantaneous vorticity field and velocity streamlines along the laminar to turbulent transition region, Ducoin et al., 2016

method to capture the laminar to turbulent transition. The Fig.1.4 depicts the transition along with velocity and pressure contours. The wall pressure signals are compared with the experiments. The laminar to turbulent transition is induced by the LSB and strong periodic pressure fluctuations are noticed in the transition region due to the LSB shedding. A classical H type or K type transition is observed, highlighted by the lambda structures. Finally, random fluctuations of lower amplitude are present in the fully developed turbulent region. The required span length of the foil to capture the transition is highlighted. Periodic boundary conditions are set in span-wise direction and the span width is reduced to save computational time. However, it was suggested that it could slightly force the coherent structures in the transition region at a certain wave length.

Zhang and Samtaney, 2016 investigated a flow past NACA0012 airfoil at Re = 50 000 to understand the influence of aspect ratio on the flow separation and laminar to turbulent transition in DNS. It is observed that the turbulent kinetic energy is affected by the reduced span length particularly close to the region of reattachment.

1.3 Unsteady flow over oscillating foils

Investigation of unsteady flows under dynamic structural conditions are challenging. Theodorsen assumptions (Theodorsen, 1934) are no longer held in these cases. It usually requires time-resolved experimental techniques for both the fluid and the structure, or high-fidelity numerical techniques such as Large Eddy Simulations or Direct Numerical Simulations, which demand large computational resources. In the literature, studies of fluid-structure problems can be divided into two distinct problems, wherein unsteady flow is combined with either forced structural motion or free motion.

(a) *Transition mechanism*

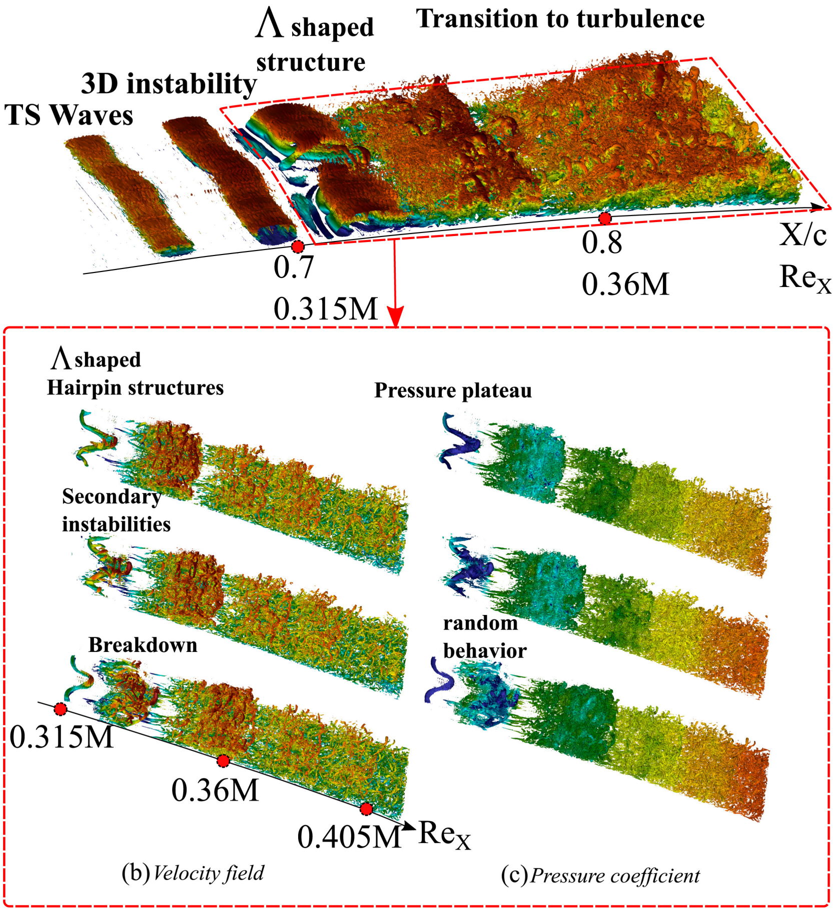

(b) *Velocity field* (c) *Pressure coefficient*

FIGURE 1.4: Iso-surfaces of λ_2 coloured with velocity contours (top and bottom left) and pressure coefficients contours (bottom right), Ducoin and Astolfi, 2019

1.3.1 Forced oscillations

In the forced oscillation cases, a given foil motion is set to reproduce a structural behavior. Of the numerous experimental studies that have addressed this topic (McCROSKEY and PHILIPPE, 1975; Jumper et al., 1987; Pascazio et al., 1996; LEE and GERONTAKOS, 2004.Nati et al., 2015), the majority of the works are related to large pitch oscillations and dynamic stall effects which appear from the leading edge. It comprises of unsteady pressure fluctuations over the airfoil which leads to non linear aerodynamic loads acting over the airfoil. The point of laminar separation is often characterised along with re-attachment and the main focus is on the importance of the pitching frequency on the boundary-layer regime.

Ducoin et al., 2009 investigated the wall pressure analysis of a transient pitching NACA66 hydrofoil at Re = 750, 000 through a combination of experimental and numerical techniques. It involved studying the effect of pitching velocities on the boundary layer regime and hydrodynamic loadings. The computations were performed over RANS based code. The $k-\omega\ SST$ turbulence model is used for turbulence part and γ - Re_θ is used for transition modelling. Experimentally, wall pressure signals showed strong periodic pressure fluctuations downstream of the LSB due to the vortex shedding. The Fig. 1.5 depicts the location of laminar separation, re-attachment and transition points during the rotation of hydrofoil before stall obtained numerically. It was observed that the length of LSB decreases with increasing angle of attack; however, the Reynolds-Averaged Navier-Stokes (RANS) simulations were unable to capture the core LSB dynamics and hence the wall pressure fluctuations upstream.

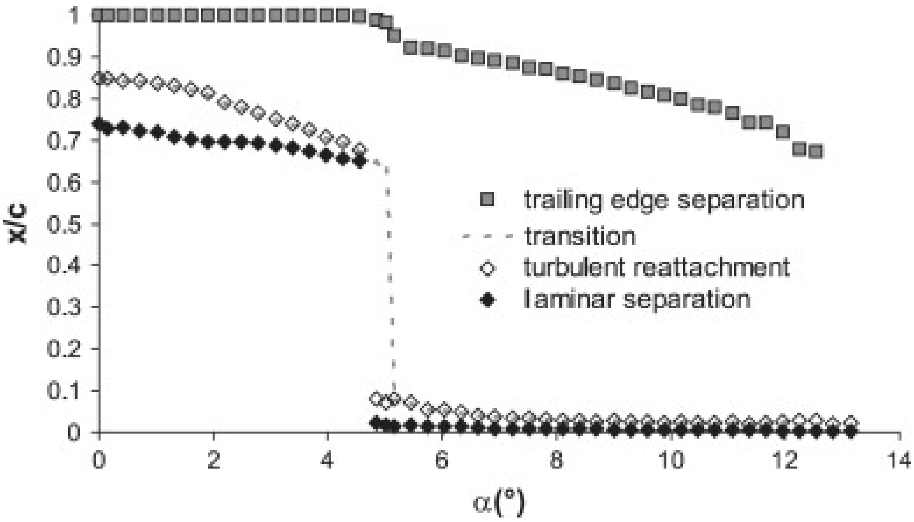

FIGURE 1.5: Location of separations, reattachment and transition points on the suction side as functions of the angle of incidence during the hydrofoil rotation at Re = 750 000 (CFD RANS simulation of Ducoin et al., 2009)

Visbal, 2014 studied the flow around SD7003 airfoil at Reynolds number, $Re = 500,000$ using ILES. They showed that the upward pitch of the foil forces the flow separation to advance towards the leading edge. The LSB contracts, as the angle of attack increases. This contraction reaches a critical point at which the LSB bursts. A similar study was also carried out by the same authors on a NACA0012, which showed a smoother transition compared to the SD7003 due to lower curvature of the leading edge.

Rahromostaqim et al., 2016 investigated the flow over Eppler 387 airfoil at Reynolds number of 30,000 using well resolved LES. This work differs from the previously mentioned studies, as the frequency and amplitude of oscillation are significantly higher. They observed that the high frequency of oscillation induces strong hysteresis effects on the aerodynamics load in comparison to the low frequency oscillations.

Recently, Negi et al., 2018 used a well-resolved Large-Eddy Simulations (LES) in Nek5000 to study the flow physics of relatively small amplitude pitch oscillations of an airfoil at Re = 100, 000. They analyzed the effect of small amplitude pitching airfoil on LSB and transition locations. The Fig. 1.6 displays the effect of pitching on wall shear stress. A sinusoidal change in the transition point is observed. The red region in Fig. 1.6(a) shows strong wall shear stress which causes transition to turbulence. The black spots in Fig.1.6 (b) depicts the separated flow region. The transition is induced by the LSB and two positions of LSB's are observed during the pitching. One is near to the trailing edge which persist only for short period of time and the latter is at leading edge which is sustained for a longer period. An hysteresis effect is observed between the movement of transition point from downstream to upstream.

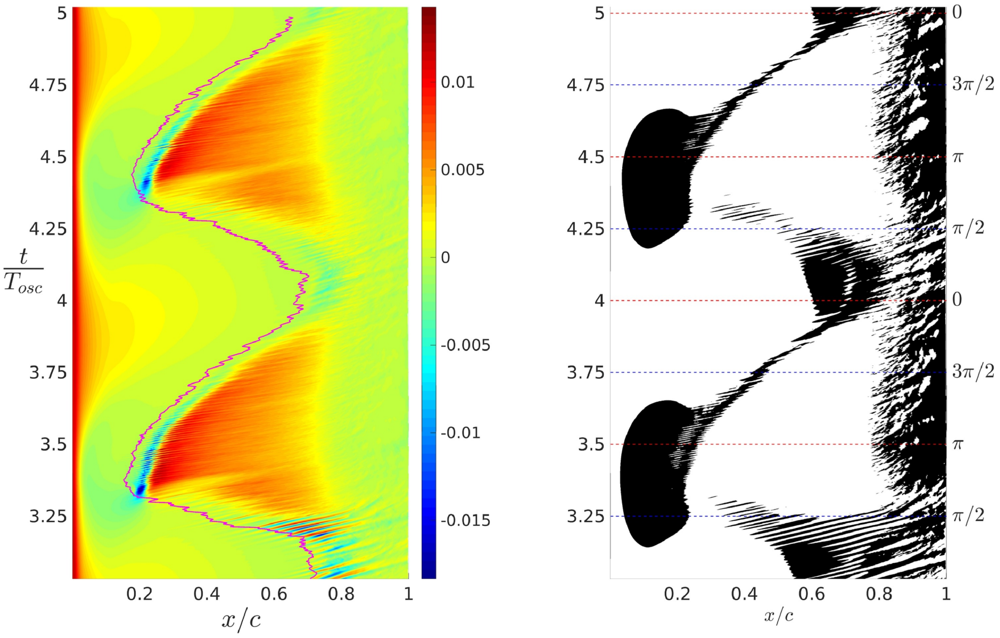

(a) Wall-shear stress (τ_w). (b) Separated regions (black).

FIGURE 1.6: Space-time plot for the skin friction (a) and separation of the flow (b). The plots are captured from the instantaneous flow field which is averaged over the span-wise direction, Negi et al., 2018

1.3.2 Free oscillations

The behaviour of the fluid flow under dynamic conditions are explored in the above cases (one way interaction). In the case of free oscillations, a two way coupling takes place between the structure and the fluid, which induces fluid structure interaction (FSI).

Aeroelastic studies

Lian and Shyy, 2007, performed a numerical simulation at Re = 60 000 using RANS with e^N transition model over a SD7003 airfoil in which a portion of the upper surface of airfoil is covered with a latex membrane. It is observed that the LSB is generated over the flexible membrane, forces the foil to vibrate and an energy transfer occurred in between the flexible foil and fluid flow. Thus, the flow is affected by the vibration and the separation point is advanced when compared to the rigid case. The fluctuating frequency of the membrane (primary) and vortex shedding frequency (secondary) can be observed in the lift coefficient. However, the averaged quantities of lift coefficient from flexible foil is close to that of rigid case. Gordnier, 2009 studied the coupling effects of flexible membrane wing under unsteady flow conditions using a higher order 2D Navier Stokes equations at a Reynolds number ranging from 2500 to 10, 000. At lower Reynolds numbers, strong coupling is observed between the airfoil vibration frequency and vortex shedding frequency. As the Reynolds number further increased, the wing structure starts to show some dynamic vibrations. On the other hand, the unsteady vortex flow became more turbulent. Thus, a 2D Navier Stokes equation may no longer be justifiable to study the coupling effects.

Poirel et al., 2008 performed a wind tunnel experiment to study self-sustained oscillation of a NACA0012 section in transitional flows. The foil was supported by a flexible one degree-of-freedom (1-DOF) pitching system (torsional spring and damper). At a Reynolds number ranging from $Re = 4.5\times10^4$ to 1.3×10^5, self-sustained limit cycle oscillations (LCO) were observed, dictated by laminar flow separation near the trailing edge at $0°$. Once established, the LCO governed by the transition behaviour. The experimental observations were supported by a CFD RANS simulation (Poirel et al., 2011). The Fig. 1.7 shows the pitch angle response and moment coefficient acting over the foil for one cycle of LCO. The high frequency components in the moment coefficient is due to the shear instabilities present in the flow which lead to von Kármán vortex shedding at the wake and low frequency component is due to the laminar flow separation. They confirmed that the laminar flow separation is the key physic behind the onset of self sustained LCO of airfoil. Moreover, the vortex shedding in the wake has no impact on the structural behaviour. They also confirmed that the presence of intense free stream turbulence can adversely affect the amplitude response of LCO.

Later, Poirel and Mendes, 2014b did another experimental study at the same range of Reynolds numbers and the same airfoil but with 2 DOFs, i.e plunge and

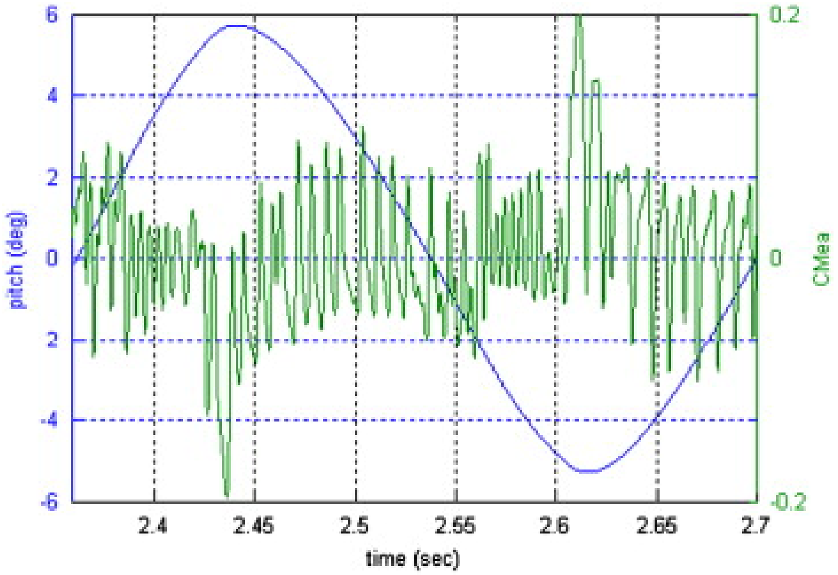

FIGURE 1.7: Pitch angle response and aerodynamic moment coefficient about the EA for one cycle of LCO; Re = 8.54×10^4; CFD RANS simulation, Poirel et al., 2011

pitch motions. Two types of oscillations are observed, i.e, small amplitude oscillations (SAO) and large amplitude of oscillations (LAO). The SAO type oscillations are the result of separated laminar shear layer, which has been detailed in the previous studies whereas LAO type oscillations are due to an external perturbation applied on the foil. In the latter type oscillation, both plunging and pitching frequencies merge into a single frequency. Moreover, a phase difference is also observed between plunging and pitching motions. In SAO type oscillations the plunge motion did not make any significant effect on the laminar separation flutter. However, the energy transfer between the flow and the structure is seen to increase when there is a plunging motion. In addition to that, no self sustained oscillation is observed in pure plunging case.

Yuan et al., 2013 studied the interaction between the flow and 2 DOF (pitching and plunging), 1 DOF (pitching) motions using LES at Reynolds number of 77 000 on the NACA0012. It confirms the presence of laminar flow separation induces oscillation in 1-DOF pitching case and highlights the primary importance of the pitch modal response in 2-DOF system i.e plunging motion does have any impact on the LCO. Besides, the pitch angle and moment coefficient shows a 180° phase difference. However, lift coefficient and pitch motion shows only a small phase difference.

Recently, Barnes and Visbal, 2018 and Barnes and Visbal, 2019 studied the impact of transition on Laminar Separation Flutter (LSF) over a NACA0012 airfoil at different Reynolds numbers in between 7.7×10^4 and 2.0×10^5. They used an implicit large eddy simulation (ILES) for the calculations. In the previous studies, the LCO response was observed only at the following range of Reynolds numbers, 4.5×10^4 and 1.3×10^5. In this study, they observed LCO at Re = 1.5 × 10^5 by initially providing an external perturbation in the moment coefficient. Following the external perturbation, the dynamic response of the foil is similar to that of Re = 1.1 × 10^5. The LCO behaviour can be observed upto Re = 2 × 10^5 by increasing the intensity of external disturbances. Moreover, they also investigated the effect of Reynolds number on the amplitude of oscillations. As the Reynolds number increases, the transition happens earlier and a linear relation of moment coefficient is observed with respect to the pitch angle. The Fig. 1.8 shows the transition, separation, reattachment, and momentum coefficient over time associated to the pitching down of foil. The blue and red line of Cf represents the separation and reattachments position over upper and lower surfaces. The colored region in the vorticity plot (Fig. 1.8(a)(b)) shows the transition to turbulence. They observed a dominant peak in the vorticity (first stage transition to turbulence) that occurs just before the maximum and minimum angle of attack on the both upper and lower surfaces. This dominant region coincides with the reattachment and a peak in the moment coefficient is observed. Then, the LSB moves upstream and again comes back to the trailing edge where the transitional flow begins to reemerge and a second stage transition occurs. Again, another small peak in the moment coefficient is observed corresponding to the second stage transition. Finally, when the LSB of both upper and lower surfaces appears near the trailing edge, the reversal of moment coefficient, upstream of the elastic axis is also observed from the pressure coefficients.

Açıkel and Genç, 2018 investigated studied experimentally the control of laminar separation over wind turbine NACA4412 airfoil at Reynolds number of 2.5×10^4, 5×10^4 and 7.5×10^4. A partially flexible membrane is installed on a small portion of the wing's upper surface (between $x/c = 0.2$ and $x/c = 0.7$) where the LSB appears and affects the performance of the airfoil. The flexible membrane and the LSB interacted with each other and formed short vortices which forces the membrane to vibrate simultaneously. The scale of the vortices affects the number of modes of vibration i.e, as the size of the vortices increases, the number of vibration modes decreases. Moreover, a good agreement is observed between the frequency of oscillation and frequency of velocity from the fluid flow near to the membrane wall, which confirms the interaction between boundary layer flow and the flexible membrane. The vibration triggers the laminar to turbulent transition earlier in comparison to the rigid case and the size of the LSB is reduced.

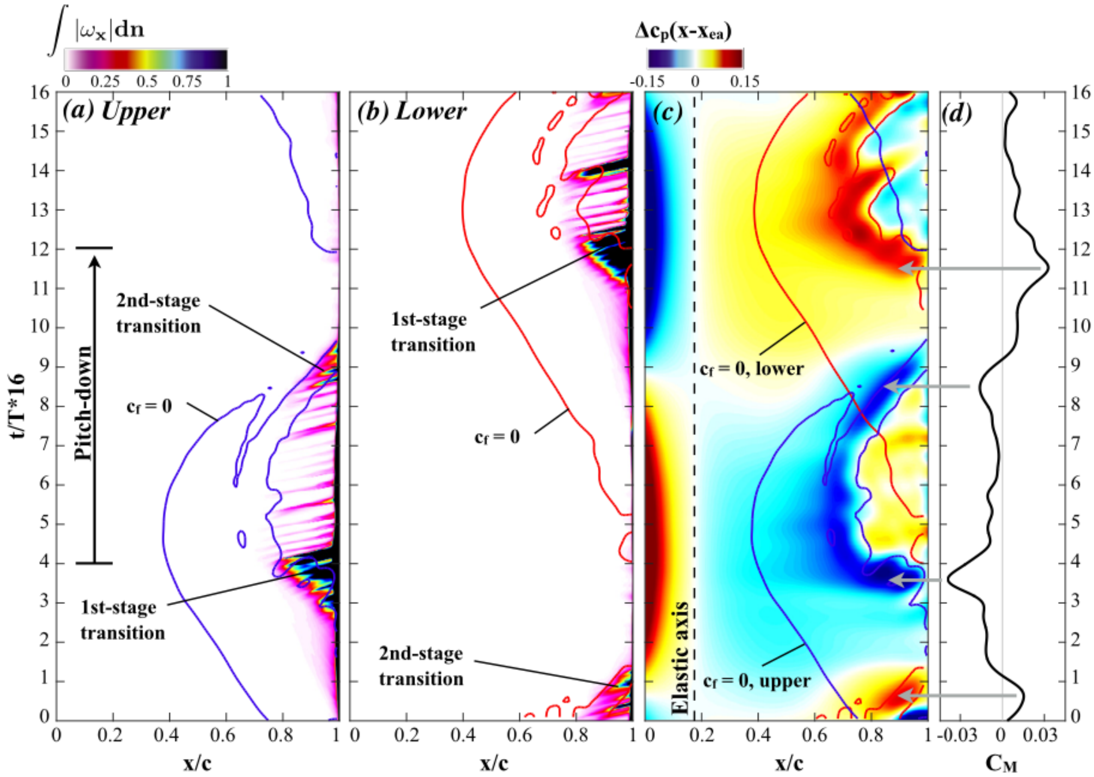

FIGURE 1.8: Filtered Cp fluctuations overlaid with friction coefficient line at $C_f = 0$ and Re = 7.7×10^4, Barnes and Visbal, 2019

Hydroelastic studies

Many researches were conducted FSI studies of composite hydrofoils as base studies to develop composite propellers. Zarruk et al., 2014 presented experimental measurements for NACA009 trapezoidal hydrofoils made up of metals and composites in a steady flow conditions up to Reynolds number of 1 $\times 10^6$. They showed that the hydrodynamic behaviour of flexible composite hydrofoils is significantly different from the stainless steel and aluminium made hydrofoils. The composite hydrofoils shows of course larger deflection and twist deformations under steady hydrodynamic loading. There is no significant vibration observed for pre-stall incidences whereas a totally different response was observed in post-stall configurations for metal and composite hydrofoils. Later, Young et al., 2018 investigated a 2-DOF FSI experimentally and numerically on the same hydrofoil at Reynolds number ranging from 0.25 $\times 10^6$ to 1.2 $\times 10^6$ under steady state flow conditions as well. They suggested that the hydrodynamic efficiency of hydrofoils can be increased by taking advantage of the intrinsic material bend-twist coupling. Pernod et al., 2019 did an experimental and numerical work in quasi-steady flow regime at moderate Reynolds number ranges from 90, 000 to 560, 000 on NACA66 trapezoidal hydrofoil. They demonstrate a good agreement on the bending and a reasonable comparison on the twist between experimental and numerical results. Additionally, Lock-in with von Kármán shedding and structural excitation due to leading-edge vortex shedding are also observed experimentally at the lower range of Reynolds numbers. Recently, Arab et al., 2019 performed a study on a composite hydrofoil to examine the influence of imposed internal pressure in the controlling of hydrodynamic performance. Those studies about composite hydrofoils are a crucial step to optimize flexible propellers, as they demonstrated the ability of composite to passively control deformations to enhance performances. They also produces a large amount of experimental data that can be used for the validation of numerical FSI codes. However, very few of them investigated the dynamics of FSI as well as the effect of laminar to turbulent transition on the structural behaviour, although the Reynolds numbers lies in the transitional regimes.

Only few studies have been conducted on the prediction of transitional flows and its impact over flexible hydrofoils at Reynolds number ranging from 300,000 to 1,000,000. Ducoin et al., 2012 carried out an experimental work on vibration of NACA66 hydrofoil submitted to laminar to turbulent transition induced by LSB. Both rigid and flexible hydrofoils are considered. The rigid hydrofoil is made of stainless steel and the flexible one is made of polyacetate (POM) to significantly enhance the fluid structure interaction. The Fig.1.9 shows the first four natural frequencies/ mode shapes of the flexible hydrofoil observed in water as: f1 = 43 Hz (first bending mode), f2=171 Hz (first torsional mode), f3=291 Hz (second bending mode) and f4=560 Hz (both bending and torsional mode).

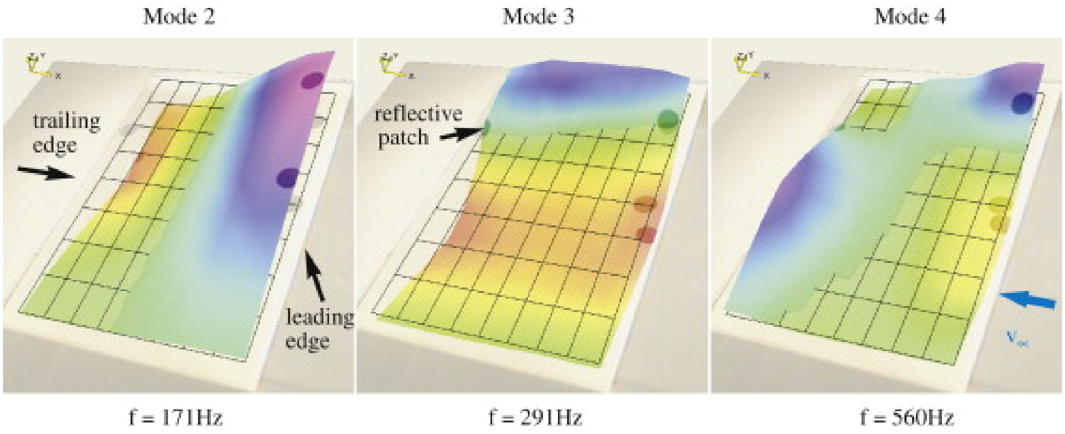

FIGURE 1.9: Experimental mode shapes of the flexible hydrofoil, Ducoin et al., 2012.

It is noticed that the transition process interacts with the vibrations of the hydrofoil when the vortex shedding frequency is getting closer to the natural frequency of the hydrofoil. As a result, the amplitude of vortex shedding and transition frequencies increases when compared to the rigid case (see, Fig.5). A resonance is observed when the mode 4 engages with the vortex shedding frequency which is seen lying close each other. Additional frequency components are also observed in the hydrofoils vibration.

The current thesis is inspired from the above mentioned work. However upto the author′s knowledge, there are no high fidelity numerical studies performed on the transition induced vibration over hydrofoils at these range of Reynolds number. When compared to aeroelasticity, hydroelasticity can be more difficult to solve because of the added mass effect and fluid damping forces. Viscous effects and cavitation also bring further complications on the hydroelastic problems. It should be noted that the above said aeroelastic problems usually consist of larger deformations and low frequency oscillations whereas the current hydroelastic problem shows higher frequency oscillations with lower amplitude deformations (vibratory response). Moreover, the observed natural frequency of hydrofoil is in the range of shedding frequencies associated with the transition, which may lead to different interaction mechanism. Unlike the airfoils in which the transition comprises of a large portion of the chord that dominates the boundary layer flow, a laminar profile of marine propeller is often used where the maximum thickness of the foil is close to the centre of the chord in laminar profiles. This is done so that the adverse pressure gradient reduces and transition is delayed which is used to reduce frictional drag on the body.

1.4 Conclusion

The dynamic of transition induced vibration has been well investigated in aeroelasticity at various range of Reynolds number. With the recent development of flexible lifting profiles in hydrodynamic, there is a need to get a better knowledge in the fluid structure interaction mechanism. In particular, the amplitude and frequency of vibrations are quite different in hydroelasticity as compared to aeroelasticity due to the added mass and fluid damping forces. As the Reynolds number is larger, significant difference in the global response of the system is expected.

In fact, the complex operating conditions, unsteadiness in the flow, and nonlinear coupling between the fluid and structure make the experimental measurements of the flow challenging. On the other hand, DNS simulations shows a promising approach, which can bring detailed understanding of the physic involved. Up to the authors knowledge, there is no numerical simulation which resolves the laminar-turbulent transition induced vibration over flexible hydrofoils. The objective of this work is to investigate in this area.

Chapter 2

Numerical Resolution of Fluid & Structure

Summary

The mathematical and numerical background of equation of motion for the fluid and structural part are detailed in Chapter 2. This chapter starts by presenting a numerical frame work for the resolution of fluid flow. Then, the spectral element code Nek5000 is introduced to solve the fluid part and a modal approach is adopted for the structural part. Lastly, an equation of motion is derived for 1-DOF rigid pitching hydrofoil from a set of generalised equation of motions and it is coupled with Nek5000.

2.1 Mathematical modelling of fluid flow

Mathematically, the fluid flow can be governed by a set of conservation laws:

- Conservation of Mass
  The amount of fluid mass (m) going in and out of a control volume $(\Omega(t))$ is constant in time (t). That is;

  $$\frac{d}{dt}m(t) = 0 \tag{2.1}$$

  By applying the Reynolds transport theorem and assuming that it is an incompressible fluid, we get:

  $$\operatorname{div} u = 0 \tag{2.2}$$

  where $u = (u_x, u_y, u_z)^T$ is the velocity vector.

- Conservation of Momentum
  According to Newtons second law, the rate of change of momentum of a material in domain $\Omega(t)$ with respect to time is equal to the sum of the forces acting on it as shown in Eq. 2.3.

  $$\frac{d}{dt}\int_{\Omega(t)} \rho_l u dV = \int_{\partial\Omega(t)} \sigma dS + \int_{\Omega(t)} \rho_l f_{ext} dV \tag{2.3}$$

  where ρ_l is the density of the fluid, f_{ext} is the external forces such as gravity, $d\Omega(t)$ is the boundary of the control volume $(\Omega(t))$ and σ is the stress tensor from Cauchys principle based on the constitutive relation of newtonian compressible fluid which can be written as:

  $$\sigma = -pI + 2\mu d \tag{2.4}$$

  where μ is the dynamic viscosity of the considered fluid, p is the dynamic pressure and d is strain rate tensor:

  $$d = \frac{1}{2}\left[\nabla u + (\nabla u)^T\right] \tag{2.5}$$

Thus by applying again the Reynolds transport theorem, divergence theorem and mass conservation we can re-write the Eq.2.3 and to obtain the following equation of motion for the fluid part:

$$\rho_l \frac{Du}{Dt} = \operatorname{div}\sigma + \rho_l f_{ext} \tag{2.6}$$

Finally, the Navier Stokes equations for newtonian and incompressible fluid can be arrived as follows:

$$\frac{\partial u}{\partial t} = -\nabla p + \frac{1}{Re}\nabla \cdot (\nabla + \nabla^T)u - u \cdot \nabla u \tag{2.7}$$

$$\nabla \cdot u = 0 \tag{2.8}$$

The Reynolds number is defined as $Re = \rho_l u_\infty c / \mu$, where c is the chord length and u_∞ is the upstream velocity.

2.2 Numerical resolution of fluid flow

The numerical resolution of fluid flow is obtained by solving the Navier Stokes (N-S) equations. To do this, we have selected a spectral element solver called Nek5000 developed at Argonne National Laboratory (USA) by Paul F. Fischer and Kerkemeier, 2008. Before going into detail about the N-S in Nek5000, theory of Spectral Element Method is briefly presented in the following subsection.

2.2.1 Spectral Element Method

SEM is an extension of finite element method (FEM) combined with spectral method (SM). Thus, SEM provides an advantage of dividing the domain into elements as in FEM and obtaining spectral convergence rate in space as in SM. (Patera, 1984,Maday et al., 1990,Orszag, 1980). SEM uses spectral basis function of higher degree within single element as shown in Fig.2.1. Thus, it provides solutions with little numerical dispersion and dissipation error.

To filter the spurious pressure modes from the solution, we used $P_N - P_{N-2}$ pressure formulation in our computation. As a result, we choose Gauss-Lobatto Legendre (GLL) quadrature basis points in the reference domain (bi-unit domain as shown in Fig.2.2) for the velocity (i = 0 to N where i is the number of points).Upon considering the pressure space, the basis is the set on the Gauss Legendre (GL) quadrature points (i =1 to N-1 where i is the number of points). The computation is faster in this formulation as compared to the $P_N - P_N$ pressure formulation. More details about this method can be found in Oliveira and Seriani, 2011,Deville et al., 2002,KREISS and OLIGER, 1972.

To save some computational time, the simulation can be first initialized at low Lagrange polynomial in order to develop the velocity and pressure fields, after which we can progressively increase the element order to obtain full DNS.

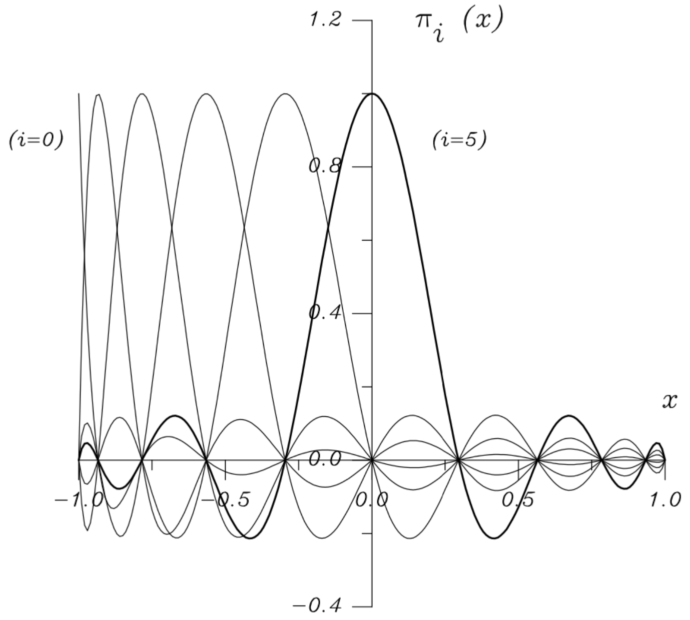

FIGURE 2.1: An example of Legendre spectral-element basis functions corresponding to N = 10 (Only half of the basis in an element is displayed.)

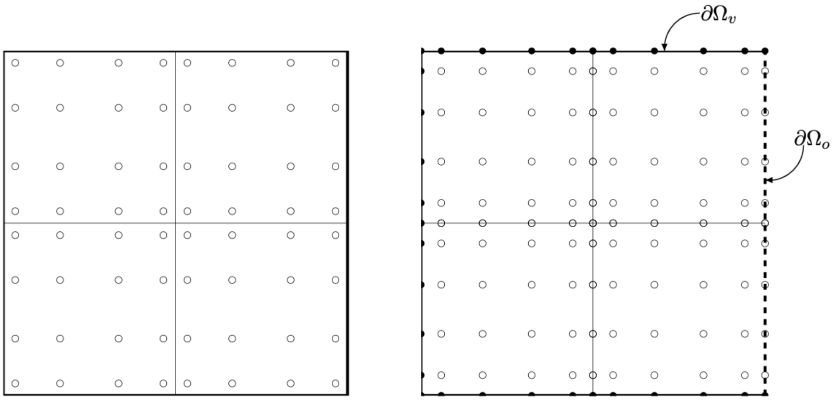

FIGURE 2.2: Lagrange interpolation basis points for the pressure on the left, and for the velocity on the right in a spectral element configuration with, N = 5. Empty dots denote actual degrees of freedom whereas solid dots denote Dirichlet boundary points for the velocity. (Fischer, 1997)

2.2.2 Key features of Nek5000

The main advantages of Nek5000 for the present study are listed below:

- Arbitrary Lagrangian Eulerian formulation is supported. It uses arbitrary coordinate system (between Lagrangian at the moving wall to Eulerian away from it) that allows to solve N-S equations with mesh deformation.

- It is highly scalable in parallel computing.

- It ensures continuity between elements.
- It has semi-implicit 3^{rd} order accuracy in temporal scheme (BDFk/ EXTk).
- The grid points are tightly coupled with in each elements.
- It has efficient pre-conditioners.

2.2.3 Navier Stokes in Nek5000

The Navier Stokes equation under ALE frame work over a domain $\Omega(t)$ in spectral element method can be written as (Fischer et al., 2017):

$$\frac{d}{dt}(v,u) = (\nabla \cdot v, p) - \frac{1}{Re}(\nabla v, \sigma) - (v, u \cdot \nabla u) + c(v,w,u) \tag{2.9}$$

$$(\nabla \cdot u, q) = 0 \tag{2.10}$$

where v and q are test functions. They belong to $X_0^N(\Omega(t)) \times Y^N(\Omega(t))$ which are considered as a function of time as the domain$(\Omega(t))$ moves. σ is the stress tensor $\sigma_{ij} := \left(\frac{\partial u_i}{\partial x_j} + \frac{\partial u_j}{\partial x_i}\right)$. Moreover, an extra term present in the Eq.2.9 represents the trilinear form of mesh velocity.

$$c(v,w,u) := \int_{\Omega(t)} \sum_{i=1}^{3}\sum_{j=1}^{3} v_i \frac{\partial w_j u_i}{\partial x_j} dV \tag{2.11}$$

Spatial discretisation is achieved by decomposing the real/physical domain into N number of spectral elements where the pressure field is created on Gauss-Legendre (GL) nodes and the velocity using Gauss-Lobatto-Legendre (GLL) nodes. The Eq.2.9 is temporally discretised using a semi implicit time matching scheme called k^{th} order Backward Difference Formula (BDFk/ EXTk). Thus the Eq.2.9 can written as :

$$\sum_{j=0}^{k} \frac{\beta_j}{\Delta t}(v^{n-j}, u^{n-j})_{n-j} = (\nabla \cdot v^n, p^n)_n - \frac{1}{Re}(\nabla v^n, \sigma^n)_n + \sum_{j=1}^{3} \gamma_j \tilde{N}^{n-j} + O(\Delta t^k) \tag{2.12}$$

$$(q^n, \nabla \cdot u^n)_n = 0 \tag{2.13}$$

where β_j and γ_j are the coefficients of temporal scheme as shown in Table 2.1. $O(\Delta t^k)$ is the global truncation error of the temporal scheme which refers to the temporal accuracy of the system. $\tilde{N}^{n-j}$ represents mesh motion and the non linear term in the Eq.2.9. Thus, at t^m:

$$\tilde{N}^m := c(v^m, w^m, u^m)_m - (v^m, u^m \cdot \nabla u^m)_m \tag{2.14}$$

$$= \sum_{i=1}^{3}\sum_{j=1}^{3}\int_{\Omega(t)} v_i^m \left[\frac{\partial w_j^m u_i^m}{\partial x_j^m} - u_j^m \frac{\partial u_i^m}{\partial x_j^m}\right] dV \tag{2.15}$$

By omitting the truncation error and re-arranging the Eq.2.12 by putting all the unknowns at t^n on the left hand side :

$$\frac{\beta_0}{\Delta t}(v^n, u^n)_n + \frac{1}{Re}(\nabla v^n, \sigma^n)_n - (\nabla \cdot v^n, p^n)_n = r^n \tag{2.16}$$

$$(q^n, \nabla \cdot u^n)_n = 0 \tag{2.17}$$

$$r^n = \sum_{j=1}^{k}\left[\gamma_j \tilde{N}^{n-j} - \frac{\beta_j}{\Delta t}(v^{n-j}, u^{n-j})_{n-j}\right] \tag{2.18}$$

The nonlinear terms in the above equations (right hand side) are treated explicitly and the linear part (left hand side) is treated implicitly.

TABLE 2.1: The coefficient of BDFk/ EXTk temporal scheme

k	β_0	β_1	β_2	β_3	γ_1	γ_2	γ_3
1	1	-1	0	0	1	0	0
2	$\frac{3}{2}$	$-\frac{4}{2}$	$\frac{1}{2}$	0	2	-1	0
3	$\frac{11}{6}$	$-\frac{18}{6}$	$\frac{9}{6}$	$-\frac{2}{6}$	3	-3	1

2.2.4 Scalability test in Nek5000

The scalability of Nek5000 has been already tested in many cases and reasonable efficiency is proven for more than 35,000 processors (Offermans et al., 2016; Tufo and Fischer, 2001). The computational efficiency mainly depends upon the number of elements per CPU and type of machine. Therefore, it is important to perform a scalability test to find the optimum number of processors to carry out further studies. A scalability test of Nek5000 is performed on Jean-Zay HPE SGI 8600 machine at Re = 450, 000 upto 16284 processors provided by GENCI-IDRIS under the grant of 2019-(100631). The total number of degree of freedom is 326 million grid points. The results are shown in Fig. 2.3. It demonstrates a good scalability with small decrease of efficiency when the number of processors are more than 8192. Also, Nek5000 shows the best performance when the number of cores are powers of 2. Hence, 4192 cores seems to be optimal for our studies.

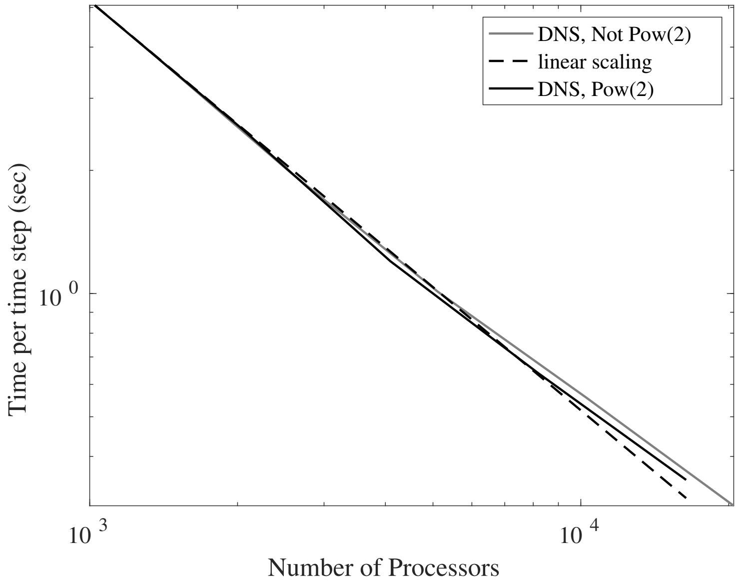

FIGURE 2.3: Scalability test for problem size of 326 million grid points v/s the number of cores on a HPE SGI 8600 machine. $Pow(2)$ and Not $Pow(2)$ represents the number of processors that are power of 2 or not.

2.3 Mathematical modelling of Structural Part

In this work, the structure is assumed to be rigidly moving under the fluid load instead of having any linear or non linear material deformations. A modal approach is sufficient to model this type of fluid structure interaction and a structural finite element solver is not required to solve the dynamics of the structure. In order to solve the structural dynamics, an equation of motion for 1 degree of freedom is derived for a desired type of motion (either translational or rotational motions) in the Cartesian frame as described in Leroyer and Visonneau, 2005 and De Nayer et al., 2020. This equation can be implemented in the fluid solver to carry out the coupling at each time step.

The Fig. 2.4 (a) shows schematic diagram of a general cantilevered 3D blade. Unfortunately, DNS over full span length of a hydrofoil is computationally not feasible. It forced to investigate the FSI using DNS at selected portion of the hydrofoil span where the flexibility is higher. Typically, the flexibility is higher towards the free end of the hydrofoil but due to the difficulty of carrying experimental measurements at that location, we selected a section at $0.75z$ from the clamped end where z is the

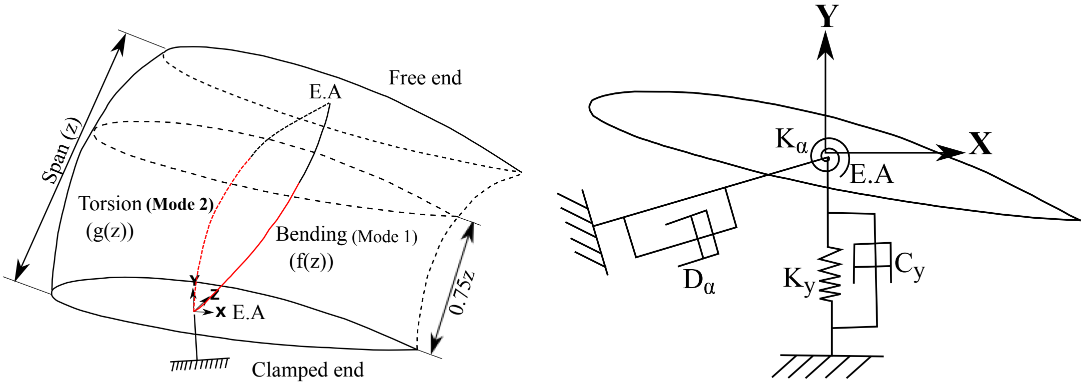

(A) Schematic diagram of a 3D cantilevered hydrofoil.

(B) 2DOF system with spring and damper.

FIGURE 2.4: Transformation of a flexible section of 3D hydrofoil to 2DOF system

span of the hydrofoil. Then, the structural parameters of this section is computed by a set of generalized shape functions and 2D structural quantities. The generalized shape functions can be derived from the Eq. 2.19 and the corresponding values are plotted in Fig. 2.5 with respect to the span of the hydrofoil. It describes the vertical $f(z)$ and twist $g(z)$ displacements of the full blade into bending and torsion, respectively. The shape functions are derived from a combination of experimental and finite element analysis, which were originally described in Ducoin and Young, 2013 and used in Chae et al., 2017.

$$\begin{aligned} f(z) &= \frac{\cosh(1.875z) - \cos(1.875z) - 0.734[\sinh(1.875z) - \sin(1.875z)]}{2} \\ g(z) &= \sin\left(\frac{\pi}{2}z\right) \end{aligned} \tag{2.19}$$

The red colored portion is considered to compute the material properties of flexible hydrofoil at the location of $0.75z$ from the clamped end. Thus, for each section we can deduce the 3D structure problem into an equivalent 2D problem as shown in Fig. 2.4 (b). The 3-D material behaviour of the hydrofoil can be obtained by integrating the 2-D sectional terms along the span-wise direction using the shape functions. The 2D structural parameters and equation for the computation of 3D structural parameters are shown in Appendix B.

In this thesis the system is simplified to single mode approximation (1 DOF system) particularly in pitching degree of freedom. The equation of pitching motion with respect to Z-axis is shown in Eq.2.20 where I_α is the moment of inertia of the hydrofoil, D_α is the damping coefficient of pitching hydrofoil, K_α is torsional stiffness of the hydrofoil and T_{EA} is the torque obtained about the elastic axis.

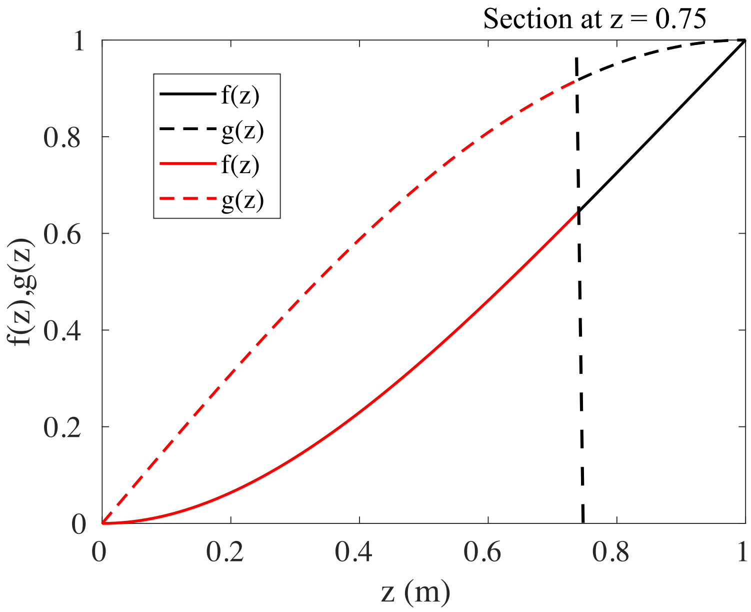

FIGURE 2.5: Shape functions for the approximation of 3D structural quantities.

$$I_\alpha \ddot{\alpha} + D_\alpha \dot{\alpha} + K_\alpha \alpha = T_{EA} \tag{2.20}$$

Here $\ddot{\alpha}$ is the angular acceleration, $\dot{\alpha}$ angular velocity and α is the angle of twist of the hydrofoil during pitching.

2.4 Conclusion

This chapter is dedicated to the presentation of the mathematical modelling of fluid and structural equation of motions. The spectral element solver Nek5000 is selected to perform the DNS at Re = 450,000. It is a high order spectral method derived from finite element method which consists of least numerical dissipative and dispersion error to solve turbulence more accurately. The solver also supports mesh deformation/ motion to perform moving body cases with high scalability. With regards to the structural part, a modal approach is chosen to perform our FSI problem. A given section of flexible cantilevered hydrofoil is transformed into an equivalent 1 DOF system.

Chapter 3

Resolution of Fluid-Structure Interaction & Mesh Deformation

Summary

This chapter lies in the heart of this thesis and is devoted to the detailed study of fluid-structure interactions and their coupling methods. We will first detail the classifications in fluid-structure interaction problems and the non-dimensional quantities associated to it. Secondly, we will look into the mathematical modelling of fluid structure interaction with different coupling techniques followed by the methods developed for the current work. The computation of added mass is also described. This chapter is concluded with a comparison study on mesh deformation schemes.

3.1 Introduction and classification of fluid-structure interaction problems

Fluid-structure interaction (FSI) is an area of study where the fluid and solid interact each with other. It is a multi-physics problem and a quite challenging scientific topic to both researchers and engineers. It plays a vital role in the design of many engineering applications. The numerical methods such as CFD/ FEA and their couplings have became a widely accepted as a tool for research in this interdisciplinary domain. In most of the applications, the fluid force causes change in the dynamic state of the structure and as a result, the flow field will be modified by the motion of the structure. Depending upon the flexibility of the structure and flow configuration, a two way interaction can be engaged in this scenario. Fluid-structure interaction can be observed in natural systems. A leaf curling up in the wind is a typical example of a natural fluid interaction phenomena. The nature and configuration of interaction is different in each cases even-though they are submitted to fluid structure interaction.

To cover some of the aspects in this interdisciplinary field of research, the fluid structure interaction systems can be differentiated into two main cases : rigid body vibration and flexible body oscillation. The Fig.3.1 represents an example of rigid body interaction and it is often called vortex induced vibration (VIV) of a rigid cylinder. Vortex-induced vibrations can be critical for large structures. In this example, the vortex sheddings are not able to alter the shape of the structure due to the high rigidity of the structure. However, a vibration can occur as a result of the interaction depending up on the mechanical properties of the structure. If the natural frequency of the vortex shedding becomes close to the natural frequency of the structure, it may lead to strong coupling and resonance which causes catastrophic failure of the system. Whereas, in flexible body oscillation seen in FSI problems, the structures are deformed/ distorted under the action of the fluid force. The Fig. 3.2 depicts an example of flexible structure deformation due to the fluid force. The banner undergoes flapping and introduces additional drag due to the the flutter. Virot et al., 2016 performed a research in relation to the intrinsic flutter instability of flags. Harvesting of energy is possible from flapping flags by covering the flag surface with piezoelectric patches which is essentially taking advantage of fluid structure interaction.

Numerically, the rigid body-fluid interaction problem is simpler when compared to the deforming case because the rigid body motion can be captured by solving an equation of motion. This is usually implemented within the fluid solver whereas flexible structures consist of linear and/or non-linear deformations and it has to be solved using numerical methods such as finite element method.

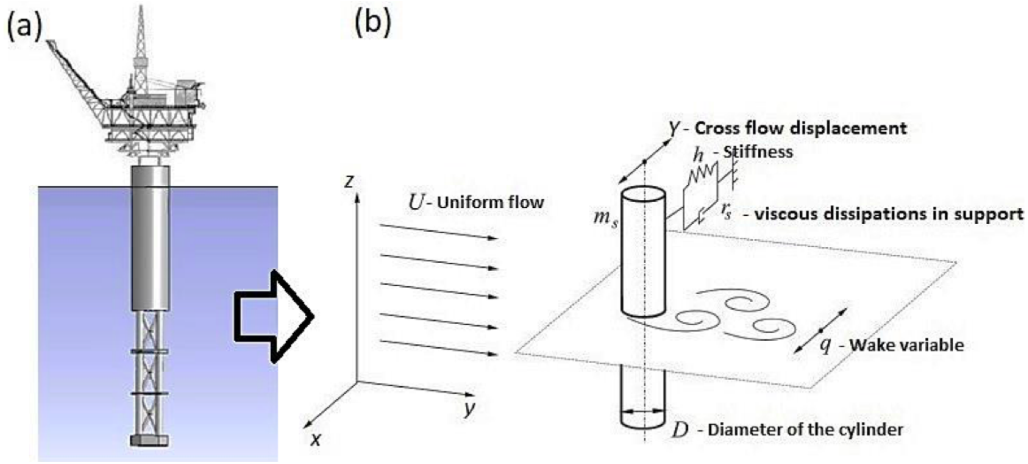

FIGURE 3.1: (a) A schematic representation of Spar Platform submerged in sea (b) A schematic model of coupled structure and wake oscillator for 2D vortex-induced vibration (W.N.W. Hussin and Rahman, 2017)

FIGURE 3.2: A banner towed to a helicopter. The picture is taken from wikipedia

In this thesis, we are interested in a hydroelastic problem which undergoes a rigid body vibration.

3.2 Non-Dimensional numbers related to FSI

Dimensionless numbers are widely used in fluid mechanics when compared to solid mechanics in order to study and characterise the flow behaviour. To characterise the FSI response, the following set of non-dimensional parameters are mostly used (de Langre, 2001).

- Mass number (M)
  It is the ratio of density of the fluid (ρ_f) to that of the structure (ρ_s). For instance, when the mass number is close to 1 or above. It refers to a dense fluid and light structure. As a result, the fluid exerts additional mass over the body as soon as the body accelerates. It causes numerical instabilities in weak and/or explicitly coupled problems. Implicit coupling is required to maintain the stability of the coupling. Conversely, when the mass number is less than 1 ($M << 1$), then the fluid is light compared to the structure and explicit/ weak coupling is able to maintain the stability of numerical computations.

$$\mathrm{M} = \frac{\rho_f}{\rho_s} \tag{3.1}$$

- Frequency ratio
  It is the ratio of the natural frequency of the structure (f_N) to the characteristic frequency of the fluid flow (f_s) (vortex shedding frequency in the case of VIV of cylinder at low Reynolds number).

$$F = \frac{f_N}{f_s} \tag{3.2}$$

- Amplitude ratio (A)
  It is the ratio of displacement of the structure y to a given characteristic length D. The latter can be linked to the structure geometry or a spatial quantity from the flow.

$$A = y/D \tag{3.3}$$

- Time bar
  It is the ratio of physical time (t) evolution of the coupled system to the characteristic time period ($T_{fluid/solid}$) from the fluid or solid.

$$T = \frac{t}{T_{fluid/solid}} \tag{3.4}$$

- Reynolds number
  It is the ratio of inertial forces to viscous forces in a fluid. It is an important quantity to evaluate the boundary layer regime (laminar, turbulent) of the flow.

$$Re = \frac{\rho_f U_\infty D}{\mu} \tag{3.5}$$

3.3 Mathematical modelling of fluid structure interaction

The resolution of the fluid structure interaction problem requires mathematical models for both fluid and structural domains as shown in Fig. 3.3. Special attention has to be given to the interface between the two domains. Additional conditions are imposed on the coupling interface to capture the interaction process.

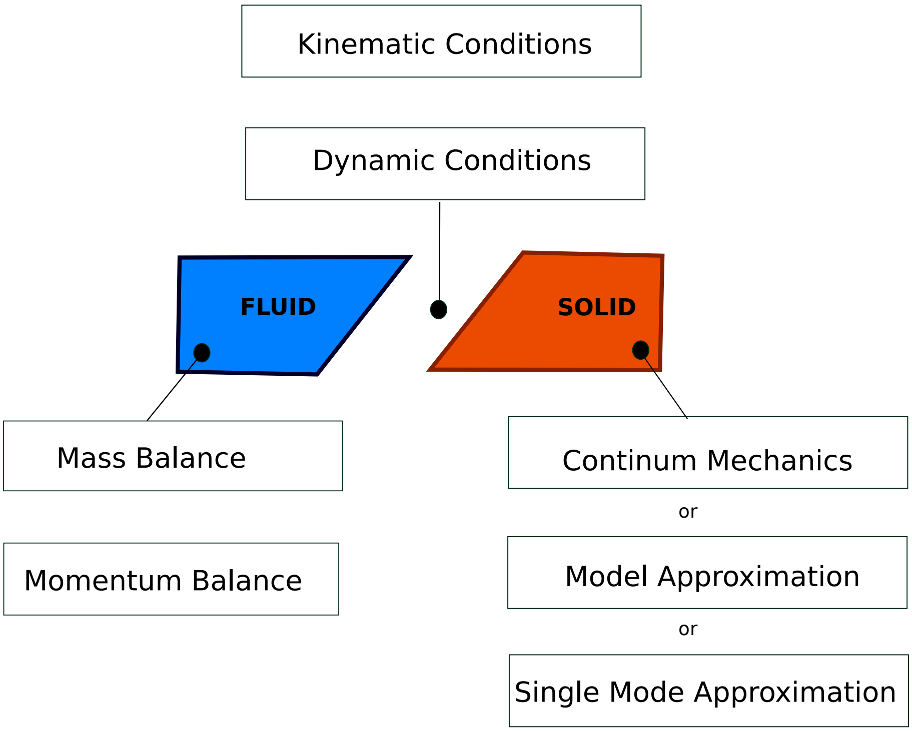

FIGURE 3.3: Schematic diagram representing the fluid-structure interaction problem

Our interest is to investigate a fluid-structure coupled problem of a hydrofoil. The hydrofoil is fully submerged in the fluid domain i.e, there is no influence of the free surface. The system therefore responds to the equations of fluid established in Chapter 2 which is recalled below (see Eq. 3.6 - 3.7):

$$\frac{\partial u}{\partial t} = -\nabla p + \frac{1}{Re}\nabla \cdot (\nabla + \nabla^T)u - u \cdot \nabla u + c(w,u) \tag{3.6}$$

$$\nabla \cdot u = 0 \tag{3.7}$$

For the sake of clarity and simplicity, the structural equation is simplified using a single mode approximation (1 DOF system), which is defined by displacement in Y -direction. The simplified equation of motion is referred from Chapter 2 (see Eq. 3.8).

$$m_s\ddot{y} + c_y\dot{y} + k_y y = f_y \tag{3.8}$$

In addition to the fluid and structural equations, more constraints are required particularly at the coupling interface. The coupling interface is the common surface zone between the fluid and structure. It is also called a wet surface. That is, the interface is theoretically unique where the stress in the fluid medium and the structure medium are equalized. There are mainly two conditions that need to be satisfied for a stable, accurate fluid-structure interactions computations. They are written respectively in the form of Eq. 3.9 and Eq. 3.10.

- the continuity of the velocity fields at the interface.

$$u(y,t) = \frac{dy}{dt}(t)\varphi(y) \tag{3.9}$$

where $\varphi(y)$ is model shape of the motion and is a known quantity.

- the continuity of the forces (f) at the interface.

$$\int_{interface} \{[-pI + \mu(\nabla u + \nabla' u)] \cdot n\}\varphi dS = f_y \tag{3.10}$$

where dS is the surface area of an element at the interface.

Eq. 3.9 implies the continuity of the velocity fields according to the motion of the body and Eq. 3.10 ensures the continuity of the stress through the interface. The first term in Eq. 3.10 refers to the dynamic pressure and the latter term refers to the viscous pressure. The fluid stress which is transmited from the fluid to interface should be the same as those transmitted from the interface to structure. In most of the cases, the perfect equality of Eq. 3.9-3.10 cannot be guaranteed because (Durand, 2012):

- the discrete interface may not be unique

- the stress fields are not necessarily continuous between the media

These differences, even if minor, can create problems such as interface power generation (Lombardi et al., 2013). However in our study, the solid-fluid interface is unique by applying a **moving wall** boundary condition on the fluid mesh where the structure is located. Then the moment exerted by the fluid is calculated about the neutral axis of the structure.

3.4 Numerical resolution of the fluid-structure interaction

To summarise, a fluid-structure interaction problem consists of:

- a fluid domain and system of fluid equations (Eq. 3.6) - (Eq. 3.7).
- a rigid or elastic structure and an equation of motion for the body (Eq. 3.3).
- a fluid-structure interface and coupling constraints (Eq. 3.9 - 3.10).

In order to perform the fluid structure interaction problems, it is necessary to convert all the above mathematical formulations into partial or ordinary differential equations to discretise them in space (using FDM, FVM, FEM) and in time (using Adams-Bashforth, Range Kutta, BDFk/ EXTk). We have already seen in Chapter 2 how the (Eq. 3.6) - (Eq. 3.7) are discretised in space and time. The equation of motion (Eq. 3.3) is a simple second order ordinary differential equation which can be disctretized in time using any implicit/ explicit temporal schemes as mentioned. The most important part is considered to be the coupling method which ensures with the transfer of energy in between the fluid and structure.

3.4.1 Coupling Methods

Coupling between fluid and structural solvers are cannot be considered as straight forward. Each of the coupling method has its own advantages and disadvantages. Therefore, understanding of its application and its requirements are very important in the selection process. Coupling of fluid and structural solvers can be mainly made by monolithic, partitioned and decoupled approaches.

Decoupled approach

It is rather a simplified approach for FSI computation. Both computations are not coupled together at each time instants. It is a step by step procedure. The fluid and structural computations are calculated separately. However the input (the pressure load) to the structural solver comes from the fluid solver which assumes that the structure is rigid. Then the structural part is solved without interacting with the fluid. This coupling method can be taken into consideration when the effect of deformation of structure is significantly low to make any impact on the fluid flow. For instance, the deformations of a rigid structure can be ignored under hydrostatic loading conditions. In this case, the pressure field around the body is calculated from the fluid solver, where it is considered as an input to the structural solver in order to solve the equation of motion of the structural part. Since there is no interaction, the interface constraints (Eq. 3.9 - 3.10) are no longer validated and the system is not conserved in terms of energy. Ezkurra et al., 2018 have done a comparative study between decoupled and coupled approach in a Butterfly valve problem.

Partitioned Approach

It is the most widely used coupling method in the FSI applications for moving flow. Piperno et al., 1995 and Farhat and Lesoinne, 2000 developed several partitioned FSI couplings. In this approach, dedicated fluid and structural solvers are used for the solutions, similar to the decoupled approach. However, they exchange informations at each time step. They are coupled each other during the whole simulation. The transfer between the two codes can be done by using an external software/ sockets. High modularity of softwares is one of the main advantages of this method. Similarly, each solver can have its own time schemes and time steps (Idelsohn and Oñate, 2006). Moreover different space discretization techniques can be used for each of the fields. However, a special attention has to be given for the difference in temporal schemes and space discretisation. For instance, the fluid part can be solved by finite volume method and structural part can be solved by finite element method but the transfer of informations and deformation/ re-meshing of the mesh can be challenging (Durand, 2012). The energy conservation at the coupling interface is difficult to handle and it can be a potential source of error in this kind of scenario (Lombardi et al., 2013). On the other hand, partitioned method has several limitations. Partitioned approach needs careful implementation and formulation to avoid instability and accuracy issues especially when there is added mass effect which will be discussed later in this Chapter. Some of the different types of algorithms present in partitioned approach to couple fluid and structural codes developed by Farhat and Lesoinne, 2000 is shown below. In the schematic figures, U denotes the structural velocity vector, V denotes the fluid velocity, P represents the pressure and n represents the time instant.

- Conventional Serial Staggered (CSS)
  This algorithm is a weak/ explicit coupling algorithm and widely used in aeroelasticity problems (low mass number problems). In such cases these algorithms are simple, stable, accurate and fast. The algorithm needs only informations from the previous time step and calculate parameters for the next time step. However, this method can be improved by doing sub iterations until a better convergence is obtained. Presence of added mass is the primary source of instability in this method. The schematic diagram of algorithm is shown in Fig.3.4 and more details about this approach can also be found in Piperno and Farhat, 2001.

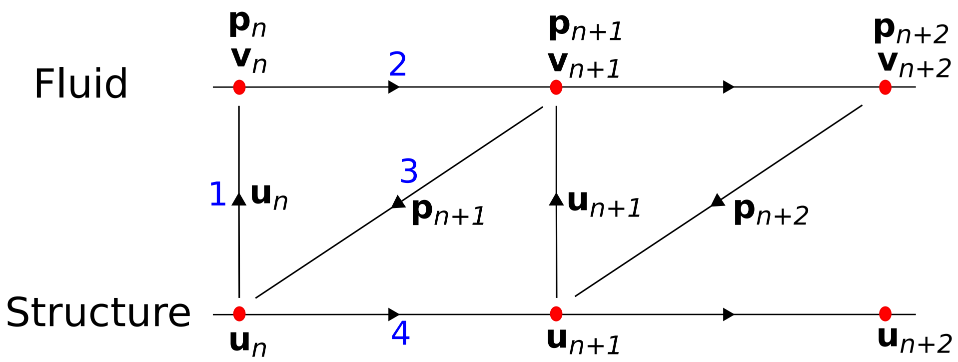

FIGURE 3.4: Conventional Serial Staggered (CSS) algorithm.

- Conventional Parallel Staggered (CPS)
  This synchronous algorithm aims to reduce the overall computation time by allowing a parallelization of the fluid and structure problems. Thus, the transfer of information is carried out simultaneously at the beginning of the time step between the fluid and structural solvers. However this method is still an explicit scheme. The schematic diagram of algorithm is shown in Fig.3.5.

- Improved Serial Staggered (ISS)
  This algorithm is also called ”lagged algorithm with prediction”. It is an asynchronous coupling algorithm which introduces a time difference between the fluid and structure resolutions because the synchronous algorithm does not respect the interface coupling constraints (kinematic condition (Eq. 3.9) and dynamic continuity (Eq. 3.10)). The CSS algorithm is thus modified and it is presented in the semi-implicit form. The schematic diagram of algorithm is shown in Fig.3.6.

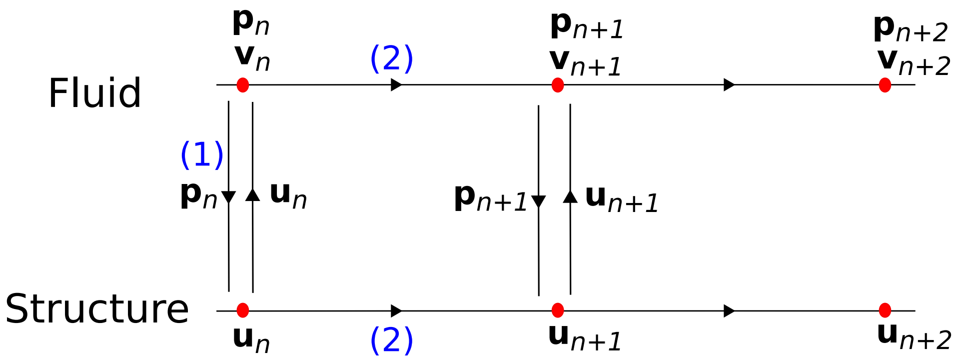

FIGURE 3.5: Conventional Parallel Staggered (CPS) algorithm

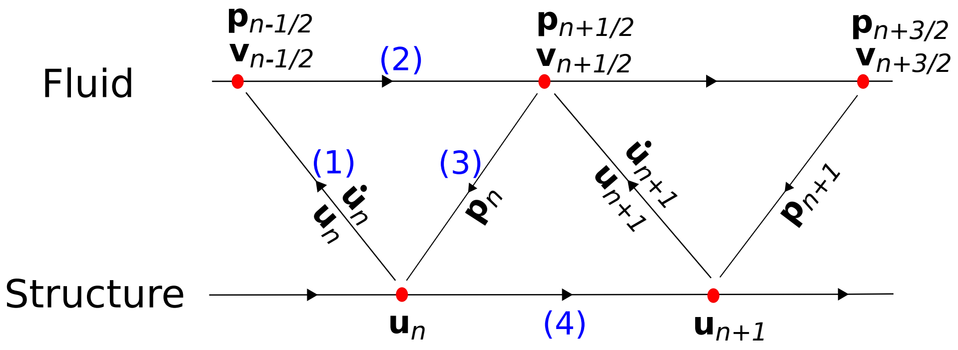

FIGURE 3.6: Improved Serial Staggered (ISS) algorithm

- Improved Parallel Staggered (IPS)

  This method proposes an improvement of the ISS scheme, which does not have any feedback term from the fluid solver within a single time step. An improvement in terms of exchange of information between the fluid and structure parts is done at the half-step in this algorithm. IPS should produce better results compared to CPS at the expense of an additional half-step in between the time step. The schematic diagram of algorithm is shown in Fig.3.7.

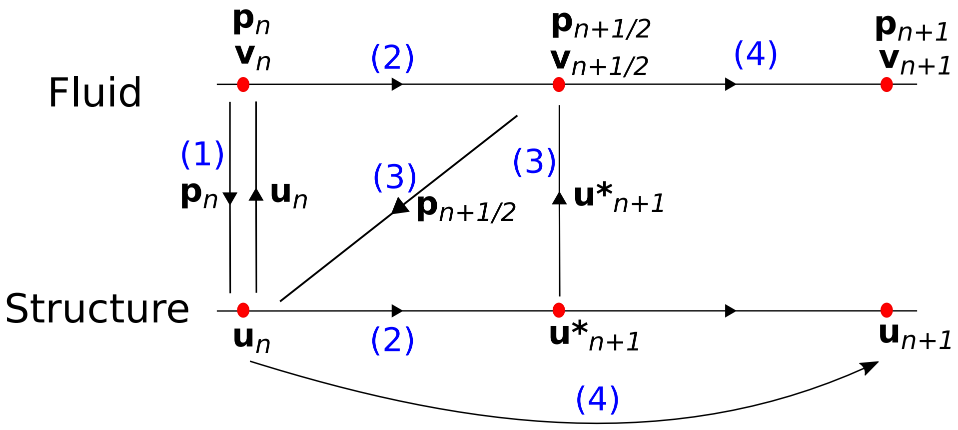

FIGURE 3.7: Improved Parallel Staggered (IPS) algorithm

To summarize, the partitioned coupling method can be generally divided into two types, weak and strong coupling. The difference between these coupling methods is shown in Table 3.1:

TABLE 3.1: Comparison of weak and strong coupling

Weak Coupling (Explicit)	Strong Coupling (Implicit)
No sub iterations in a time step	Sub iterations are needed in a time step
Stability issues	Highly stable
Non conservation of energy at interface	Conservation of energy
Smaller time step	Larger time step
Can be improved by predictor	Algorithmic improvement is possible
Simple algorithm	Complex algorithm

Monolithic Approach

In this methodology, the fluid and structure equations are solved together in the same system of matrix equations with interface constraints. As a result, a single solver is enough for solving FSI problems. The method is conservative intrinsically and the coupling constraints at the interface are verified as well. The main advantage of monolithic approach is that larger time steps can be adopted as compared to other FSI coupling methods. They are also highly suitable for strongly coupled problems. However when the coupled problems consists of significant difference in scaling of variables in the multi-field problem, the matrix which solves coupled problem will be ill conditioned (Farhat and Lesoinne, 2000). Therefore, it would be needed to find a good pre-conditioner to make the solver to gain higher efficiency in terms of computation time and the whole solver has to be validated again (Hübner et al., 2004). So, the monolithic coupling method is limited to small systems. Above all, monolithic approaches are expensive and difficult to implement.

Finally, the summary of the coupling methods is shown in Fig.3.8. Further, the classification based on numerical method is more challenging because the adaptation of numerical technique depends on the physical phenomena that we want to investigate. For instance, immersed boundary element methods in fluid-structure interaction are getting attention of many researchers (Sotiropoulos and Yang, 2014, Kim and Choi, 2019).

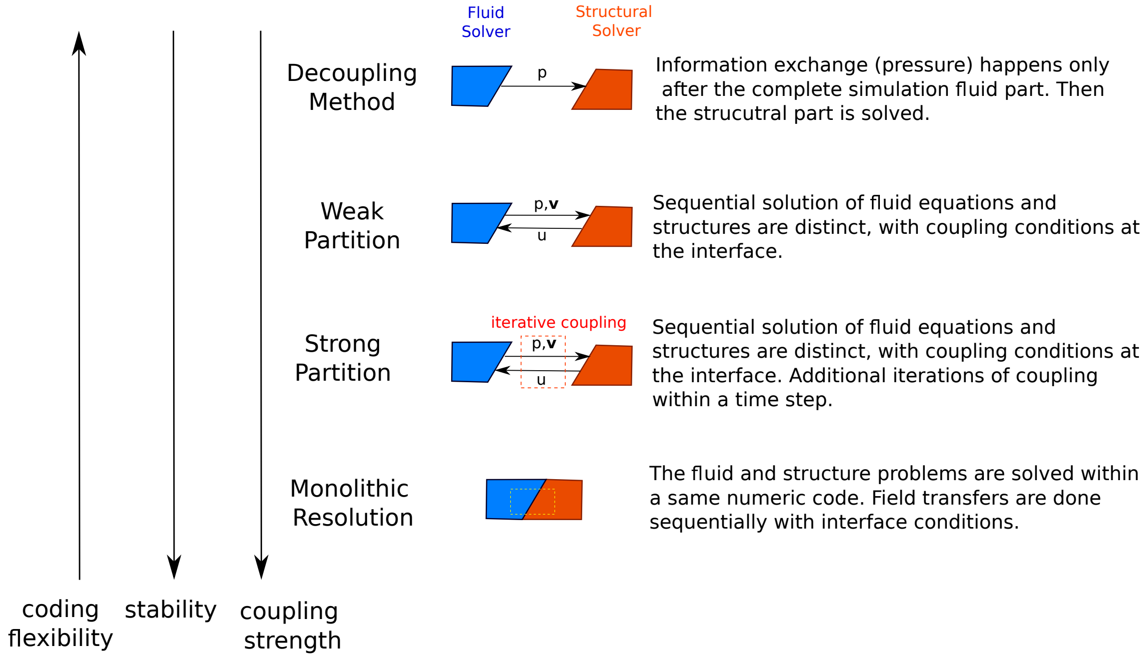

FIGURE 3.8: Summary of the coupling methods

3.4.2 Modified Equation of motion due to Added Mass effect

Added mass is a virtual mass added to the system when the body accelerates in a fluid. The effect of added mass is not negligible when the mass ratio of fluid to structure (mass number) is close to 1 or above. The added mass is a very well-known phenomenon and widely investigated by Green and Stokes who calculated the term added mass accurately for simple geometries. The added-mass effect is very common in the study of flexible marine structures because the density of the water is not negligible compared to the density of the flexible marine structures and it is strongly linked to the convergence of problems during FSI simulations. To avoid this added-mass effect from the numerical simulations an artificial added mass method is introduced (Yvin et al., 2018a; Young et al., 2012a). This method is illustrated by considering a rigid body which has only one degree of freedom in Y-direction (vibrates upward and downward). So the Eq. 3.8 is retained here.

$$m_s\ddot{y} + c_y\dot{y} + k_y y = f_y \tag{3.11}$$

where f_y is the total fluid force including the added mass effect in Y-direction because the added mass effect is intrinsically included in the classical CFD solvers. The added mass effect is due to the dynamic fluid pressure and it is an opposite force to the direction of acceleration of the body. It causes instability issues due to the imbalance of forces on right and left hand side. So we re-write the right hand side of the above equation in terms of the standard fluid force and added mass force.

$$m_s\ddot{y} + c_y\dot{y} + k_y y = f_{st} - m_a\ddot{y} \tag{3.12}$$

Theoretically the total fluid force (f_y) can be separated into two parts: One part is added mass force ($m_a\ddot{y}$) which is negative due to the opposite action of motion and the remaining part is called standard force (f_{st}). Since, the f_y cannot be separated in reality, an artificial added mass is added on the both sides of Eq. (3.12) in order to obtain the force balance.

$$(m_s + \overline{m}_a)\ddot{y} + c_y\dot{y} + k_y y = f_{st} - m_a\ddot{y} + \overline{m}_a\ddot{y} \tag{3.13}$$

where $\overline{m}_a$ is the artificial added mass. The added mass effect can be avoided, when the artificial added mass becomes equal to the physical added mass which will be discussed later in Section 3.4.4. Finally the EOM can be written as :

$$(m_s + m_a)\ddot{y} + c_y\dot{y} + k_y y = f_{st} \tag{3.14}$$

3.4.3 Computation of Added Mass

It is necessary to obtain a correct value of the added mass in order to achieve a stable and accurate FSI simulation. The numerical test shows stable and accurate solutions when the artificial added mass is close enough to the real added mass (Young et al., 2012a). Prediction of added mass effect becomes difficult if the shape of the object is complex or if it changes its position during the computation. Presence of confinement, free surface or other bodies can also affect its value. Thus, it is important to implement a pressure equation to calculate the added mass matrix dynamically. Its calculation is a time consuming operation, thus it can be made once at the beginning of the computation or at different instants if the shape/ position of the object changes significantly. An important remark is that, the body is accelerated with unit acceleration to compute the added mass in all the calculation methods as shown below:

- Using Laplace equation (de Langre, 2001)
  Laplace equation of pressure can be used to calculate the added mass effectively. In order to do that, a linearized Navier-Stokes equation is considered under the assumptions of very small amplitude of deformation and a negligible flow velocity. Thus, the linearized Navier-Stokes equation can be written as:

$$\mathrm{div}\, u = 0 \tag{3.15}$$

$$\frac{\partial u}{\partial t} = -\nabla p + \frac{1}{S_T}\Delta u \tag{3.16}$$

where S_T is the stokes number. Due to the negligible range of viscous effects the terms with Stokes number is disappeared and Eq. 3.16 is simplified as follows:

$$\frac{\partial u}{\partial t} = -\nabla p \tag{3.17}$$

Similarly we can re-write the interface constraints (Eq. 3.9-3.10) with the same assumptions:

$$u(y,t)\cdot n = \dot{y}(t)\varphi(y)\cdot n \tag{3.18}$$

$$M\int(-pn)\cdot\varphi dS = f_y \tag{3.19}$$

where M is the mass number. The tangential components of the fluid force disappears in Eq. 3.19 since the viscous effects are neglected. So only normal component of the fluid force is considered at the interface and the energy is conserved. Now, we consider not only on the interface but everywhere in the fluid, so the velocity field and pressure field becomes:

$$u(y,t) = \dot{y}(t)\varphi_u(y) \tag{3.20}$$

$$p(y,t) = \ddot{y}(t)\varphi_p(y) \tag{3.21}$$

where $\dot{y}(t)$ is the time dependence and is a known quantity. $\varphi_u(y)$ and $\varphi_p(y)$ are space dependences which are unknown. Now, let us re-write the simplified Navier-Stokes equation (Eq. 3.15 and Eq. 3.17) using Eq. 3.20-3.21

$$\text{div}\,\varphi_u = 0 \tag{3.22}$$

$$\varphi_u = -\nabla\varphi_p \tag{3.23}$$

Similarly, the interface constraints are reshaped into:

$$\varphi_u\cdot n = \varphi\cdot n \tag{3.24}$$

$$f_y = -\ddot{y}\big[M \textstyle\int \varphi_p n \cdot \varphi dS\big] \tag{3.25}$$

where the term inside the bracket is added mass and it is a constant, which only depends up on the shape of the moving body.

$$m_a = M \int \varphi_p n \cdot \varphi dS \tag{3.26}$$

The objective is to find φ_p which can be obtained by taking divergence of the momentum equation(Eq. 3.23) results in a Laplace equation of pressure.

$$\Delta \varphi_p = 0 \tag{3.27}$$

and the interface is :

$$-\nabla \varphi_p \cdot n = \varphi \cdot n \tag{3.28}$$

Laplace equation can be solved by any numerical methods such as FDM, FVM and FEM etc. Moreover, many exact solutions exist which depends up on the type of problem. For instance, an analytical solution can be derived for a 2D cylinder which vibrates vertically/ horizontally in a potential flow field:

$$m_a = \rho_l D^2 \tag{3.29}$$

where m_a is the displaced mass, ρ_l is the density of the fluid and D is the diameter of the cylinder.

- Time invariant unsteady Stokes equation (used in the current study)
  In Nek5000, we use a time invariant unsteady stokes equation (Eq. 3.30 - 3.31) to calculate the added mass coefficient.

$$(q, \nabla . u_g)_n = 0 \tag{3.30}$$

$$\frac{\beta_0}{\Delta t}(v, u_g)_n + \frac{1}{Re}(\nabla v, \sigma_g)_n - (\nabla . v, p_g)_n = 0 \tag{3.31}$$

where $u_g = (u_{gx}, u_{gy}, u_{gz})^T$ is base velocity vector, σ_g is the stress tensor, p_g is the pressure field obtained by imposing a unit acceleration ($\beta_0(\dot{y}_g^{(n)} - \dot{y}_g^{(n-1)})/\Delta t$ = 1) on the body as boundary condition. The subscripts on the inner product $(.,.)_n$ indicates integration over $\Omega(t^n)$. The force(f_g) represents the added mass contribution and can be explicitly calculated by using Eq.3.32.

Eq. 3.31 is the linear part of the Eq. 2.16 which we have seen early in the Chapter 2. Moreover, the Eqs. 3.30 - 3.31 are similar to the Eqs. 3.15 - 3.16 except that the viscous term is considered here. The obtained force (f_g) from the time invariant unsteady stokes equation, which acts over the body contains the added mass effect. Finally, the added mass can be calculated by Eq. 3.32.

$$m_a = -\Delta t f_g / \dot{y}_g \beta_0 \tag{3.32}$$

Due to the presence of viscosity, the added mass computed by Eq. 3.30 - 3.31 is slightly greater than the analytical solution. However, by reducing the time step and viscosity, this method can predict the actual added mass with significant accuracy.

3.4.4 Implementation of coupling algorithm in Nek5000

Conventional serial staggered in Nek5000

Initially a conventional staggered sequential (CSS) algorithm is developed in Nek5000 to study the FSI problems. It is a loosely coupled method (explicit coupling) which is easy to develop. The Eq. 3.13 is recalled to build the CSS method.

$$(m_s + \overline{m}_a)\ddot{y} + c_y\dot{y} + k_y y = f_{st} - m_a\ddot{y} + \overline{m}_a\ddot{y} \tag{3.33}$$

Depending upon the type of problem, there are two ways to solve this equation. For instance, if there is no added mass effect, the terms with m_a in the Eq. 3.33 can be neglected and the rest of the equation can be solved by using explicit coupling and time schemes. If there is an added mass effect, again there are two ways to solve it (1) Without sub-iterations and (2) With sub-iterations using the Eq.3.34.

$$(m_s + \overline{m}_a)\cdot\ddot{y}\big|_{n+1}^{i+1} + c_y\dot{y}\big|_{n+1}^{i+1} + k_y y\big|_{n+1}^{i+1} = f_{st}\big|_{n+1}^{i} - m_a\cdot\ddot{y}\big|_{n+1}^{i} + \overline{m}_a\cdot\ddot{y}\big|_{n+1}^{i} \tag{3.34}$$

where the sub-iterations and time iterations are denoted as i and n respectively.

If we want to fully eliminate the virtual added mass effect from the Eq. 3.34, then the acceleration term on the left hand side ($\ddot{y}|_{n+1}^{i+1}$) should be equal to the acceleration term on the right hand side $\ddot{y}|_{n+1}^{i}$, otherwise it will become a potential source of instability. Thus, the sub-iterations are necessary to ensure the convergence of $(\ddot{y}|_{n+1}^{i+1}) = \ddot{y}|_{n+1}^{i}$. This method is quite popular and has been used by Yvin et al., 2018b to simulate the flow around a ship and by Young et al., 2012b for the FSI on hydrofoils.

It is interesting to remark that coupling with sub-iteration is an expensive process in DNS even-though it might need only 2-3 sub-iterations. In that case, another option is reducing the time order to maintain the computational expense although the accuracy is reduced. However, if the problem consist of only steady state solutions or if the time step is very small (O^{-8})then the FSI without sub-iteration can be a good choice due to its simplicity and lower computational expense. It can be also noted that the DNS used in this study is time expensive, however the semi-implicit method induces very small time step, so no sub iteration would be needed.

Predictor - Corrector method in Nek5000

An implicit coupling referring to the paper of Fischer et al., 2017 is detailed here and all the future results are generated with this coupling method in this thesis. This implicit coupling is a predictor corrector method where the correction comes from the added mass effect.

We can re-write the Eq.(3.8) to adapt with the temporal scheme used in Nek5000 (BDFk/ EXTk).

$$\frac{m_s}{\Delta t}\sum_{j=0}^{n}\beta_j \dot{y}^{n-j} + k_y y = f_y \tag{3.35}$$

where Δt is the time step and β_j is the temporal scheme coefficients whose values are prescribed in Chapter 2 , n represents the order of temporal scheme and f_y represents the force exerted by the fluid on the hydrofoil in Y-direction.

In this study we split the f_y into two contributions : $f_y = f_{st} + \tau f_g$, where f_{st} is the standard fluid force that would result from Navier Stokes equations with a given body velocity vector $(\dot{y}_{st})$ whose value is predicted by equating the acceleration term to zero $(\beta_0(\dot{\alpha}_{st} + \sum_{j=1}^{n}\beta_j \dot{\alpha}^{n-j})/\Delta t = 0)$. As a result f_{st} is free of added mass effect since the added mass exists only when the body accelerates.

The second part is called f_g, it is the force obtained by solving time invariant unsteady Stokes problem (Eq. 3.30 and Eq. 3.31) and can be explicitly calculated by using Eq.3.32.

Now, the unknown non dimensional factor τ can be obtained by predicting the standard moment (f_{st}) and correcting with added mass force (f_g). The Eq. 3.35 can be written into two components: Predictor and Corrector as shown below:

$$\underbrace{\frac{m_s}{\Delta t}\left(\beta_0 \dot{y}_{st} + \sum_{j=1}^{n}\beta_j \dot{y}^{n-j}\right)}_{\text{Predictor}} + k_y y + \underbrace{\frac{\beta_0}{\Delta t} m_s \dot{y}_g \tau}_{\text{Corrector}} = \underbrace{f_{st}}_{\text{Predictor}} + \underbrace{f_g \tau}_{\text{Corrector}} \tag{3.36}$$

The boundary conditions of predictor ($\beta_0 \dot{y}_{st} + \sum_{j=1}^{n} \beta_j \dot{y}^{n-j} = 0$) and corrector $\beta_0 \dot{y}_g / \Delta t = 1$ parts are applied on Eq.3.36 to get the final form of equation of motion in this implicit coupling method.

$$k_y y + m_s \tau = f_{st} + f_g \tau \tag{3.37}$$

we re-arrange the above equation with damping effect which is proportional to the velocity of the hydrofoil:

$$m_s \tau + c_y \dot{y} + k_y y = f_{st} + f_g \tau \tag{3.38}$$

Thus, the Eq. 3.38 is equivalent to the Eq. 3.14.

The only unknown in the above equation is τ. Once the τ is obtained, it is used for the correction of predicted velocity vector and pressure fields for the next time step. The main part is to set the 2 linear components of velocity vector and pressure field for the whole domain,

$$u_{t+\Delta t} = \underbrace{(u_{st})_t}_{\text{Predictor}} + \underbrace{(\tau u_g)_t}_{\text{corrector}}, \quad p_{t+\Delta t} = \underbrace{(p_{st})_t}_{\text{Predictor}} + \underbrace{(\tau p_g)_t}_{\text{corrector}} \tag{3.39}$$

where $u_{t+\Delta t}$ and $p_{t+\Delta t}$ are the updated velocity vector and pressure fields for the next time step, respectively. u_{st} is the standard velocity field after imposing the initial predicted boundary condition and τu_g is the corrector velocity. Similarly, p_{st} is the standard pressure field after imposing the initial predicted boundary condition and τp_g is the corrector pressure.

If the structural degrees of freedom are more than one, it is quite easy to adapt the above method. Each DOF has to find a solution pair of (u_g, p_g) and it generates a force or torque on the object that corresponds to its DOF. Then a $N_{DOF} \times N_{DOF}$ matrix will be obtained corresponds to the τ in Eq.3.38. The cost of computation increases with increase in degrees of freedoms since the computation of added mass is quite expensive.

The algorithm of Predictor-Corrector method is shown in Fig.3.9:

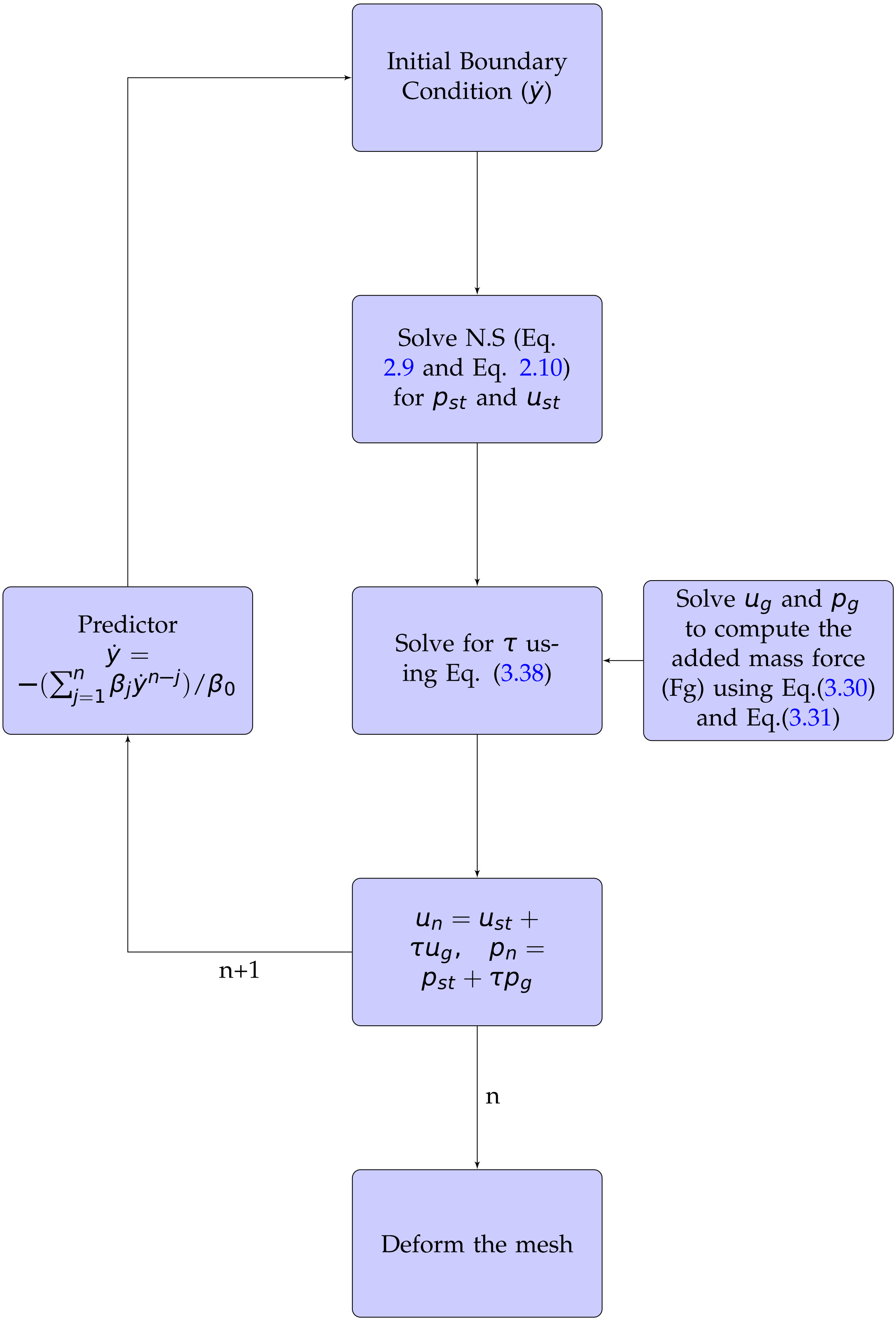

FIGURE 3.9: The algorithm of Predictor-Corrector method used in Nek5000.

3.5 Mesh deformation schemes

In flow with moving domain problems it is necessary to keep the resolution of mesh near the wall without deformation. If unconstrained, the boundary layer mesh can deforms, which can change the wall normal resolution, i.e. $y+$ during the calculation and it leads to accuracy loss. To ensure that wall resolution of the spectral mesh remains unchanged, the mesh is determined using a purely Lagrangian coordinate system in the near wall region and deforms outside of the boundary layer flow. A cylinder vibrating in Y-direction is taken as an example to show the deformed and non deformed boundary layer mesh in Fig. 3.10. The boundary layer mesh topology is deformed in Fig.3.10a, while it is rigidly displaced in Fig. 3.10b i.e. a different scheme is chosen so that it deforms outside of the cylinder region. The deformed boundary layer mesh may lead to an inaccurate results and also leads to negative volumes if the deformation is too large. Different methods are discussed here to rigidly move the boundary layer mesh as the body moves.

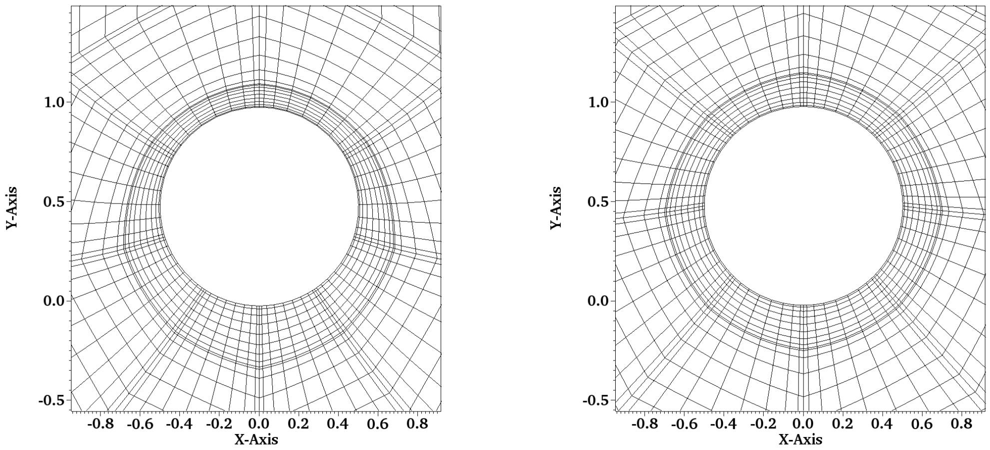

(A) Deformed boundary layer mesh

(B) Non deformed boundary layer mesh

FIGURE 3.10: Mesh deformation in oscillating cylinder (deforming in Y-direction only)

Let's take the above cylinder motion in Y-direction as an example. Mesh deformations within each element is specified by a mesh velocity, $w = dy/dt$ which should be smooth and satisfies the kinematic condition

$$w \cdot \hat{n}|_{\partial\Omega} = u \cdot \hat{n}|_{\partial\Omega} \tag{3.40}$$

where $u(y,t)$ represents the fluid velocity as a function of space y and time t. $\hat{n}$ is the unit normal at the domain surface, $\partial\Omega(t)$. Then the motion of the nodes are computed by integrating $w = dy/dt$ in time. The key idea is to smoothly blend the boundary mesh deformations into the interior of the domain. Depending up on the type of problem (free surface, complex domain etc) different methods can be adopted to deform the mesh. For instance in free surface problems, Ho, 2005 introduced a robust elasticity solver in ALE- SEM formulation to blend the boundary data into the domain interior. However this approach is expensive. To perform mesh deformations, two different methods are implemented in Nek5000.

3.5.1 Laplace equation

The Laplace equation(Eq.3.41) of deformation velocity is used to build a bounded interpolant (Lohner and Yang, 1996). This method ensures a smooth blending of mesh deformation. It does not requires any prior knowledge about the dimensions and topology of the mesh and can be easily adapted to any complex domain problems.

$$-\nabla \cdot \Gamma \nabla u_D = 0 \tag{3.41}$$

where Γ is the diffusivity parameter and u_D is deformation velocity coefficient which ranges from 0 to 1. Once u_D is obtained, it is multiplied with the actual velocity of the object(w) to move the mesh. Diffusivity parameter determines the rigidity of elements and the trend of deformation within the mesh deformation region. The mesh velocity tends to match with the one near the moving object by increasing the diffusivity of nearby elements i.e, as the diffusivity increases, the rigidity of the element increases. Then the diffusivity blends to zero far away from the wall. As a result, mesh deformation occurs in a region where the element are large enough to absorb it, and where the physical gradients are low. There are two ways to compute this diffusivity:

- Depending upon the distance to the wall from nodes (Fischer et al., 2017)

  $$\Gamma(x) = 1 + 9\left(e^{-\epsilon^2}\right) \tag{3.42}$$

  where ϵ is the ratio of Euclidian distance from wall to mesh points and the thickness of the first layer of spectral element (boundary layer) in contact with the given object.

- Depending upon the local element volumes (Masud and Hughes, 1997; Kanchi and Masud, 2007)

  $$\Gamma(x) = \frac{1 - V_{\min}/V_{\max}}{V^e/V_{\max}} \tag{3.43}$$

  where V_{min} is the volume of the smallest global spectral element and V_{max} is the volume of largest global spectral element in the domain. V^e is the volume of the given global spectral element. Typically smallest volume elements are situated near the wall and largest elements are located at the far region. The volume of global spectral elements are considered here instead of the volume of local spectral elements because the size of the local spectral elements varies like a gaussian function with in a global spectral element.

There are some advantages and disadvantages on the above mentioned methods. Fig. 3.11 shows a simple test mesh in order to compare the different deformation schemes. Fig. 3.12 shows the comparison between the two different way diffusivity equation is treated based on the test mesh. The volume of element method is similar to a step function because only 3 types of global spectral elements are present in the Y-direction (directly above the cylinder). The volume of element method gives highest diffusivity near the cylinder wall compared to the node distance method. However, the diffusivity in Node distance method is smoother which helps to have a more progressive deformation. It is necessary when the mesh topology is fine in order to avoid mesh distortion problems.

3.5.2 Smoothing function

If the geometry is not too complex, this method is simple to setup and perform (Barnes and Visbal, 2016). It gives freedom to the user to define a mesh deformation as needed. The main idea is to directly compute u_D which ranges from 0 to 1 using a simple exponential function depending on the geometry and mesh topology. However, a prior knowledge about these parameters are required in this method. The mesh close to the body will have a blending velocity coefficient of 1. Similarly, 0 at the external boundary wall. In between the body and external boundary wall, the value of blending velocity coefficient goes from 1 to 0. A blending function is used to generate u_D using the position of the grid points, see Eq. 3.44. Depending upon the refinement of the mesh topology, the deformation zone can be explicitly

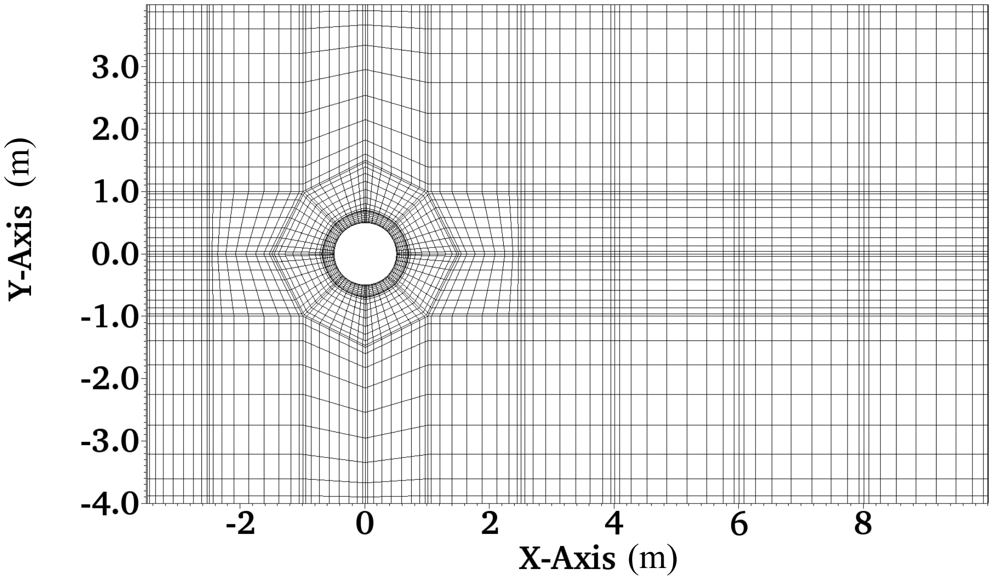

FIGURE 3.11: A sample mesh taken for validation of mesh deformation schemes where N = 48 and O(10).

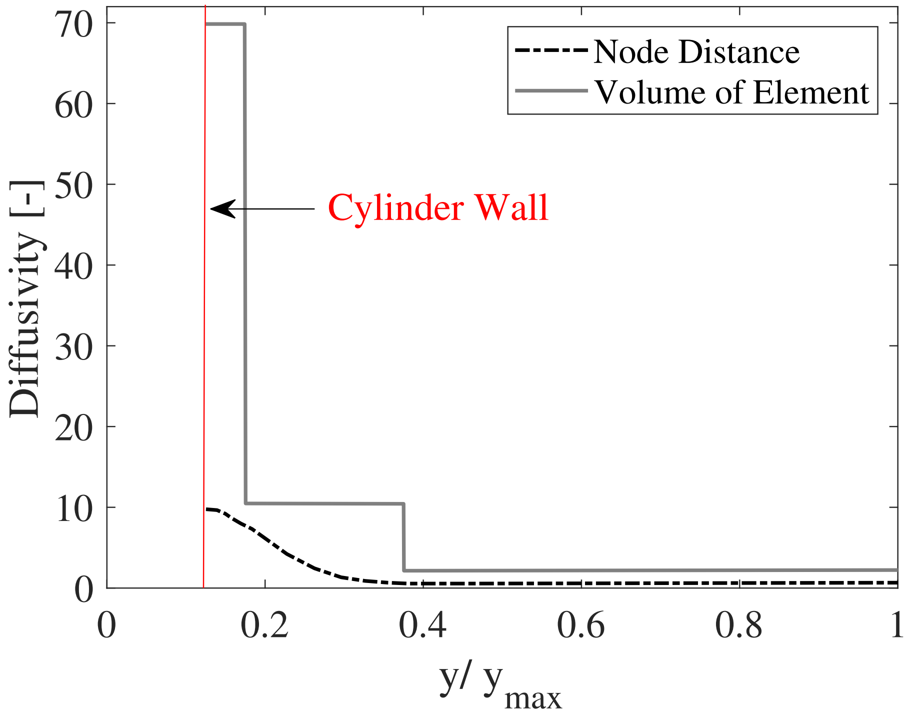

FIGURE 3.12: Diffusivity comparison on a cylinder mesh (presented in Fig. 4.2)

adjusted by using the parameters.

$$u_D = \frac{1}{1 + (exp(\eta - \eta_{mid}))/\Delta} \tag{3.44}$$

where η_{mid} is the mid point of the slope in Y-direction, η is the normal distance to the grid points from the foil wall and Δ is the slope required for blending. Fig. 3.13 shows the comparison of all the methods in terms of deformation velocity coefficient based on test mesh as shown in Fig. 3.11. The u_D obtained from smoothing function method can rigidly move more area where boundary layer develops compared to other two methods. But the deformation rate is quite high compared to other methods especially in the region of $0.4 < y/y_{max} < 0.6$ i.e, most of the deformations are forced to happen in this region. In the volume of element method, small jerks are observed due to the steps in diffusivity which may lead to mesh distortion. The most smoother method is the node distance method.

As far as computational expense is concerned, computing u_D using Laplace equation is almost 6 times longer than the Smoothing function method i.e about the same time of the resolution of fluid flow for one time step. However, this coefficient has to be calculated only once at the beginning of the simulation in most of the fluid dynamics applications. So, It can be concluded that the computational expense is not an important factor in the selection of appropriate mesh deformation scheme.

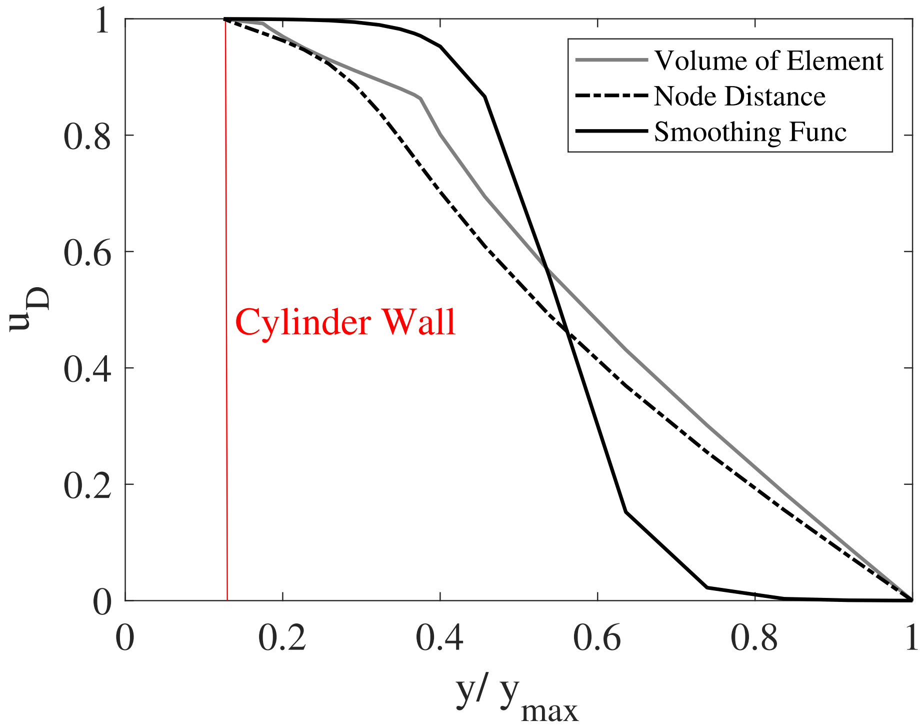

FIGURE 3.13: Deformation velocity coefficient comparison on a cylinder mesh (presented in Fig. 4.2)

3.6 Conclusion

Initially we presented some non-dimensional numbers to classify the fluid structure interaction problems. Then, the mathematical resolution of the FSI problem is discussed in detail. Then, the numerical resolution is mentioned, followed by different coupling methods associated to it. Mainly two different couplings were discussed, one is weak coupling (explicit) and second is strong coupling (implicit). Weak coupling is simple and easy to develop however stability and accuracy is an issue whereas strong coupling over comes this issue but is more expensive and difficult to implement. Thus, we have decided to move forward with both methods to test which one is more suitable. In order to do that, we have selected a CSS (Conventional Serial Staggered) algorithm for the explicit coupling and predictor- corrector algorithm for implicit coupling. A brief discussion about the computation of added mass is also carried out because we will have added mass issue in the future calculations. Finally a detailed study about the different mesh deformation schemes is carried out. There are two ways discussed in this thesis to deform the mesh smoothly from the interior to exterior boundaries. Both methods are implemented and tested in Nek5000 and finally, the deformation based on smoothing function is selected to perform the mesh deformation because of its simplicity and customizability.

Chapter 4

Validation of Developments

Summary

This chapter presents detailed validation studies on the mesh deformation schemes and resolution of fluid-structure coupling methods that were carried out in Nek5000. We will compare our results with well documented literatures. Two different test cases are considered for the validation: 1) An oscillating cylinder (Forced/ FSI) at low Reynolds number, 2) Self sustained pitching of airfoil at a transitional Reynolds numbers. The obtained results are validated with hydrodynamic coefficients, displacement of the body and spectral analysis.

4.1 Introduction

First, a cylinder oscillating in laminar flow regimes is considered to be able to validate the coupling into Nek5000 with a low computational expense. Moreover, there are many well documented cases available in forced and free motions of cylinder at low Reynolds number. In this study the first objective is to validate the proposed mesh deformation scheme with the Arbitrary-Eulerian-Lagrangian (ALE) formulation of Nek5000 before proceeding to couple the Fluid and Structural equations. Later, a Vortex Induced Vibration on the cylinders(VIV), study which happens in a low range of reduced velocity ($5 < U_R < 10$) is performed to test the coupling algorithm. Both explicit (using CSS algorithm) and implicit coupling (predictor/ corrector method) are developed for the validation. Finally, the DNS solver is coupled with 1-DOF pitching motion to validate the method in transitional Reynolds number on a NACA0012 airfoil prior to the higher Reynolds number case on NACA6612 hydrofoil.

4.1.1 Validation of ALE and mesh deformation

In this section a 2D cylinder is forced to oscillate in Y-direction with a certain amplitude (A) and frequency (f_o). This case was already studied experimentally by Koopmann, 1967 and numerically by Placzek et al., 2009. The motion of the cylinder can change the vortex shedding frequencies in the wake and some interesting physics can be observed such as "lock-in" phenomenon at certain frequency of oscillations. Lock-in is a phenomena when the vortex shedding frequency and the oscillation frequency of the body becomes into a single frequency. In addition to the validation of mesh deformation and ALE formulation, a brief study of lock-in is also carried out because it determines the quality of mesh deformation scheme.

Problem Setup

The computational domain and the spectral mesh is shown in Fig.4.1 and Fig.4.2 respectively. The results are sensitive to the confinement effects especially at low Reynolds numbers, so the total height (H) of the simulation domain is chosen as $24D$ where D is the diameter of the cylinder. The cylinder is positioned at (0,0) and the length of the domain from the centre of the cylinder to the outlet is 35D and and 12D to the inlet. There are 1348 elements with spectral element order of 6 resulting in 48528 grid points. Upper and lower boundaries are set to symmetric boundary conditions to avoid the development of boundary layer. $\nabla U \cdot x = 0$ is set at the outlet whereas a moving wall condition is set on the cylinder surface. The

Reynolds number is set to 100 and the simulation is restarted from a well converged static case at the same Reynolds number where the von Kármán shedding patterns are already developed (not shown here). A 7^{th} order polynomial approximation is used for velocity whereas a 6^{th} order approximation is chosen for the pressure. The convective terms are advanced in time using an extrapolation of O(3), whereas the viscous terms use a backward differentiation of O(3).

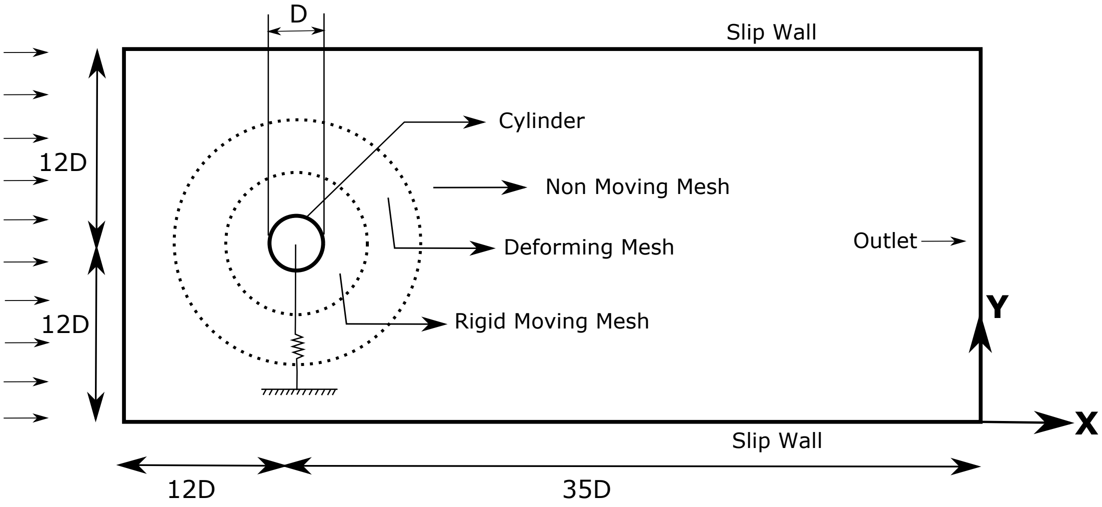

FIGURE 4.1: The simulation domain of a 2D cylinder for flexible cylinder

The cylinder motion is prescribed as :

$$y(t) = Asin(F\omega_s t) \tag{4.1}$$

where F is the frequency ratio ($F = f_o/f_s$) in which $f_s = 0.1667Hz$ is the frequency of vortex shedding of the static cylinder at Re =100, f_o is the frequency of oscillations and $\omega_s = 2\pi f_s$. $A = Ay/D$ = 0.25 is the amplitude ratio of oscillation and it is constant for all cases.

Four different cases are studied, with different frequency ratios (F) namely, Case 1 : F = 0.5, Case 2 : F = 0.9, Case 3 : F = 1.1, Case 4: F = 1.5. According to the results from Koopmann, 1967 and Placzek et al., 2009, the lock-in phenomena is observed in the cases where the oscillation frequencies are close to the vortex shedding frequencies. Thus, Case 2 and Case 3 should observe the lock-in phenomena.

Results and Discussion

A good agreement is observed between the results from Nek5000 and reference results. It is important to note that the amplitude of spectra from Nek5000 is modified to match with the reference results since the reference results are computed in Power

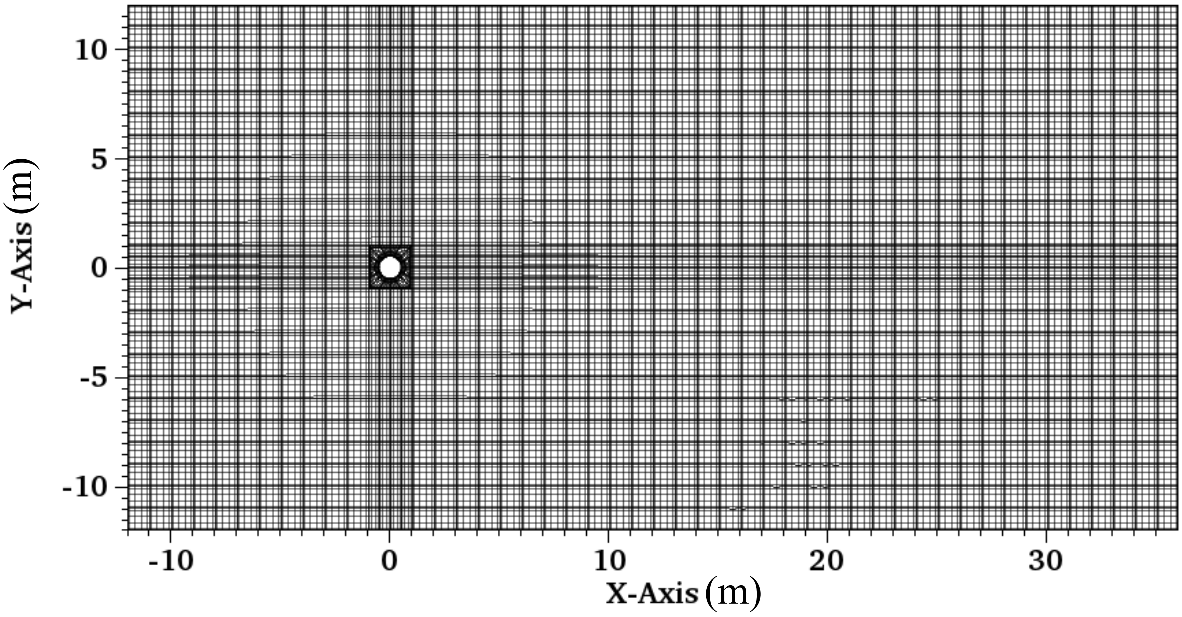

FIGURE 4.2: The spectral element mesh of 2D cylinder, N = 1348, O(6)

Spectral Density (PSD) whereas we only calculated the amplitude of the signal using fast Fourier Transform (FFT). The results of Case 2 (F = 0.9) and Case 3 (F = 1.1) are shown in the Fig.4.3 and Fig. 4.4. As expected, only one main frequency in the spectral analysis diagram of lift coefficient is observed at $f/f_o = 1$ which implies the occurrence of lock-in phenomena. Moreover, the coefficient of lift is purely sinusoidal as mentioned in Nobari and Naderan, 2006. It is also observed that the values of C_D are increased by 10% for the Case2 and 25% for Case 3 compared to that of the static case where $C_D = 1.37$. The maximum value of lift coefficient of Case 2 is decreased by 10% compared to that of static case where $C'_{L,max} = 0,33$ (where C'_L is the fluctuation of coefficient of lift), however it is increased drastically in Case 3 by 440%. In Case 2 and Case 3 the forces acting on the cylinder is induced by the both vortex shedding and the applied forced due to lock-in. A quantitative comparison of the values of C_D and C_L are shown in the Table.4.1.

TABLE 4.1: Comparison of C_L and C_D with the reference at Re = 100, F = 0.9 and F = 1.1. (The reference results are obtained from Placzek et al., 2009)

F	$C'_{L,max-REF}$	$C'_{L,max\text{ - Nek}}$	mean(C_{D-REF})	mean($C_{D\text{ - Nek}}$)
0.9 (Case 2)	0.288	0.296	1.50	1.49
1.1 (Case 3)	1.478	1.480	1.75	1.75

The results of Case 1 is shown in Fig. 4.5 and Case 4 is shown in Fig. 4.6. For these configurations, no lock-in phenomena is found and unlocked wake is observed from the spectra. Moreover, it shows a good agreement with the reference results. It

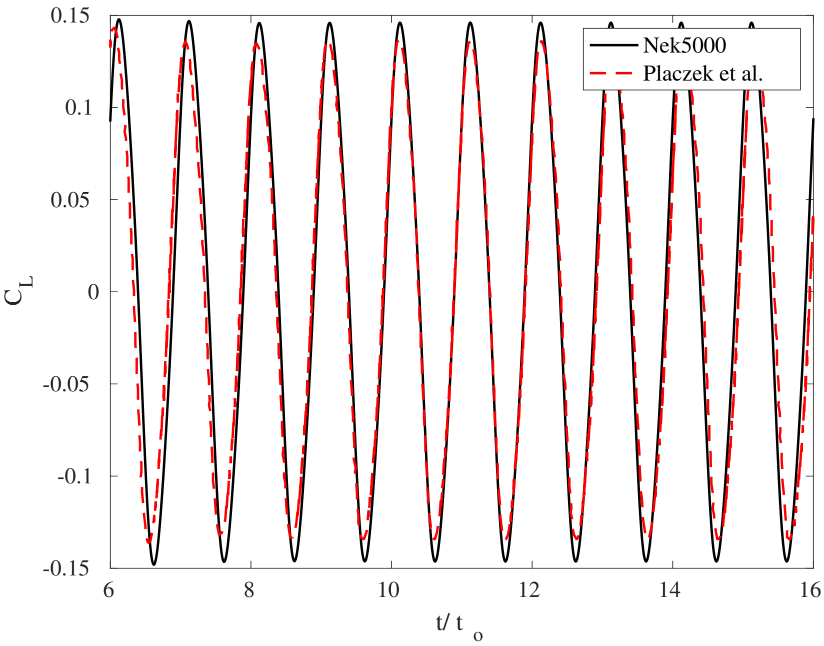

(A) Time evolution of lift coefficient

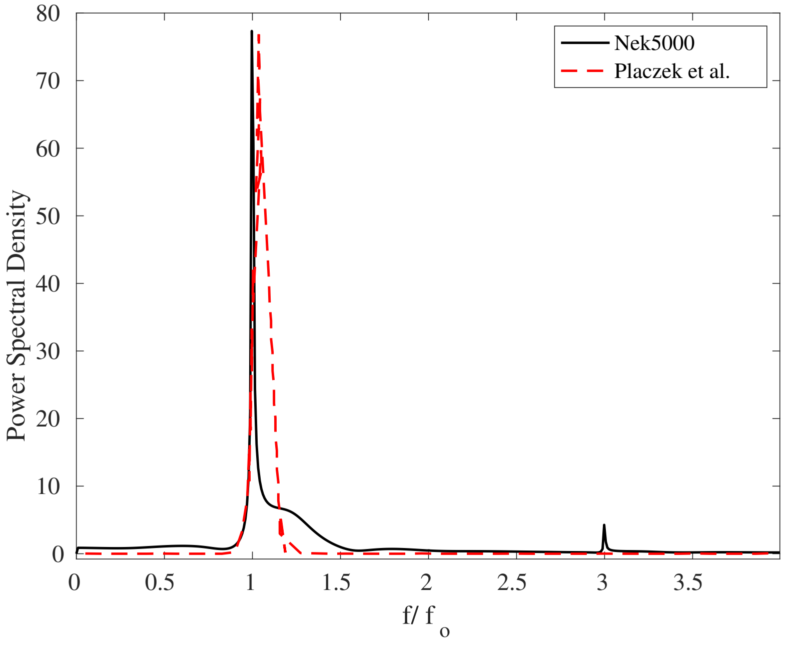

(B) Spectra of the lift coefficient.

FIGURE 4.3: Cylinder lift coefficient response and its spectral analysis of Case 2 at Re = 100 and F = 0.9

is also observed that the, C_L is no more purely sinusoidal signals and a beating response is observed. There are two main frequencies observed in the spectra for the Case 1 and Case 4. In both cases, the oscillation frequencies f_o are observed at

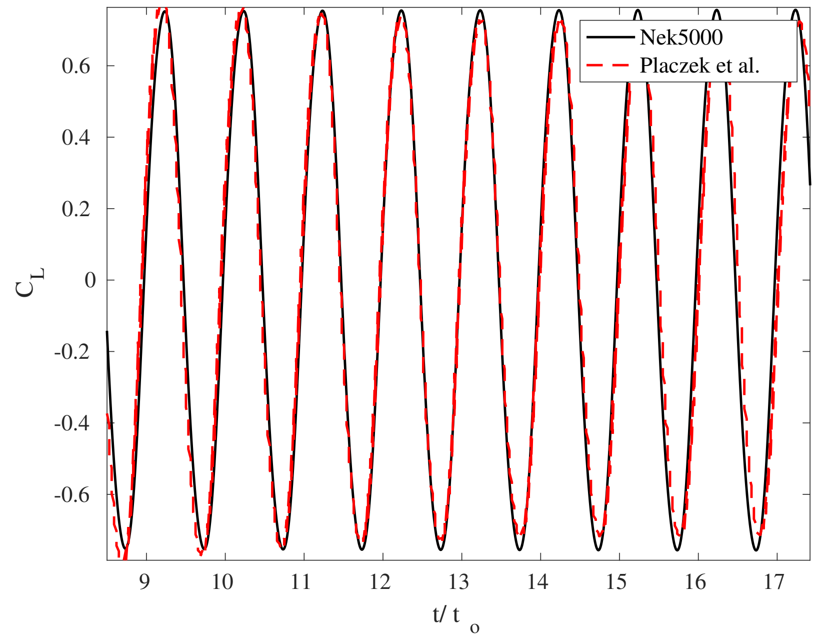

(A) Time evolution of lift coefficient

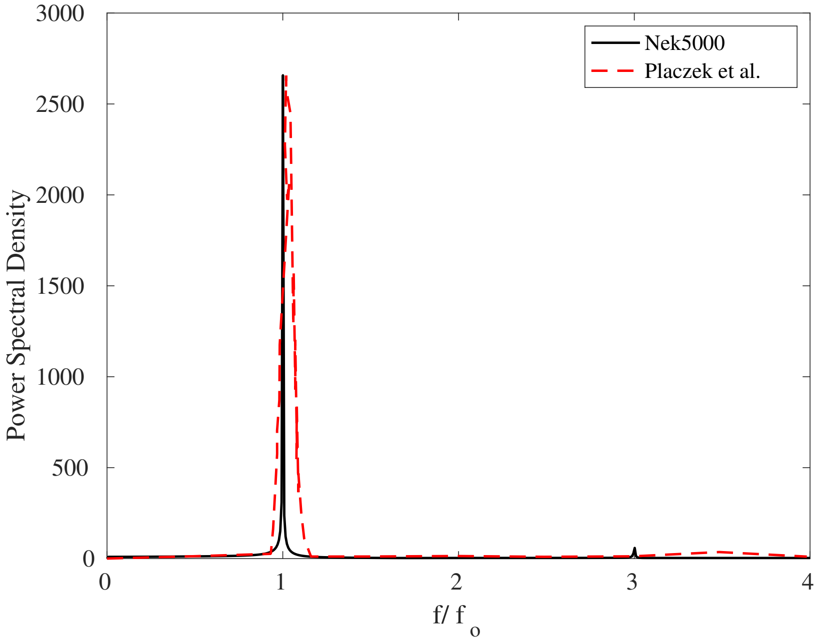

(B) Spectra of the lift coefficient

FIGURE 4.4: Cylinder lift coefficient response and its spectral analysis of Case 3 at Re = 100 and F = 1.1

$f/f_o = 1$. In Case 1, a main peak is observed at $f/f_o = 2$, which corresponds to the Strouhal frequency. In Case 4, the main peak is due to the oscillation frequency where the Strouhal frequency is reduced. Placzek et al., 2009 also remarked that the

Strouhal frequency govern the system at a region lower to the lock-in whereas the cylinder oscillation frequency is dominating above the upper limit of lock-in.

The Fig. 4.7 and Fig. 4.8 shows the vorticity patterns developed in different forced cylinder cases and its frequency is quantified as shedding frequency in Table 4.2. It can be clearly seen that the vortex shedding frequencies/ patterns are altered to match with the oscillation frequencies in the lock-in region Fig. 4.7 (b) and (c). In Case 2, the vortex shedding frequency is reduced whereas in Case 3 it is increased and leading to have lock-in phenomena. The vortex shedding frequency in Case 1 is increased as compared to that of the stationary cylinder. Different vortex shedding periodicity is observed in the wake of Case 4 (see, Fig .4.8 (Nek5000)) including oscillation, Strouhal and beating frequencies. Placzek et al., 2009 mentioned that the beating frequency is the governing frequency in the wake of Case 4. A good similarity is also observed by a qualitative comparison between the Case 4 Nek5000 vorticity field with the reference vorticity field (see, Fig. 4.8).

TABLE 4.2: Comparison of Strouhal frequency (f_S) with Placzek et al., 2009 at Re = 100, F = 0.5 and F = 1.5

F	(f_{S-REF})	($f_{S\text{ - Nek5000}}$)
0.5 (Case 1)	2.03	2.03
1.5 (Case 4)	0.667	0.664

Finally, the Fig. 4.9 shows the different simulations performed in this validation study are summarized on the Williamson-Roshko map. It shows that the vortex mode shapes are different in each cases. However, the modes observed in our study is not exactly the same as in Williamson-Roshko map, possibly due to the low Reynolds number in our study ($Re = 100$) whereas the Williamson-Roshko map is observed at $300 < Re < 1000$.

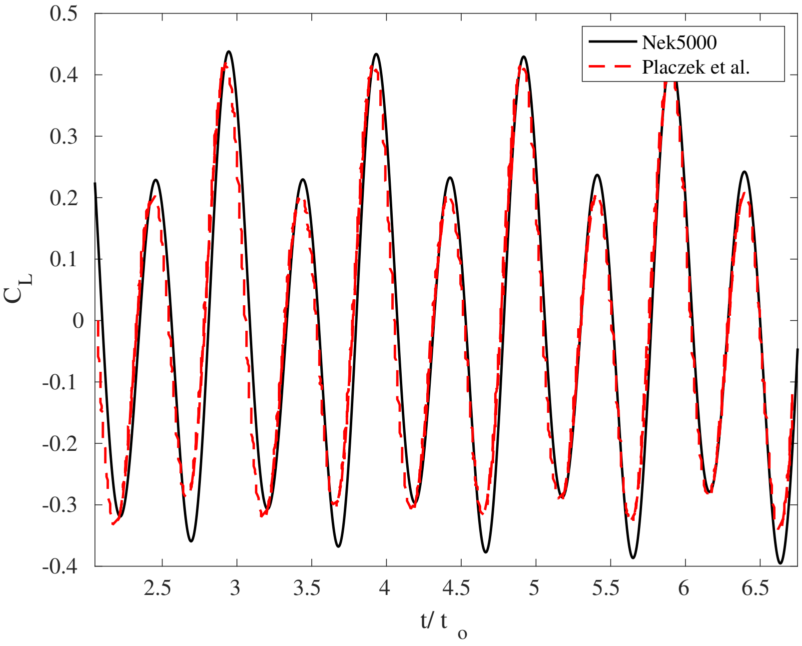

(A) Time evolution of lift coefficient

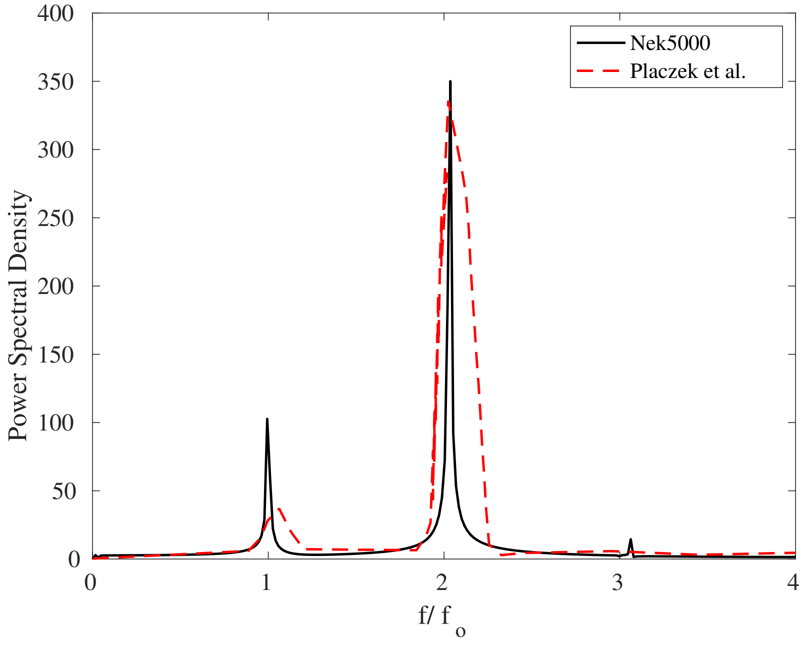

(B) Spectra of the lift coefficient

FIGURE 4.5: Cylinder lift coefficient response and its spectral analysis of Case 1 at Re = 100, A = 0.25, and F = 0.5

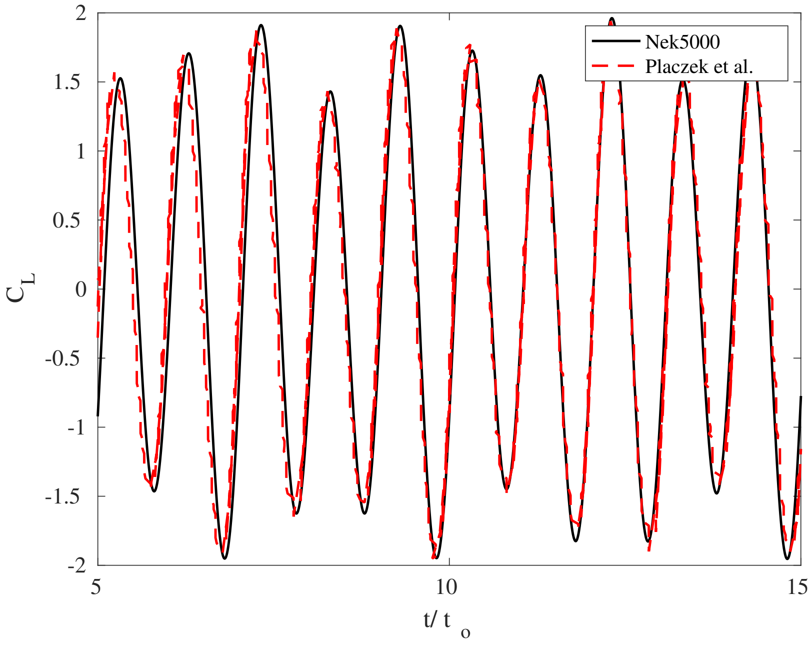

(A) Time evolution of lift coefficient

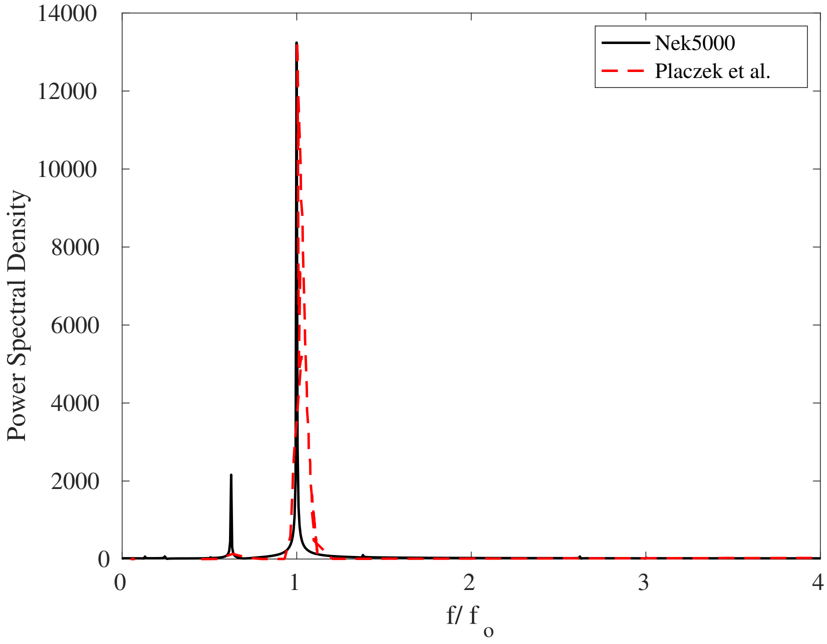

(B) Spectra of the lift coefficient

FIGURE 4.6: Cylinder lift coefficient response and its spectral analysis of Case 4 at Re = 100, A = 0.25, and F = 1.5

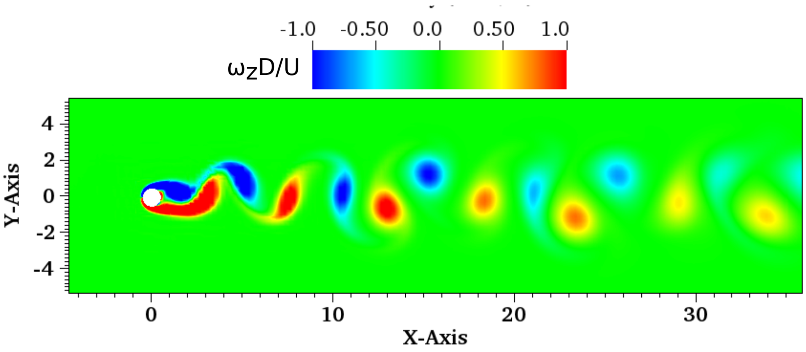

(A) A = 0.25, F = 0.5 (Case 1)

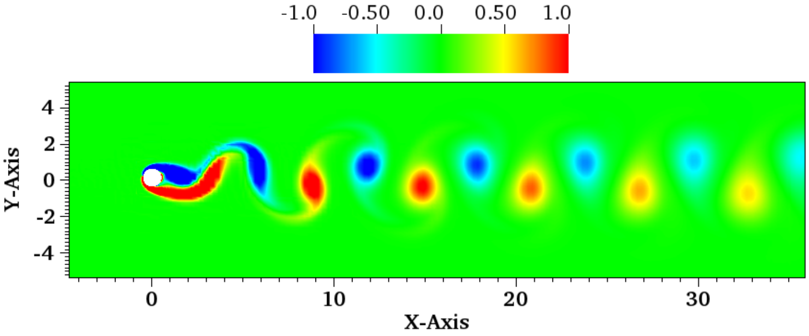

(B) A = 0.25, F = 0.9 (Case 2)

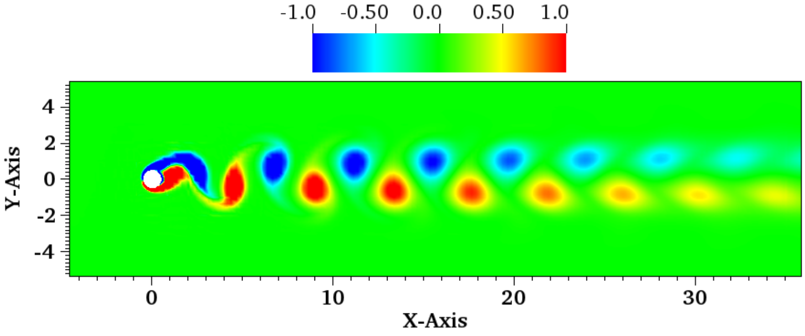

(C) A = 0.25, F = 1.1 (Case 3)

FIGURE 4.7: Vortex shedding modes inside and outside the lock-in zone for the cylinder undergoing forced vibration.

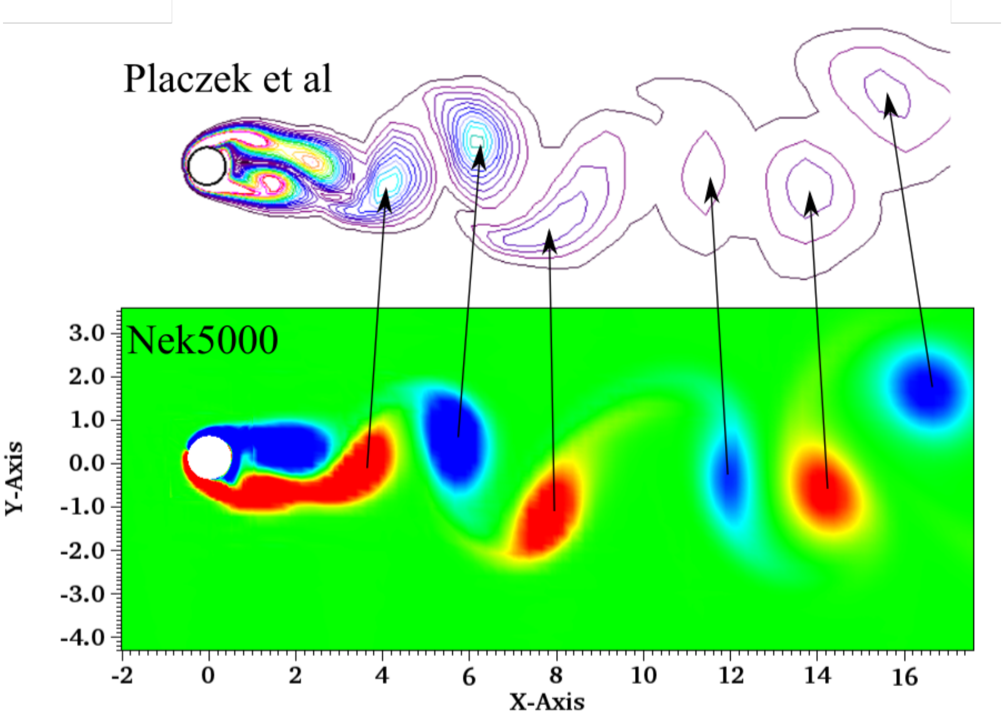

FIGURE 4.8: Instantaneous vorticity contour comparison of Case 4 (A = 0.25, F =1.5) with Placzek et al., 2009

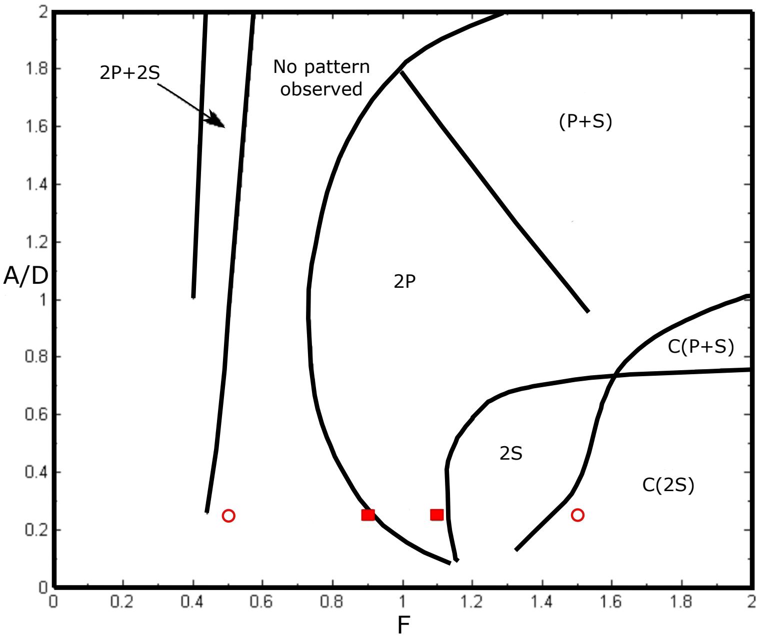

FIGURE 4.9: Representation of our results on the Williamson-Roshko vortex shedding mode map in F - scale (Williamson and Roshko, 1988). The red filled squares indicate the lock-in observed cases, whereas the empty ones are the not synchronized cases. The Y-axis is the amplitude of oscillation non-dimensionnalized by the diameter of the cylinder.

4.1.2 Validation of explicit and implicit couplings without added mass

The objective of this test case is to validate the coupling algorithm by analysing the motion of cylinder under the influence of vortex shedding and vice versa. Both explicit and implicit couplings are used for the study. However, only the results of implicit coupling is shown in this thesis for the clarity and simplicity, although both are giving the same results. From the static and forced cylinder cases, it is observed that the vortex shedding in the wake makes an oscillating drag and lift forces. Moreover, it may result in the vibration of the cylinder. Thus, the amplitude (A) and frequency response is not known prior to the simulation.

Problem Setup

Let us re-write the Eq. 3.14 in the non dimensional form, considering that the added mass is neglected due to the lower mass number (M = 0.1). Thus we have,

$$\ddot{y} + 4\pi F_N C_y \dot{y} + (2\pi F_N)^2 y = \frac{2C_L M}{\pi} \quad \text{for } (0, T) \tag{4.2}$$

where $\ddot{y}, \dot{y}, y$ are the normalised cross flow acceleration, velocity, displacement of the body respectively (the free stream flow is assumed to be in be x-direction). M is the mass number, C_L is the coefficient of lift, C_y is the damping coefficient in y direction and F_N is the reduced natural frequency $F_N = f_N D/U$ where D is the diameter of the cylinder, U is the free stream velocity and f_N is the natural frequency of the oscillator.

The computational domain and mesh of the current test case is the same as it is used in the previous forced motion case (Fig. 4.1 and Fig. 4.2 respectively) including the convergence criteria's and spectral element order (N). The boundary conditions are also the same as the forced case except that the cylinder is supported with a spring at the centre of mass and it is free to oscillate in Y-direction. The blockage ratio (D/H) of the system is 4% where H is the cross sectional length of the computational domain. For the sake of simplicity and in order to have high amplitude of oscillations, we removed the damper from the system. The mass number is set to 0.10 and the natural frequency f_N of the system is computed from the Strouhal frequency of the static cylinder at Re = 100. The computations are carried at a variable time step under the condition of CFL ≈ 0.6. In this study, different Reynolds numbers are considered at an increasing order and the non-dimensional natural frequency is changed with the Reynolds number.

Results and discussion

The validation is based on the amplitude ratio (y_{max}/D) of the cylinder oscillation, the frequency ratio (f_S/f_N) at different Reynolds number, where f_S is the vortex shedding frequency and f_N is the natural frequency. A comparison between vortex shedding modes at selected Reynolds numbers are also presented. The results in Fig. 4.10 (a) shows a good comparison with the results obtained by PRASANTH and MITTAL, 2007 in terms of both amplitude and frequency ratios. As observed in the literature, a synchronisation/ lock-in region is detected in the Fig. 4.10 (b) over a large range of Reynolds number. This region can be also called a resonant region because the amplitude of oscillation increased when the $f_S/f_N \approx 1.0$.

Slight differences in the transition between each branches are observed. These mismatches are associated to the difference in blockage ratio. The reference results are made with a blockage ratio of 1% and current results are made with 4%. PRASANTH and MITTAL, 2007 also remarked that the increase in blockage ratio leads to an early jump in cylinder response at a smaller Reynolds number. It can be due to the increase in local acceleration of the fluid flow around the cylinder when blockage ratio increases. This difference is observed in Fig. 4.10. However, the objective of this test case is not to capture all the branches accurately but to validate the code by an overall performance.

The Fig. 4.11 and Fig. 4.12 shows the comparison between vortex shedding patterns obtained at selected Reynolds numbers in Nek5000 and PRASANTH and MITTAL, 2007 . The vortex shedding patterns are similar to that of the reference results. At low amplitude of oscillations (initial branch), a classical 2S type mode shedding is observed at Re = 75 and a good comparison is observed between the vortex patterns (see, Fig. 4.11(a)). Then, the cylinder jumps to a lower branch and starts to oscillate at higher amplitudes where a change in pattern from 2S to C(2S) type vortex shedding is observed (see, Fig. 4.11 (b)) i.e, the vortices in the wake coalesce and leads to C(2S) type of vortex pattern. But, Nek5000 predicts it at slightly lower Reynolds number i.e, Re = 84 (Fig .4.11(b)) as compared to Re = 86 in the reference. The possible reason behind this small difference is mentioned before, regarding the blockage ratio. In both cases (reference and Nek5000), the vortex shedding frequency starts to merge with the natural frequency of the cylinder when 84 $<$ Re $<$ 130. In this range, the longitudinal distance between vortices increases and results in a lower non-dimensional shedding frequency when Re increases (see Fig. 4.12(a)).When Re>130 the longitudinal distance between vortices decreases and it comes back to the wake structure of flow past a stationary cylinder (see Fig.4.12(b), at Re = 140) and these changes are correctly captured in Nek5000 and compared well with the reference.

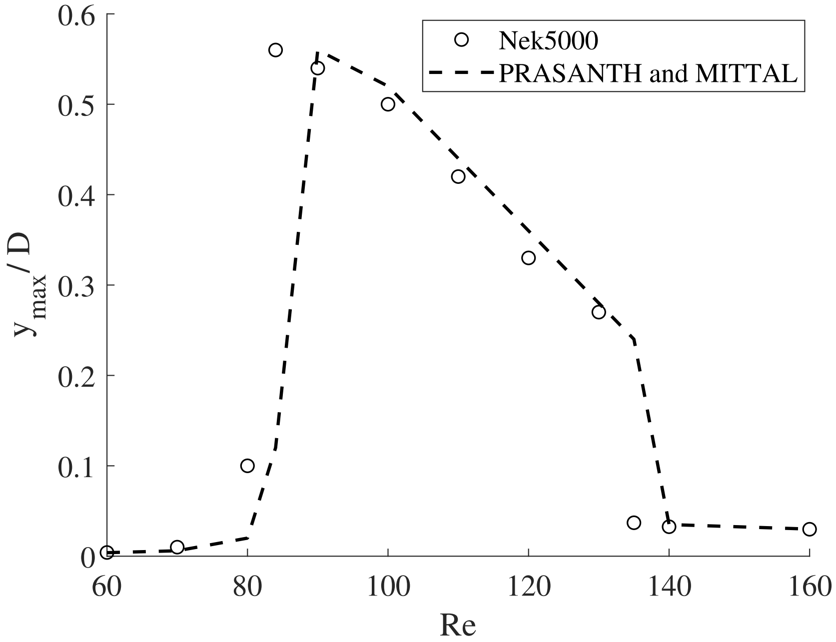

(A) Amplitude of transverse oscillation of cylinder at increasing order of Reynolds number

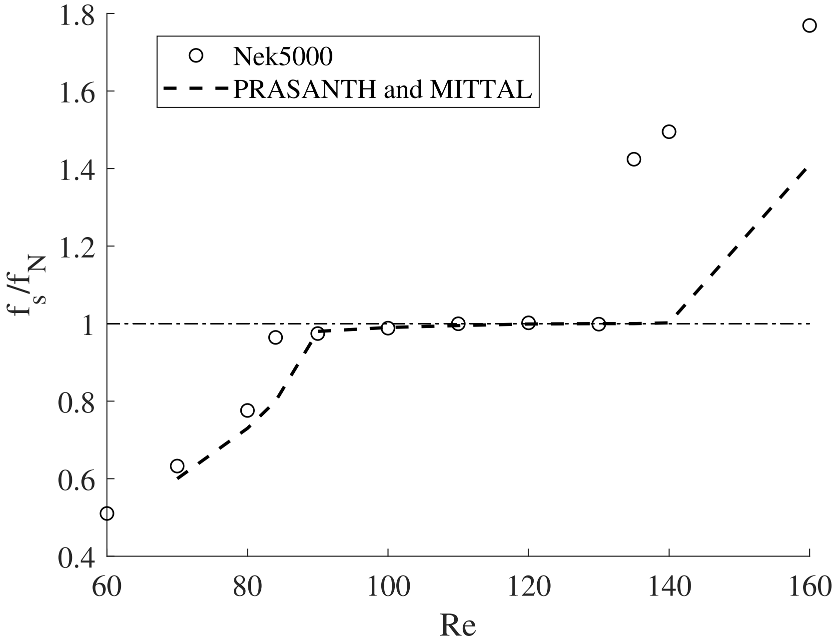

(B) Frequency ratio of cylinder at different Reynolds numbers

FIGURE 4.10: Results of VIV of cylinder at different Reynolds numbers. The reference results are obtained from PRASANTH and MITTAL, 2007.

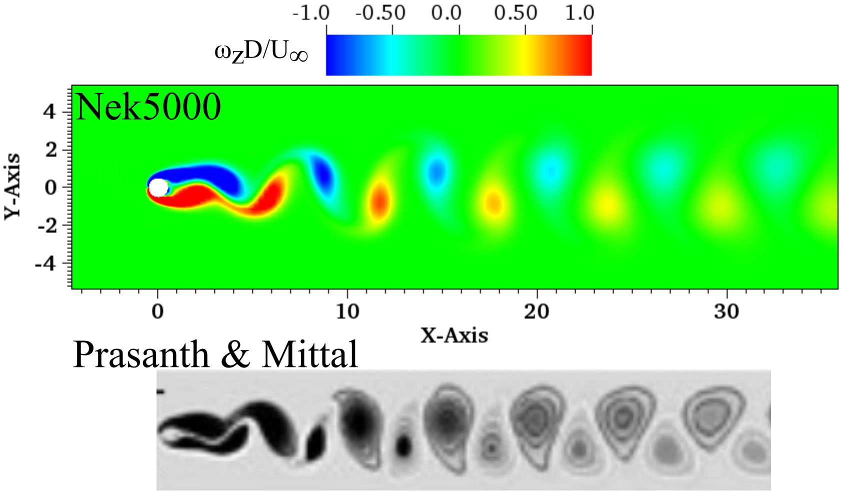

(A) Re = 75

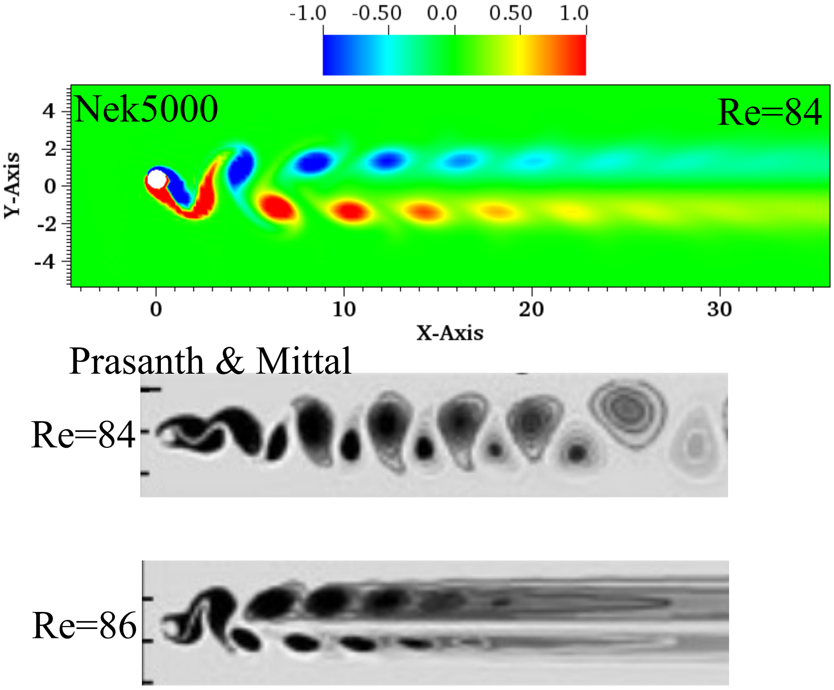

(B) Re = 84

FIGURE 4.11: Instantaneous non-dimensional vorticity ($\omega_z D/U_\infty$) at various values of Reynolds number for the 4% blockage.

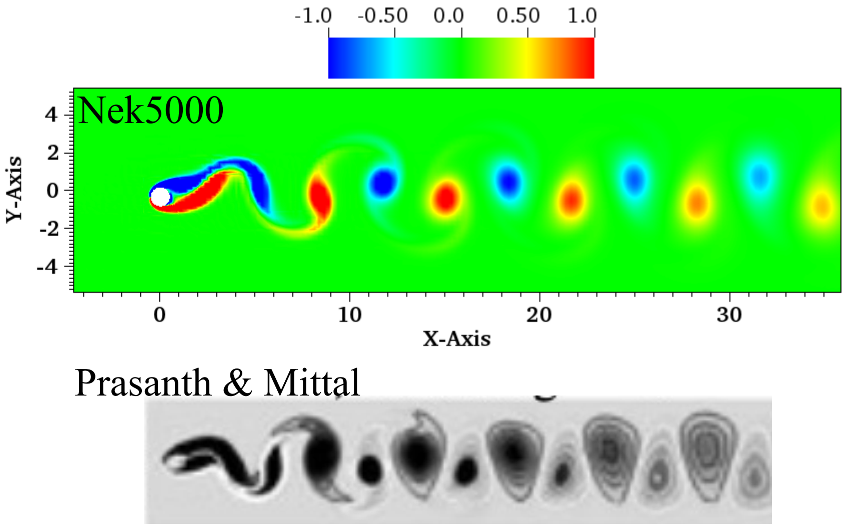

(A) Re = 120

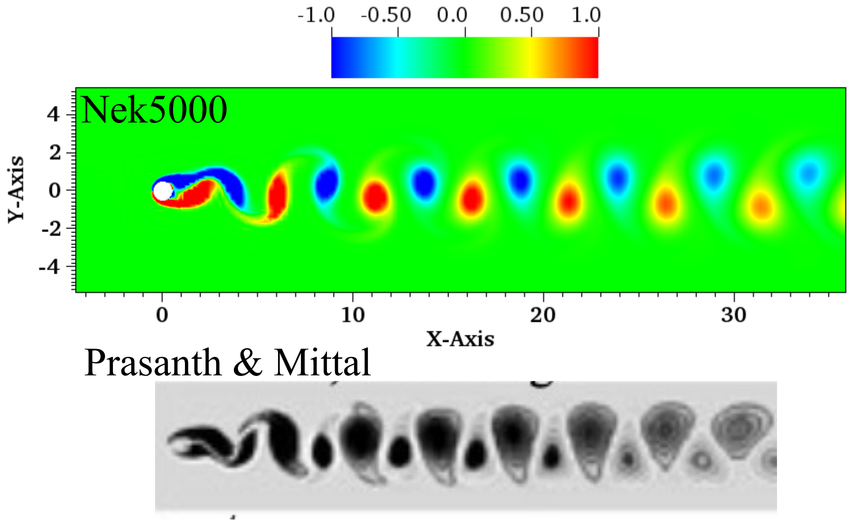

(B) Re = 140

FIGURE 4.12: Instantaneous non-dimensional vorticity ($\omega_z D/U_\infty$) at various values of Reynolds number for the 4% blockage.

4.1.3 Validation of explicit and implicit couplings with added mass

The aim of this section is to validate the coupling method when the added mass effect is not negligible. In the previous validation case, the added mass instability was neglected so the coupling scheme was stable in both explicit and implicit methods. The explicit and implicit couplings will be compared to each other in this section since both schemes are validated against literature in the previous section. In order to bring the added mass effect on the previous VIV case, we have considered a cylinder without any mass i.e $\rho_s = 0$ and $\rho_l = 1$, and the only present mass is the added mass. The Reynolds number is 100 and the stiffness remains the same. The case is started with an initial condition of a well developed von Kármán shedding at Re = 100. The Eq.3.34 and Eq.3.38 are retained to study the added mass effect on explicit coupling and implicit coupling respectively.

$$(m_s + \overline{m}_a) \cdot \ddot{y}\Big|_{n+1}^{i+1} + c_y \dot{y}\Big|_{n+1}^{i+1} + k_y y\Big|_{n+1}^{i+1} = f_{st}\Big|_{n+1}^{i} - m_a \cdot \ddot{y}\Big|_{n+1}^{i} + \overline{m}_a \cdot \ddot{y}\Big|_{n+1}^{i} \tag{4.3}$$

$$\frac{\beta_0}{\Delta t} m_s \tau + c_y \dot{y} + k_y y = f_{st} + f_g \tau \tag{4.4}$$

The force computed in explicit coupling scheme consist of an additional opposing force called added mass force to the standard force in CFD solver. It is because of the phase lag of structural motion as compared to the prediction of fluid force. In effect, the force is defined as Total Force Explicit ($f_{st}|_{n+1}^{i} - m_a \cdot \ddot{y}|_{n+1}^{i}$) where f_{st} is the standard force and m_a is the added mass. The added mass force is negative because it is opposite to the pressure force. In order to remove this added mass from the Total Force Explicit and to stabilize the 1DOF system, a correction term ($\overline{m}_a \cdot \ddot{y}|_{n+1}^{i}$) is added on both side of the EOM as shown in Eq. 4.3.

In Fig. 4.13, the force obtained with and without correction using explicit coupling is compared to the force obtained with the implicit coupling where the add mass is corrected implicitly (see, Section 3.4.4). Both explicit and implicit couplings give same results after the correction, hence the CSS coupling with correction of added mass is validated. In effect, this method is stable only when the time order is equal to 1 which may cause accuracy loss in unsteady cases. In order to achieve better accuracy, sub-iterations are required and is computational expensive.

Since both standard forces are well matched, let us look at the results of VIV case with the presence of added mass. The validations are carried out to compare the amplitude of oscillations from explicit and implicit coupling schemes. Fig.4.14 shows a very good comparison of amplitude from both coupling schemes even though the time order of explicit coupling is 1. Moreover these results are compared well with

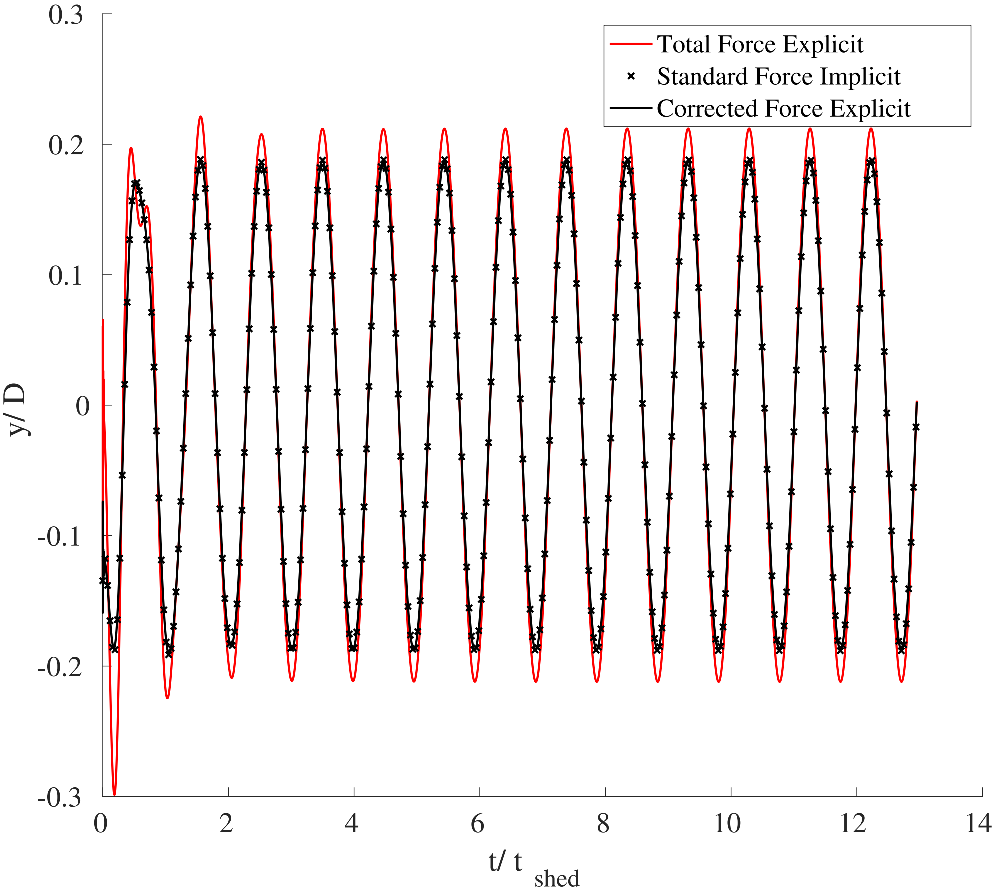

FIGURE 4.13: Force comparison between explicit and implicit schemes

the results of Fischer et al., 2017 where the amplitude ratio of oscillation, $A_{ref} = 0.0242$ against A=0.0240 in our case.

4.1.4 Validation of Coupling between 1-DOF pitching & Nek5000 on a transitional flow past a NACA0012 airfoil

A self sustained pitching NACA0012 airfoil at $Re = 64,000$ is investigated in this section. It is one of the well known aeroelastic problem and probably one of the preliminary methodical works on an aeroelastic problem at transitional Reynolds numbers. This case is physically closer from the current work even though the Reynolds number is one order less. It was originally investigated experimentally by Poirel et al., 2008. The authors observed self sustained limit cycle oscillations at low frequency with in the Reynolds number range of 4.5×10^4 to 1.3×10^5. This low frequency oscillations are not related to the von Kármán vortex shedding in the wake, which is about two orders higher than the LCO. These higher frequencies of vortex

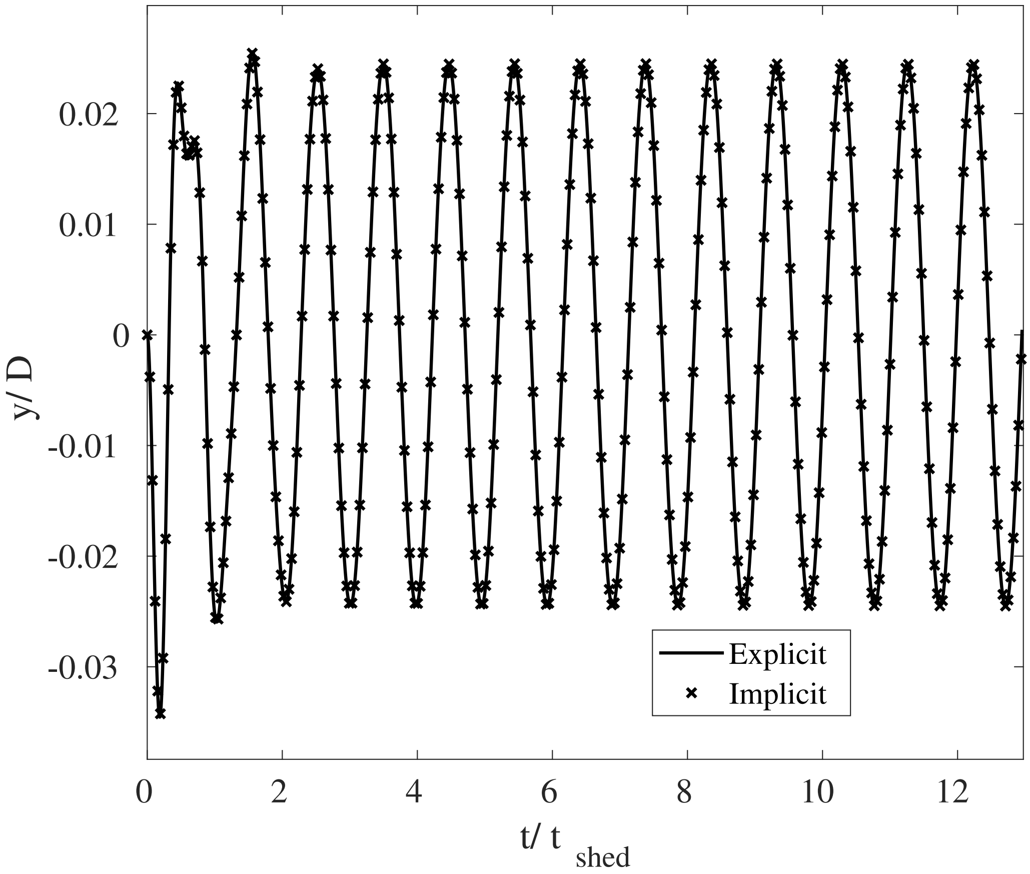

FIGURE 4.14: Amplitude comparison between explicit and implicit schemes

shedding do not have any influence on the self sustained LCO. Thus, the vibration due to the vortex shedding in the wake is no longer valid for this case. Although the Reynolds number is much lower as compared to the current thesis work, laminar separation bubble occurs along the chord and transition to turbulence occurs that induces large pitch motions, which eventually generates LCO. Later, numerous numerical studies were conducted to investigate the effect of laminar separation in this unsteady problem (Poirel and Yuan, 2010; Poirel et al., 2011; Poirel et al., 2011; Lapointe and Dumas, 2011; Poirel and Mendes, 2014a; Yuan et al., 2015). We validate the amplitude and frequency responses of the LCO along with the coefficient of friction, which is a method used to accurately locate the position of LSB.

Problem Setup

The experimental setup of this problem is shown in Fig.4.15. The airfoil is rigid and it is mounted using a torsional spring and damper. Both sides of the foil are attached to the end plates and free to oscillates about its elastic axis which, is situated at $x/c = 0.186$ from the leading edge. The corresponding computational domain along with the mesh are shown in Fig.4.16 and Fig.4.17 respectively. The computational setup is made according to the experimental setup, i.e the foil dimensions and the setup of the test section. There are 53340 spectral elements in the domain ($9.23c \times 6.92c \times 0.25c$), with an element order (N) of 6 that leading to 1.15 million grid points in total. The final resolution is set to Δx^{+}_{min} = $\Delta z^{+}_{min} \approx 9$ and Δy^{+}_{min} ≈ 0.75 i.e. at the foil's wall. Inlet velocity is set to 6 m/s and $\nabla U \cdot x = 0$ is set at the outlet whereas a moving wall condition is set on the wing surface. A periodic boundary condition is imposed on the vertical side planes of the domain. The same convergence criteria and the other boundary conditions are used as the last test case. The Fig. 4.18 shows the deformed configuration of mesh at $4.7°$ angle of attack. It illustrates the ability of current mesh deformation scheme to deal with the mesh deformation in the cases of sharp trailing edge geometries such as foils. The figure shows that, most of the deformation takes place in between the boundary layer region of airfoil and boundary of the domain.

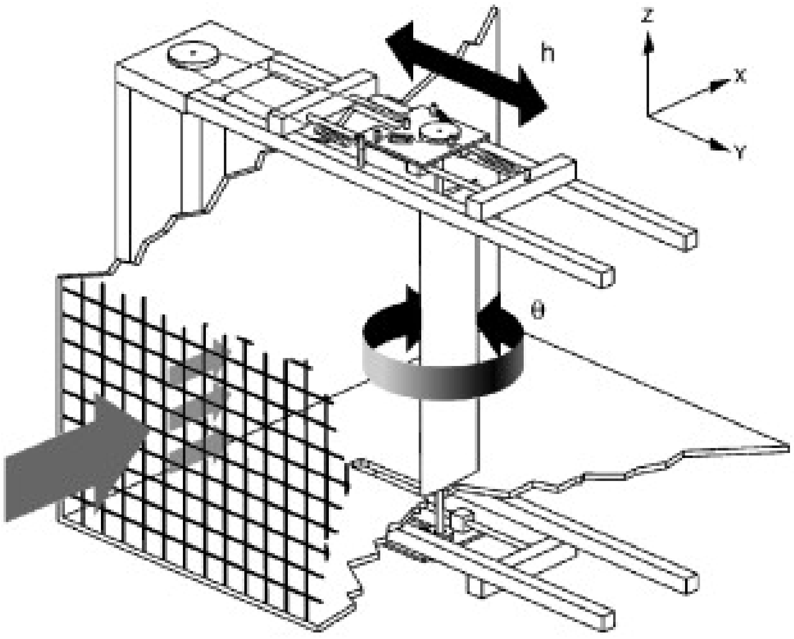

FIGURE 4.15: Experimental setup of NACA0012 airfoil (The picture is taken from Poirel et al., 2008)

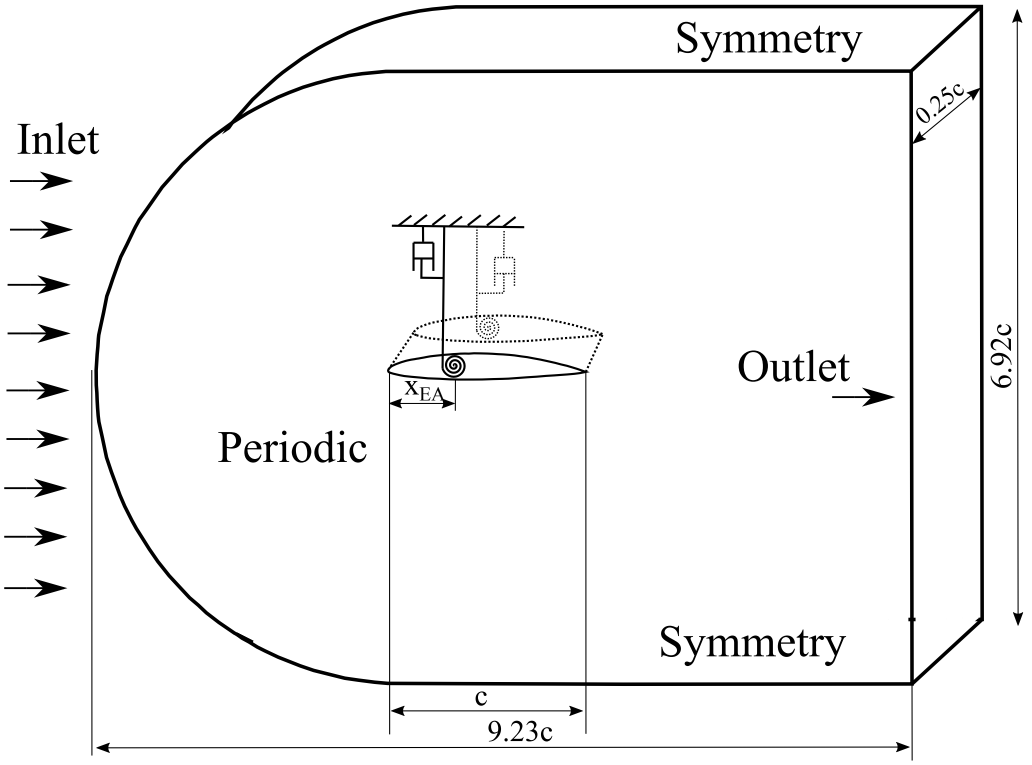

FIGURE 4.16: The computational domain of NACA0012 airfoil

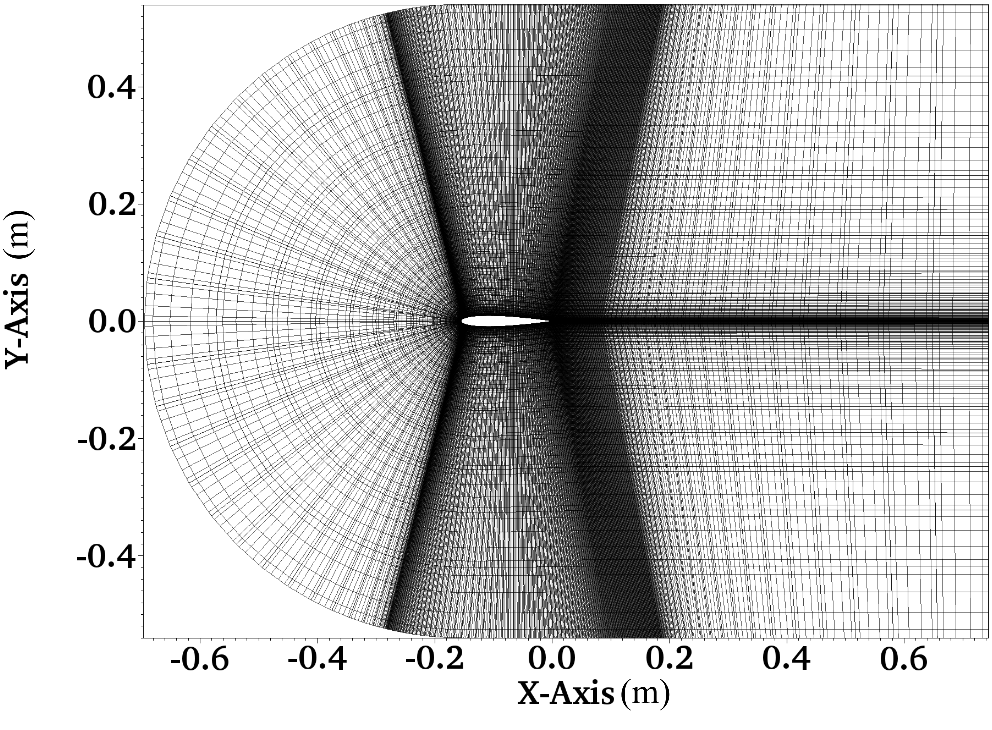

FIGURE 4.17: The spectral element mesh of NACA0012, N = 53340, O(6)

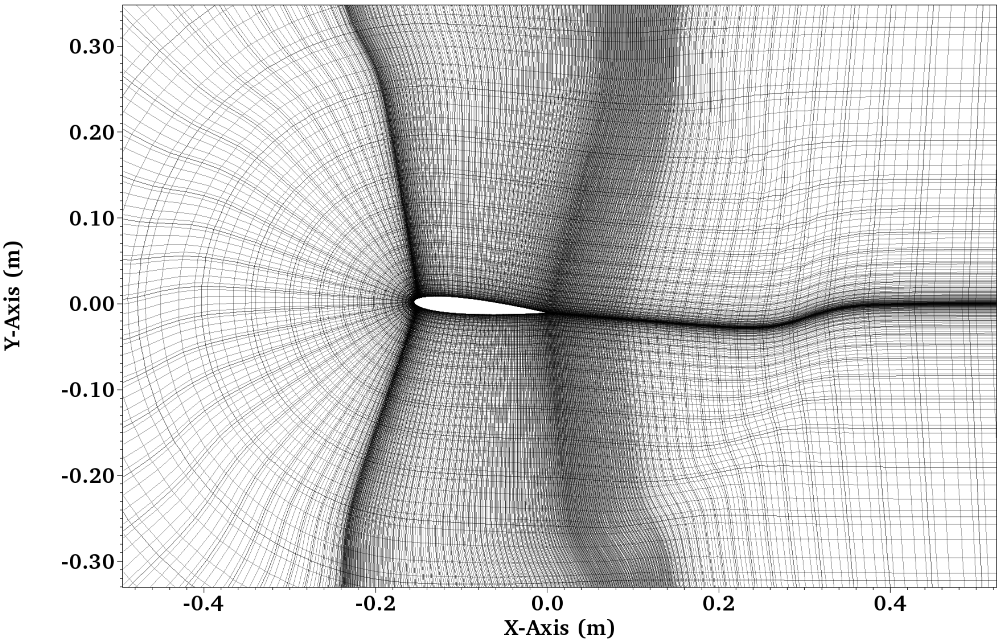

FIGURE 4.18: The deformed configuration of mesh at 4.7° angle of pitch

The system is reduced to 1-DOF to carry out the FSI studies. The plunging motion is not considered and the foil is free to rotate about its elastic axis. As a result, the general singular governing equations of motion (EOM) for pitching can be recalled from Eq.2.20 :

$$I_\alpha \ddot{\alpha} + D_\alpha \dot{\alpha} + K_\alpha \alpha = T_{EA} \tag{4.5}$$

Now let us re-write the above equation in the form of Eq.3.38, neglecting the added mass terms due the lower mass number (M = 0.018) :

$$\frac{\beta_0}{\Delta t} I_\alpha \tau + D_\alpha \dot{\alpha} + K_\alpha \alpha = T_{EA} \tag{4.6}$$

where T_{EA} is the moment exerted by the fluid on the foil about its elastic axis, with respect to the Z-axis. I_α is the moment of inertia of the foil, D_α is the damping coefficient and K_α is the stiffness of the rotational spring. τ is the correction factor, $\dot{\alpha}$ is the angular velocity of the body and α is the rotation angle about the elastic axis which is defined positive in the clockwise direction. The dimensional structural parameters of the NACA0012 airfoil are shown in Table 4.3.

TABLE 4.3: Aeroelastic parameters

I_α	0.00135	kgm^2
D_α	0.002	N m/rad
K_α	0.3	N m s
Chord (c)	0.156	m
Span (s)	0.61	m
x_{EA}	0.186c	-

Results and discussions

To check whether the laminar to turbulent transition is occurs, an instantaneous vorticity field is shown at $\alpha = -2°$ during pitching, see Fig.4.19. It confirms the presence laminar to turbulent transition at about 0.45c from the trailing edge. This transition to turbulence is caused by a LSB that will be confirmed later in the analysis.

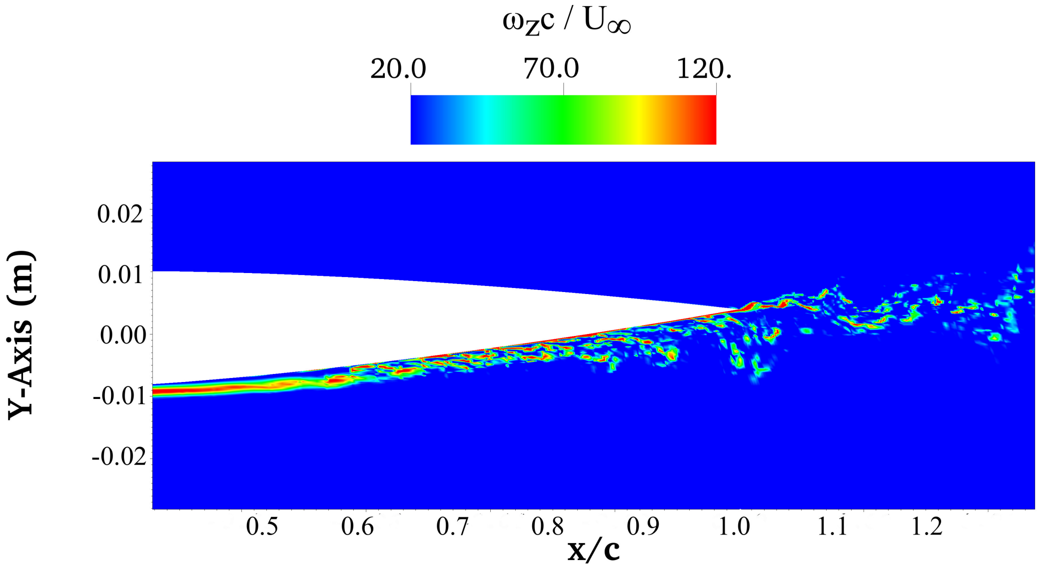

FIGURE 4.19: Instantaneous Vorticity field of the naca0012 at $\alpha = -2°$ downward pitching, Re = 64,000.

Fig. 4.20 shows the comparison between pitch amplitude response of the foil in present DNS and the LES of Lapointe and Dumas, 2011. The present DNS numerically converges faster than the LES, however it leads to the same solution for the pitch amplitude and period. It can be observed that the foil responds to a single period i.e. the natural frequency of the spring. This behaviour corresponds to the typical case of self sustained oscillations, characterized by a large LSB region together with a highly flexible system. Although turbulent flow occurs, it does not

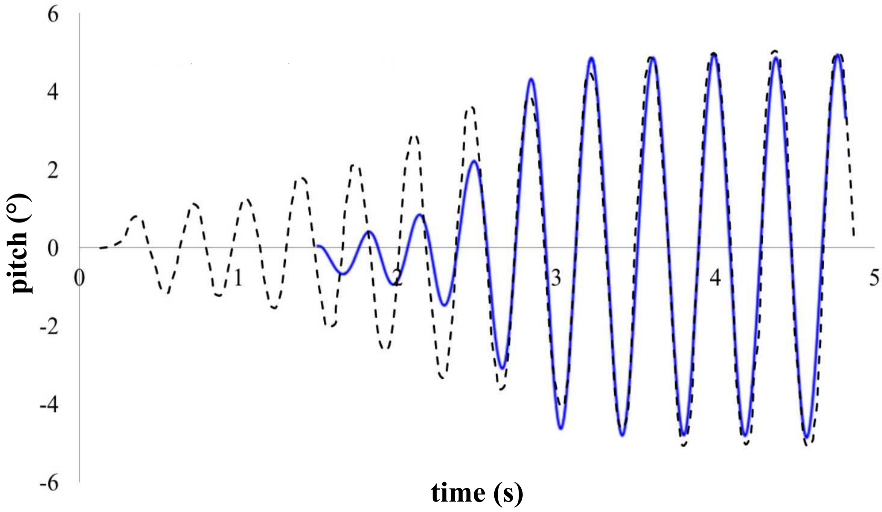

FIGURE 4.20: Comparison of pitch response time history at Re = 64,0000. The blue line represents the pitch amplitude from Nek5000 and dotted line represents the pitch amplitude from Lapointe and Dumas, 2011

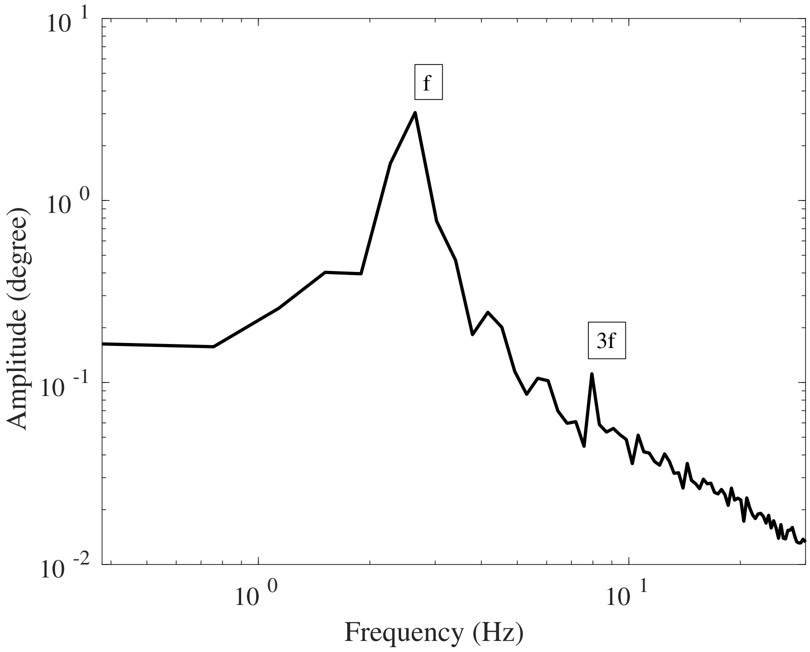

FIGURE 4.21: Spectral analysis of the pitch response at Re = 64,0000, current DNS.

disturb the structural response, and DNS is not necessary to capture this physic. The LSB shedding appears to be forced by the foil pitch response. Fig.4.21 shows the spectral analysis of the LCO regime. A subharmonic at $3f$ is also observed from the spectra of LCO. This behaviour significantly differs from our case, which will be characterized by a higher pitching frequency and lower amplitude of oscillation. The transition will be more localized and sharper, and not directly governed by the pitch response; hence a more complex fluid structure interaction phenomenon is expected.

The Table 4.4 shows the quantitative comparison of pitch amplitude and frequency of oscillation. A good comparison is observed with the literature, even with the URANS simulation of Poirel et al., 2011.

TABLE 4.4: Comparison of results for Self-Sustained Oscillations at Re = 64,000

Reference	Max pitch (deg)	Frequency (Hz)
Present DNS	4.8	2.61
Exp. Poirel et al., 2008	4.0	2.70
LES Lapointe and Dumas, 2011	5.3	2.57
URANS Poirel et al., 2011	4.7	2.90

To investigate the transition location, Fig. 4.22 shows the comparison of coefficient of friction during one period of pitch (pitching up from $0°$ to $4.78°$ and then down to $0°$). The URANS calculations of Poirel et al., 2011 are also shown for comparison. When the wing moves from $0°$ to maximum pitch angle, the laminar separation point is delayed on the upper wing surface as compared to static case. As laminar separation is due to adverse pressure gradient, URANS and DNS compare well at each instance (see the marks that highlight the zero friction). The dead region of the LSB also compare well. However, the URANS method does not predict the flow acceleration in the core of the LSB, corresponding to the stagnation of negative friction coefficient, and the influence of turbulent flow observed with the DNS.

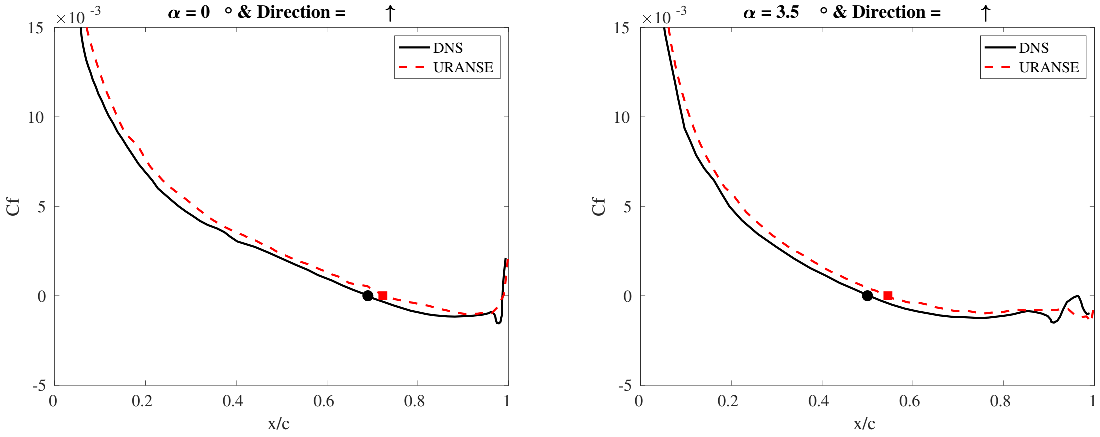

(A) 0°, Upward pitching

(B) 3.5°, Upward pitching

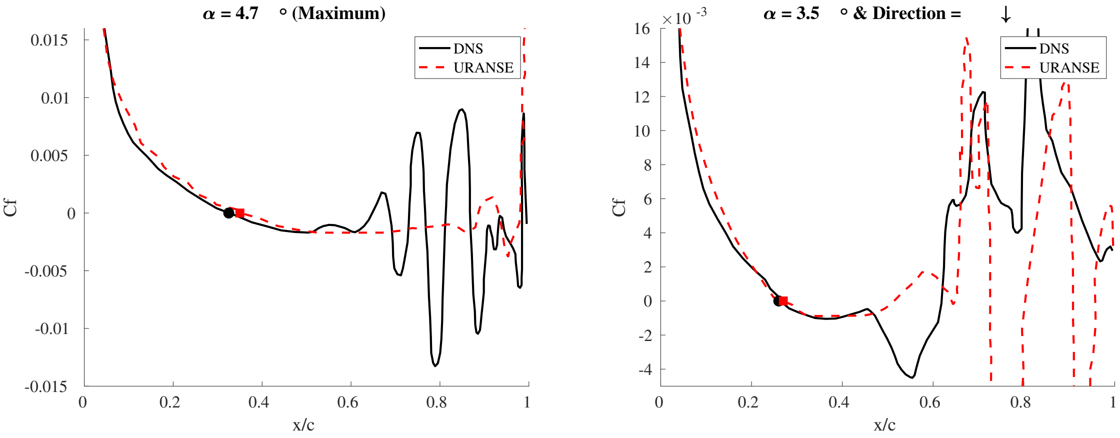

(C) 4.7°, Maximum angle of pitch

(D) 3.5°, Downward pitching

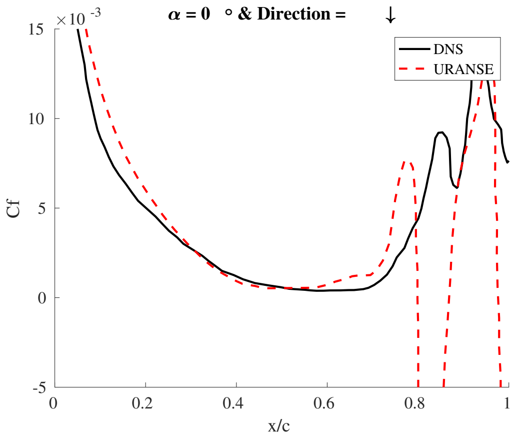

(E) 0°, Downward pitching

FIGURE 4.22: Unsteady friction coefficient at different instants of pitch angle during upward and downward pitching cycle, on the upper surface of the foil at Re = 64,000.(Circle and Square marks represents the separation points in DNS and URANSE respectively)

4.2 Conclusion

In this chapter, we have validated our mesh deformation schemes and FSI coupling methods. It seems the choice we have made from previous Chapter is satisfactory. Some of the key findings are :

- Lock in and Unlock in regions are observed and validated in Forced and VIV cylinder cases along with the validation of mesh deformation schemes.
- Explicit and Implicit couplings can be used for FSI problems where added mass effect is dominant. However, the accuracy of explicit method is lower with the existing method but it can be improved by sub-iterations, which increases the computational effort.
- Implicit method is again validated with in a non-linear coupling case (i.e. transitional flow around an airfoil) which is closer to our final objective in terms of flow regime and structural behavior.

Chapter 5

Results of STATIC & FLEXIBLE NACA6612 hydrofoil at Re = 450,000

Summary

This chapter consists of 3 subsections. In the first section, the non-dimensional numbers and parameters are introduced to distinguish the flexible hydrofoil cases. The following section shows some validation studies between restricted and full size DNS domain in static and flexible NACA6612 at $\alpha = 4^\circ$ and Re = 450,000. In the last section, the results of different flexible NACA6612 hydrofoils are discussed along with static results. These results comprises of a boundary layer flow analysis, which shows the main characteristics of the boundary layer flow from a time averaged flow and instantaneous. The transition and behaviour of coherent hair pin structures at different conditions are also observed. Then, wall pressure analysis is measured to study the effects of foils acceleration on the pressure coefficient and TS waves. A spectral analysis of wall pressure signals is also carried to investigate the influence of vibration on the transition. Later, the FSI results is consisting of the response of hydrofoil in terms of pitch angle, pitch velocity and torque is shown. Finally, a spectral analysis of the pitch velocity is carried out to understand the possible coupling effects between the laminar to turbulent transition and hydrofoil frequency.

5.1 Non dimensional parameters used for transition induced vibration

In this section we establish non-dimensional parameters in order to be able to characterise the transition induced vibration of free and forced pitching hydrofoil. First, a similarity parameter based on the chord length (c), upstream velocity (u_∞) and the pitching velocity ($\dot{\alpha}$) is introduced to form a non-dimensional pitching velocity $\dot{\alpha}^* = \dot{\alpha}c/2u_\infty$, where $c = 0.150m$, $u_\infty = 3m/s$. And non-dimensional pitching amplitude can be obtained from pitch amplitude (α) and momentum thickness (θ_{sep}), i.e, $A_\theta = \alpha c/2\theta_{sep}$. The half of the chord length (c/2) is chosen because the elastic axis (EA) is located almost half of the chord (i.e. x/c=0.47). The value of momentum thickness (θ_{sep}) at laminar separation was calculated from the static case, that is θ_{sep} = $0.00012m$. This quantity have also been used in the past to form a famous Strouhal number of LSB vortex shedding(Pauley et al., 1990), where S_t= $f\theta_{sep}/u_{sep}$, suggesting the dynamic characteristics of the LSB is linked to the boundary layer quantities at laminar separation..

In addition to a rigid hydrofoil (named STATIC case), five different types of flexible hydrofoil cases studied in this PhD work are defined as follow:

- FORCED A and FORCED B: here, the pitching motion is imposed, and hence the non-dimensional parameters $\dot{\alpha}^*_{(max)}$ and $A_{\theta(max)}$, which are the maximum values of non dimensional pitching velocity and amplitudes, respectively, obtained from the forced motion i.e.: :

$$\alpha(t) = \alpha_{max} sin(2\Pi f_N t) \tag{5.1}$$

- FSI A, FSI B and FSI C: here, the hydrofoil is free to oscillate, allowing fluid-structure interaction. $\dot{\alpha}^*_{(max)}$ and $A_{\theta(max)}$ are initially estimated by setting appropriate structural parameters with the help of forced oscillation cases, and the corresponding values are subsequently calculated in post-processing.

FORCED A reproduces the experimental parameters (torsional frequency and corresponding spectral amplitude) of Ducoin et al., 2012 (see also mode 2 in Fig. 5). In FORCED B, the amplitude is greatly increased, in order to obtain a large pitching effect. Both cases use $F = 0.5$, where F is the frequency ratio of the natural frequency of the foil (f_N) to the TS wave frequency (f_{TS}), the latter is taken from the rigid case where it was shown to be 335Hz (Ducoin and Astolfi, 2019). TS waves are used to characterise the transition dynamic because it is a 2D and purely periodic process at the first stage of transition.

FSI A case corresponds to the structural properties of the hydrofoil investigated experimentally in Ducoin et al., 2012. In the present case, the hydrofoil is then pitching with a given non-dimensional angular velocity $\dot{\alpha}^*_{(max)} = 0.00056$ (corresponding to a maximum pitching velocity ($\dot{\alpha}_{max}$) of $0.57°/s$) and a frequency ratio of $F = 0.5$. In FSI B, the amplitude is increased by approximately one order of magnitude (corresponding to $\dot{\alpha}^*_{(max)} = 0.00228$ or $\dot{\alpha}_{max}$ = $2.52°/s$) while the natural frequency is kept the same, i.e. $F = 0.5$. Finally, in FSI C, $\dot{\alpha}^*_{(max)}$ and $A_{\theta(max)}$ are in the same order of magnitude as FSI B, but the frequency ratio is set close to 1 ($F = 1.1$) to enhance the fluid-structure interactions. Table 5.1 summarises the non-dimensional parameters and natural frequency for each case, keeping in mind that the TS wave frequency is kept constant i.e. f_{TS} = $335Hz$.

TABLE 5.1: Non dimensional and dimensional parameters in all flexible cases

Cases	$A_{\theta(max)}$	$\dot{\alpha}^*_{(max)}$	F	$f_N(Hz)$
FORCED A	0.0100	0.00020	0.5	170
FSI A	0.0301	0.00056	0.5	170
FSI B	0.2125	0.00228	0.5	170
FSI C	0.1824	0.00169	1.1	368
FORCED B	0.3272	0.00750	0.5	170

Table 5.2 corresponds to the dimensional parameters of the structure in each FSI cases.

TABLE 5.2: Dimensional quantities associated to each FSI cases.

Cases	$I_\alpha + I_a$ (kgm^2)	K_α (Nm)	$D_\alpha(kgm^2/s)$	F
FSI A	0.00416	4915.1	0.1742	0.5
FSI B	0.00059	702.15	0.0236	0.5
FSI C	0.00012	702.15	0.0236	1.1

Here I_α is the inertia of the structure, I_a is the added mass effect on inertia from the Full DNS domain, K_α is the torsional stiffness and D_α is the damping coefficient in rotational motion.

All the results in this chapter were calculated over 25 periods of TS waves, as measured in the static case at Re = 450, 000. The time is non-dimensionalised by t/t_{TS}, where t_{TS} is the period of TS waves in the static case. The linear velocity component of the pitching hydrofoil was obtained at a distance of 0.22c from the elastic axis towards the leading edge.

5.2 Computation cost

Table 5.3 shows the comparison of time required for one time step between STATIC, FORCED and FSI cases. In order to compare, all the simulations are performed at 4096 processor with same accuracy for pressure and velocity. Moreover, a constant time step is chosen for a fair comparison. It is observed that the time required to move the mesh and solve the system with new boundary conditions alone in forced case is almost 19.5% higher than the time required to solve the same system in static condition. Similarly, the time required to solve the structural part in FSI case takes 31% longer than the static case including the mesh deformation as well. If we just consider the time required for solving the structural equations, it is about 11.5% higher than the forced case.

TABLE 5.3: Computational time for one time step with 4096 processors.

Cases	Time (s)	Difference (%)
STATIC	0.8279	x
FORCED	1.0293	1.19.x
FSI	1.1997	1.31x

The computation cost for 25 periods of LSB shedding/ TS waves is about 200,000 hours in STATIC case and 240 000, 272 000 hours for FORCED and FSI cases respectively. However, the total computation time is even higher because the physical convergence of fluid flow during FSI required almost three times of the above said STATIC computation time. In effect, the total computation time for one FSI simulation is about 0.9 million hours on HPE SGI 8600 machine. In this PhD, I have used about 9 million hours in total for all the set of computations including validation cases. Out of that, 5 million hours are used on Turing, IBM Blue Gene/Q from IDRIS and 4 million hours are used on the latest Jean Zay, HPE SGI 8600 machine from IDRIS as well.

5.3 Validation studies

Simulation at Reynolds = 450,000 using DNS is quite expensive, the choice is to reduce the number of elements by keeping a full DNS resolution. Hence, a near wall DNS domain is used in order to lower the computational effort. An innovative technique of changing the fluid domain to the near wall and imposing steady velocity boundary conditions from the result of the mean flow of a full DNS domain (the experimental domain dimensions) is used. As it is a strong assumption this may induce some modifications to (i) the boundary layer flow in the unsteady regions (i.e. downstream the transition region) and (ii) the coupled simulation, where the hydrofoil can have a modified structural behaviour due to the confinement (i.e. modification of the added mass). Different measures are taken into account to avoid possible consequences of this near wall DNS domain during STATIC and FSI simulations. However validations are important to make sure the corrections are defined properly. Several comparisons are presented to validate the boundary conditions of the present DNS model. First, we validate the current restricted DNS domain that uses full DNS flow velocity profiles at its boundaries, after what the results are compared with the full DNS domain by using the experimental test section dimensions, without and with free pitch motion. Then, the boundary layer characteristics of the near wall domain is compared with Laser Doppler Velocimetry (LDV) measurements taken from Ducoin et al., 2012. It has to be noted that the proposed near wall DNS domain has already been validated against experimental measurements with a rigid (STATIC) configuration prior to this work. (Ducoin and Astolfi, 2019).

5.3.1 Validation of flow over static NACA66 at 4° and Re = 450, 000, Near Wall v/s Full DNS domain

Problem setup

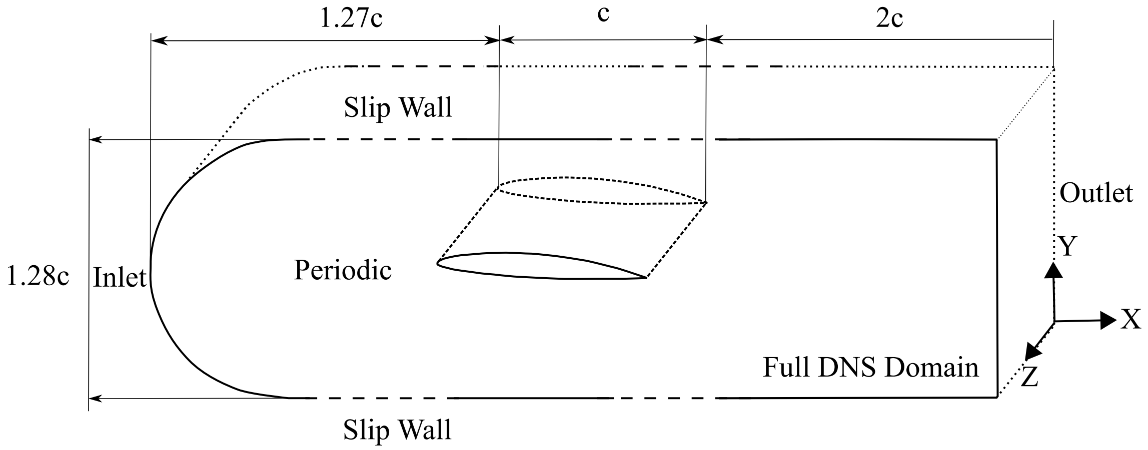

FIGURE 5.1: The full DNS computational domain of the NACA66 hydrofoil (As per the experimental setup)

The computational domain for the full DNS and near wall DNS static cases are shown in Fig.5.1 and Fig.5.2. Periodic boundary conditions are imposed on the vertical side planes of the both domains and $\nabla U.x = 0$ was set at the outlet. Depending if the hydrofoil is moving or not, either a no-slip condition or moving wall boundary condition is imposed on the wing surface and symmetry boundary condition is imposed on the top and bottom wall of the full DNS domain to avoid extra computational effort at the boundaries. Whereas the near wall DNS domain has steady velocity profiles at inlet and top and bottom walls. The steady velocity profile of the near wall domain boundaries in X-direction is shown in Fig.5.3. The full DNS domain is made according to the dimensions of experimental setup where about 10% of confinement effect is still present (Ducoin et al., 2012). The span of both domains is reduced to 0.05c. It is observed that the transverse wavelength of hair pin structures linearly varies with respect to the boundary layer thickness which is proportional to $1/\sqrt{Re}$ (Ducoin and Astolfi, 2019). So at the current Reynolds number

(Re = 450, 000) the value is close to $0.04c$. Thus the choice of span length is made slightly higher than $0.04c$, i.e $0.05c$.

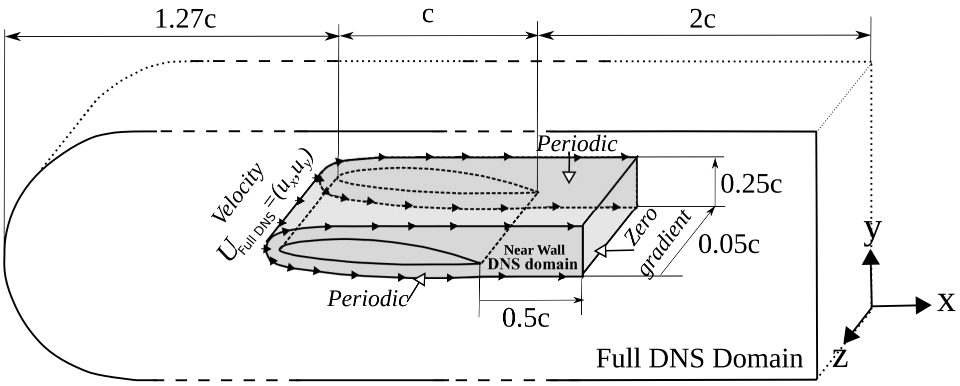

FIGURE 5.2: The near wall DNS computational domain of the NACA66 hydrofoil

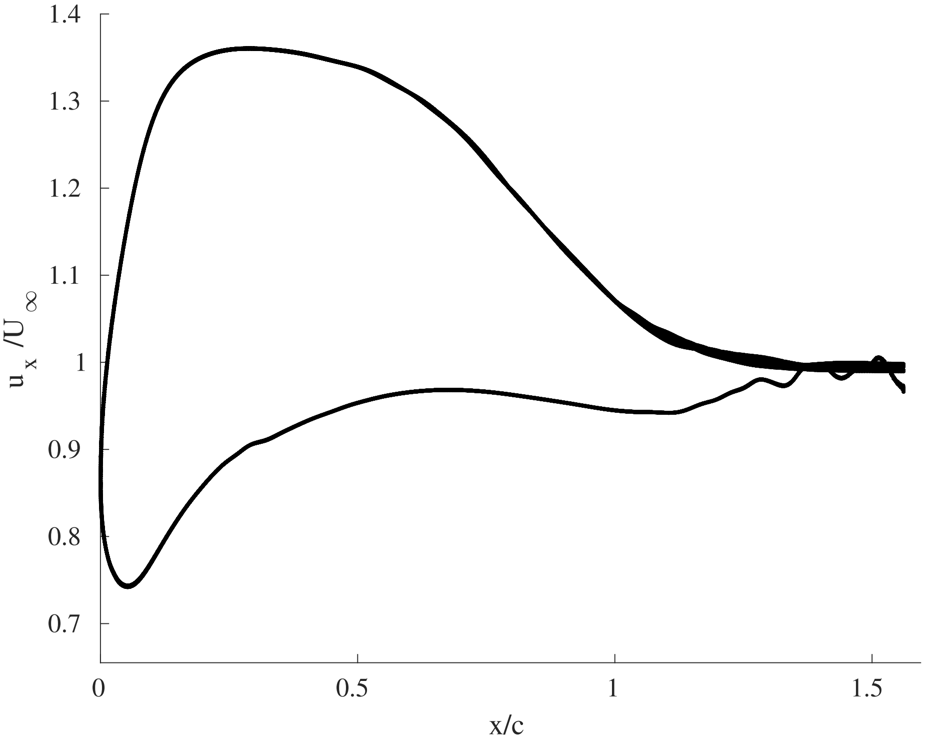

FIGURE 5.3: Steady inlet velocity profile for the near wall DNS domain, Re = 450,000, U_∞ = 3m/s

The spectral mesh for both Full and near wall DNS domains are shown in Fig.5.4 and Fig.5.5. In both cases, the mesh close to the wall is refined to obtain a required y+ value, whereas it is almost constant in chord-wise(x) and span-wise(z) directions. As a result, 333,480 spectral elements are generated in the full DNS domain whereas 188,480 spectral elements are generated in the near wall DNS domain. Due to the higher computational expense, a spectral element order of O(10) is used in the full DNS domain simulations whereas O(12) is used in the near wall DNS domain. An 11^{th} order polynomial approximation is used for velocity whereas a 10^{th} order approximation for pressure in both cases. The convective terms are advanced in time using an extrapolation of O(3), whereas the viscous terms use a backward differentiation of O(3).

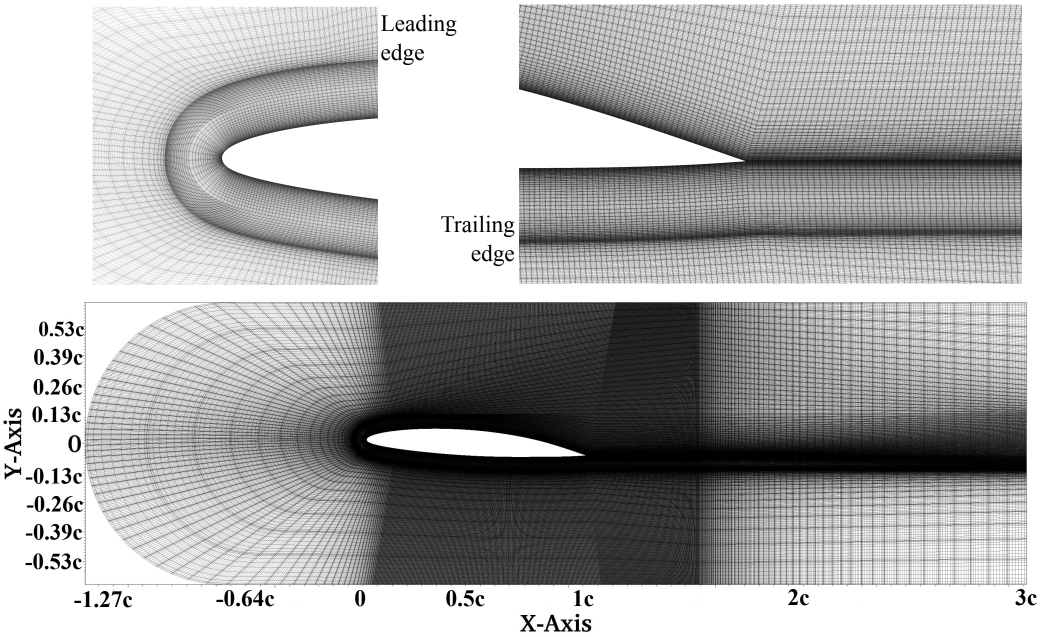

FIGURE 5.4: Spectral element mesh of the full DNS domain of the NACA66 hydrofoil, N = 333,480 and O (10)

The Fig.5.6 shows the final mesh resolution along the chord for the two cases at the wall in tangential, normal and span-wise directions. It is taken from the friction velocity, which is time and span-wise averaged over 25 period of TS waves. Since the spectral elements are non-uniformly distributed, Δx^+ and Δz^+ give maximum and minimum values. The final resolution of full DNS domain with O(10) leads to $\Delta x^+_{min} = \Delta z^+_{min} \approx 7$, $\Delta x^+_{max} = \Delta z^+_{max} \approx 15$ and $\Delta y^+ = 0.3$ corresponding to 334 million grid points at Re = 450, 000. Similarly, the final resolution of the near wall DNS domain with O(12) leads to $\Delta x^+_{min} = \Delta z^+_{min} \approx 5$, $\Delta x^+_{max} = \Delta z^+_{max} \approx 8$ and $\Delta y^+ = 0.2$ corresponding to 326 million grid points. The considered mesh resolution for the full DNS domain is seemed to be sufficient to capture the transition mechanism even though the mesh resolution is lower. A similar mesh resolution is used in Hosseini et al., 2016 and Vinuesa et al., 2018 at moderate range of Reynolds numbers (100,000 to 1,000,000) using Nek5000 on airfoils.

An isotropic von Kármán turbulence model(KARMAN, 1937) which is based on the energy spectra of the perturbation is used to disturb the flow at the inlet of the

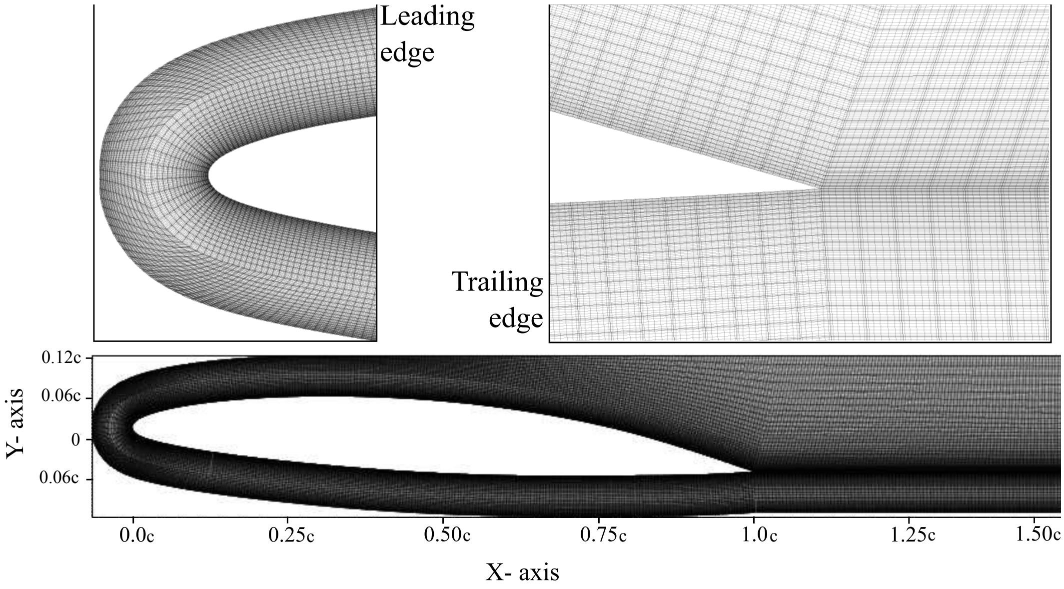

FIGURE 5.5: Spectral element mesh of the near wall DNS domain of the NACA66 hydrofoil, N = 188,480 and O (12)

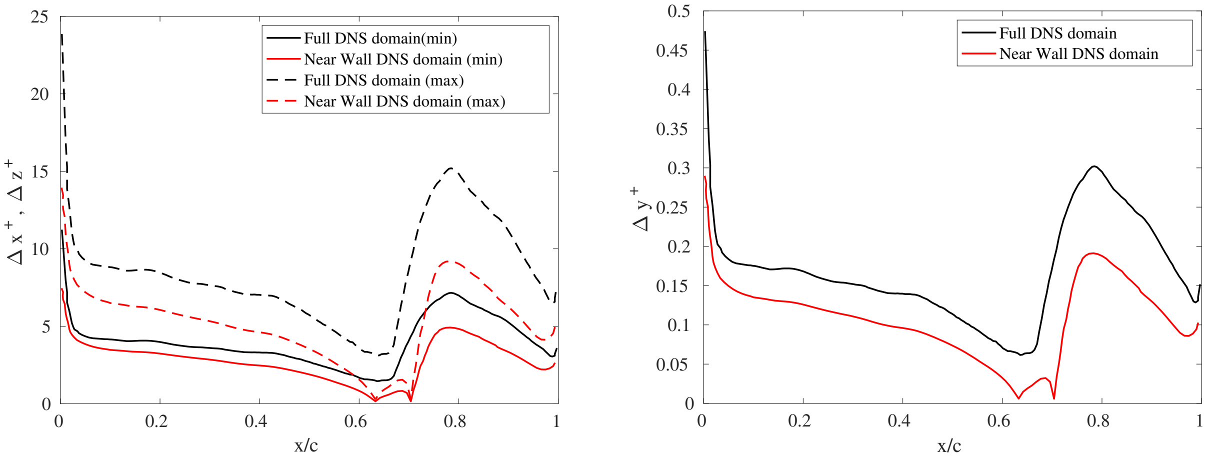

(A) Streamwise (Δ_x^+) and spanwise (Δ_z^+) resolutions

(B) Wall normal resolution (Δ_y^+)

FIGURE 5.6: Mesh resolution at the hydrofoil surface for both near wall and full DNS domains.

near wall DNS domain. It is based on the generation of synthetic isotropic turbulence. The model presented here is taken from the work of Davidson, 2015 and has been already implemented and tested in Nek5000, within our group by Sharma and Ducoin, 2018. The energy spectrum is numerically set by random number generating algorithms to generate random Fourier modes. The mathematical details and derivations can be found in Appendix B. The synthetic turbulence model is applied only at a portion of the inlet as shown in Fig.5.7. However, it covers the whole boundary layer of the hydrofoil. The disturbances are convected with the free-stream flow. The intensity of the inlet turbulence model is set to $\approx 2\%$ to match with that of the experimental facility (Ducoin et al., 2012). In the case of full DNS domain, no inlet turbulence is imposed since the mesh close to the inlet is very sparse and numerical divergence was observed, caused by the propagation of numerical instabilities. In this case, the transition is triggered by the mesh itself, which is considered to have only a secondary effect on the validation process.

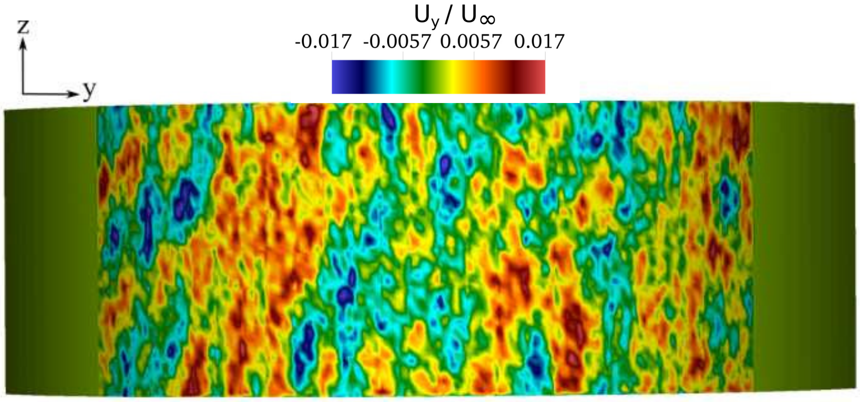

FIGURE 5.7: Velocity contour of isotropic inlet turbulence at a maximum magnitude of 2% of inlet velocity, at Re = 450,000 and $U_\infty = 3m/s$

Results and Discussion

Mean flow comparison at Re = 450,000

To check the validity of the DNS velocity boundary conditions of the near wall DNS domain, the mean flow obtained from both domains are compared in this section. The Fig.5.8 shows an overall good agreement between the averaged velocity fields of both cases. The stagnation point is accurately reproduced by the near wall DNS at $x/c = 0.0055$. Moreover, the velocity gradient is correctly reproduced until the transition region, in comparison to the full DNS domain. Local velocity profiles close to the hydrofoil's upper surface along the chord are shown in Fig.5.9. The comparison between the velocity profiles are in good agreement even though the velocity of near wall domain is slightly forced due to the added confinement effect. As a result, the boundary layer external velocity is approx 7% higher for the near wall domain as compared to the full DNS domain. This numerical error is corrected in the computation of coefficient of pressure which will be discussed later.

A comparison of span-wise and time averaged friction coefficients between the near wall and full DNS cases along with Xfoil results are shown in Fig.5.10. Two different configurations are performed in Xfoil with N_{crit} = 14 at Re = 450,000. At

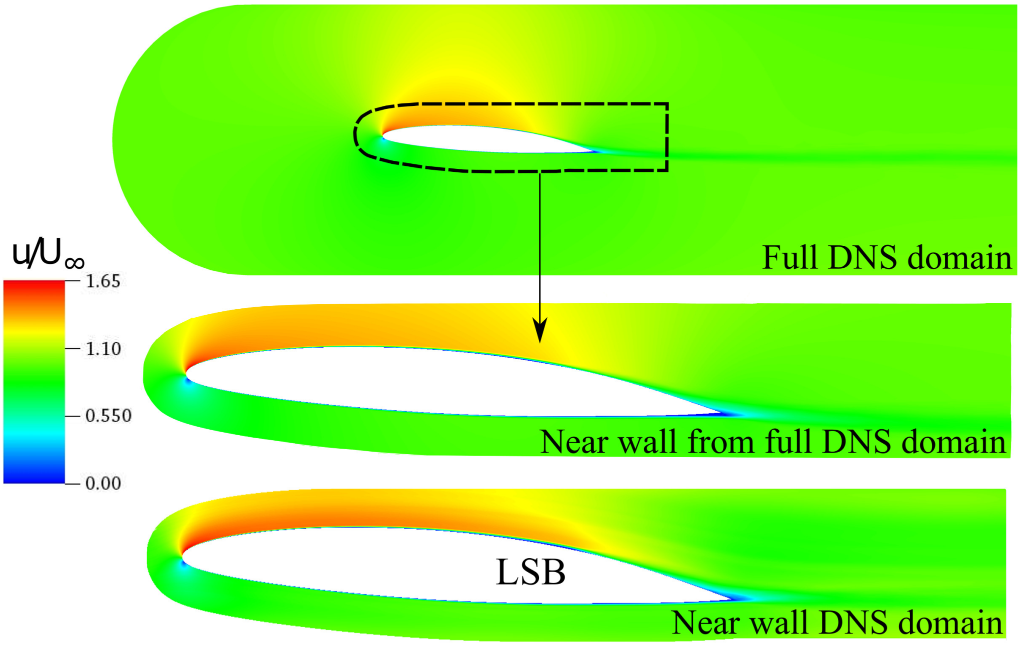

FIGURE 5.8: Comparison of near wall and full DNS domains velocity contours, Re = 450,000

$\alpha = 4^\circ$ and $Re = 450,000$, the LSB is small and is hence quite sensitive to small variation in adverse pressure gradient at this configuration. First one is lead with $\alpha = 3^\circ$ and latter is with 4°. In the near wall DNS case, the laminar separation and reattachment of the flow is located at $x/c = 0.62$ and $x/c = 0.71$ respectively. Thus, the transition is induced by the laminar separation bubble. At an angle of attack of 3° the LSB appears towards the end of trailing edge. At 4° the LSB is not formed and the transition is advanced towards the leading edge around $x/c = 0.05$ where friction is lower in the Xfoil. A slight change in the angle of attack has made a significant difference on the LSB and transition location. Similarly, in the case of full DNS case, the LSB is not observed. The main difference between the near wall DNS and full DNS calculations is the transition point, which is advanced by x/c = 0.04 due to the small modification of the adverse pressure gradient and hence the removal of LSB. This modification is however considered as second order and does not affect periodic fluctuations in the wall pressure due to the TS waves. However, a short term appearance and disappearance of LSB is suspected in the full DNS case. The presence of LSB in the near wall domain might be due to the slightly forced velocity flow over the foil that affect the pressure gradient over the foil.

A comparison of time averaged pressure coefficients is shown in the Fig.5.11. Overall a good agreement is observed between the cases even though some slight local variations are observed on the suction side. The lower pressure peak at the

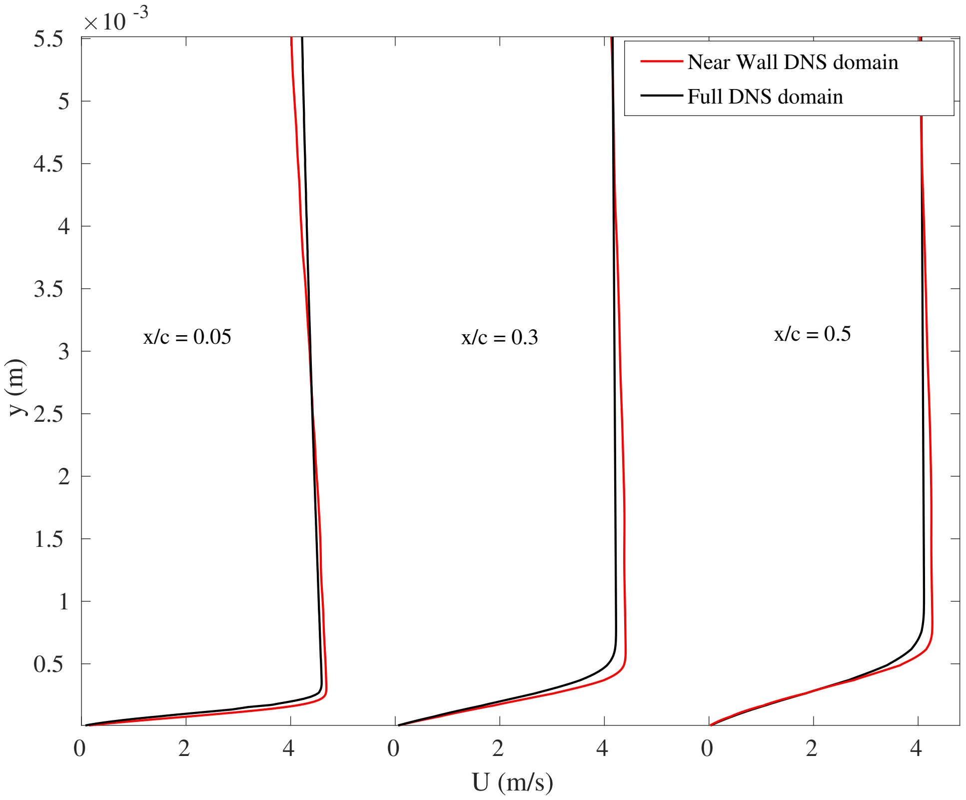

FIGURE 5.9: Comparison of full DNS and near wall DNS domains velocity profiles for three different locations, Re = 450,000

leading edge of suction side ($0 < x/c < 0.05$) side is different in all the cases. The Xfoil shows the lowest peak because there is no confinement, which is followed by the full DNS domain and then near wall DNS domain. However, the near wall domain quickly changes its pressure gradient and matches with the full DNS domain as it moves toward the leading edge ($0.05 < x/c < 0.2$). Then both near wall and full DNS cases are well matched up to the transition region ($0.2 < x/c < 0.6$). A slight difference is observed between the two domains in the transition region which results in the presence/ absence of LSB.

Wall pressure and velocity analysis at Re = 450,000

In this section wall pressure results are compared between both domains along with experimental results obtained from Ducoin et al., 2012 at Re = 450,000.In Fig.5.12, we compare the experimentally measured local wall pressure coefficients to those obtained with DNS at Re = 450,000, U_∞ = 3 m/s for $x/c = 0.7, x/c = 0.8$ and $x/c = 0.9$. All the results are shown for 10 period of TS waves and adjusted temporally to be synchronised with each other. Overall, a good agreement is observed

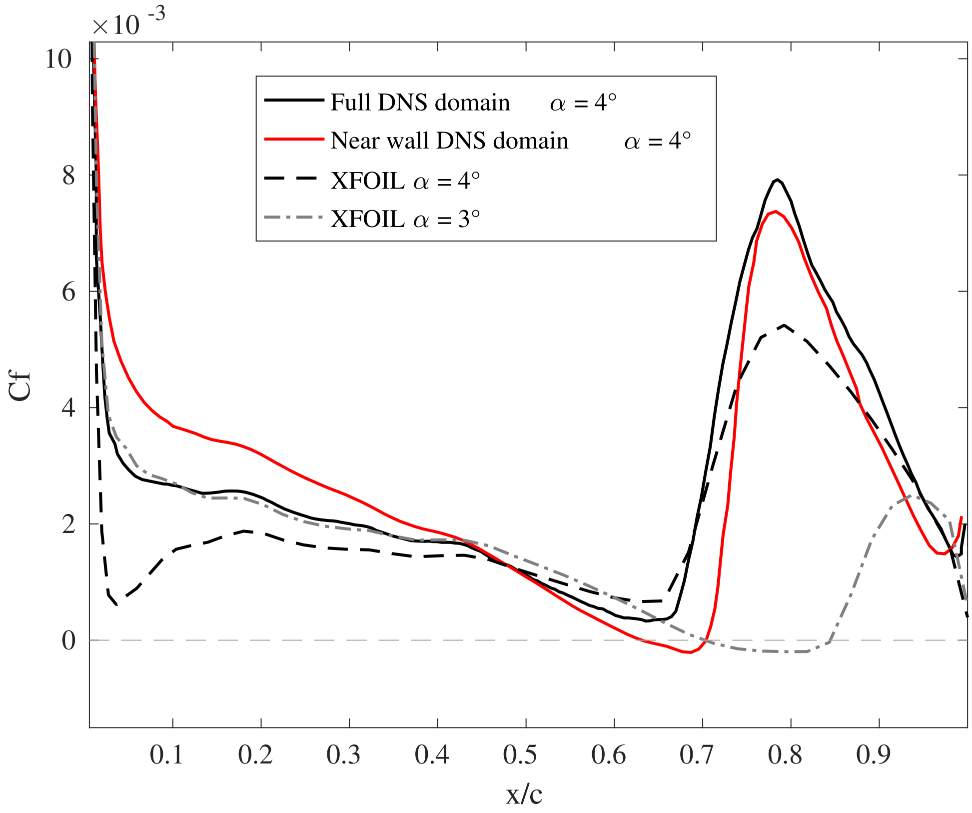

FIGURE 5.10: Comparison of friction coefficient at Re = 450,000 along with Xfoil with $N_{crit} = 14$. The N_{crit} is a value used to set the free stream turbulence level in the Xfoil. Higher N_{crit} (close to 20) represents lower ($\approx 0.05\%$) free stream turbulence intensity and N_{crit} = 1 means too much disturbance in the flow.

between the near wall DNS and full DNS along with the measured values in terms of temporal behaviour and amplitudes.

In the transition region at x/c = 0.7(Fig.5.12(a)) the flow is highlighted by the development of coherent structures and of TS waves that progressively form 3D coherent structures between $0.7 < x/c < 0.8$. The TS waves causes strong periodic pressure fluctuations intermittently in experimental and both DNS computations. The full DNS case predicts slightly higher amplitude of pressure fluctuations, however the same intermittent behaviour is obtained. As the flow convects further, at x/c = 0.8 (Fig.5.12(b)) the signal consist of some random nature and smaller amplitude fluctuations, together with a periodicity caused by the development of hairpin structures. At x/c = 0.9 (Fig.5.12(c)) which is close to the trailing edge, the signal is in turbulent region which shows fully random fluctuations and lower amplitudes of fluctuations.

A spectral analysis is performed to find the dominant frequency components in the pressure fluctuations, thereby identifying the TS wave/ LSB shedding dynamics.

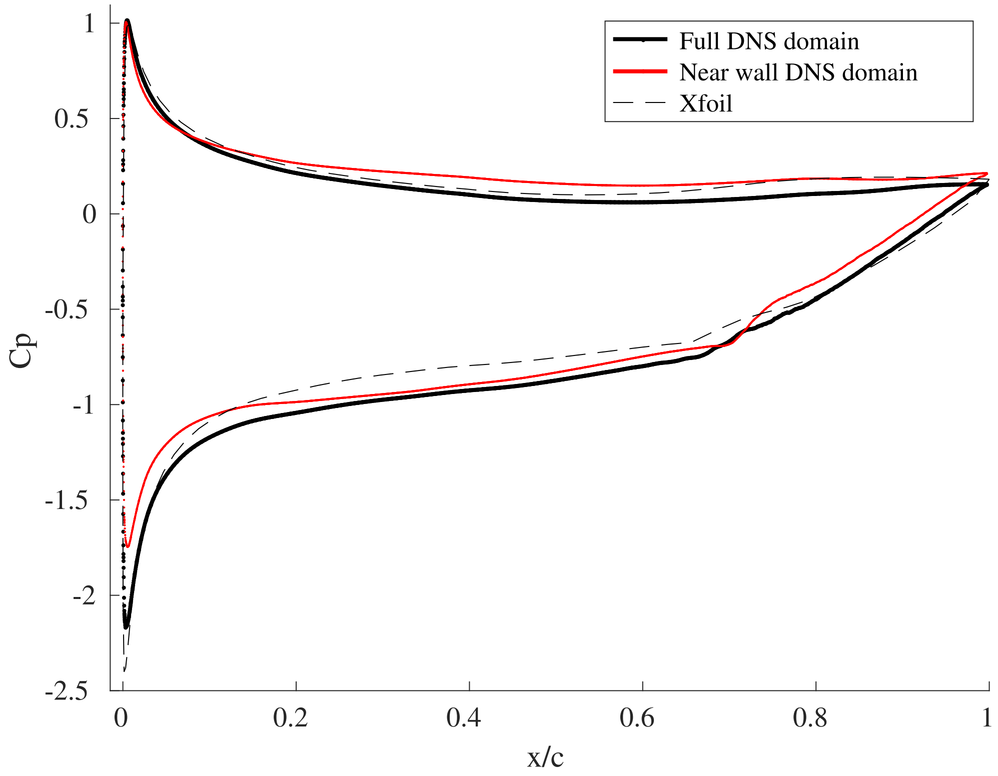

FIGURE 5.11: Comparison of time averaged coefficient of pressure at Re = 450,00 along with Xfoil where N_{crit} = 14

The results are shown in Fig.5.13 and they are showing good agreement with each other.

At x/c = 0.7, it shows the main frequency peak of TS wave/ LSB vortex shedding. A rapid fading is observed at higher frequencies in all the cases. As it moves forward in chord wise direction, a continuous reduction in the amplitude of frequency is observed; however the main peak is still noticed at $x/c = 0.8$ and $x/c = 0.9$. Moreover, the amplitude of full DNS domain is slightly lower than that of near wall DNS and experimental results. It could be due to the lower mesh resolution of full DNS domain at the turbulent region (O(10)) compared to that of near wall DNS domain (O(12)), and the absence of inlet isotropic turbulence.

An exhaustive data of wall pressure coefficients over 25 periods of TS waves/ LSB shedding of both near wall and full DNS along the chord is shown in Fig.5.14. The corresponding spectral analysis of the wall pressure coefficients along the chord is also shown in Fig.5.15. The X-axis of both figures are non dimensionalized using the experimentally observed shedding period ($T_{shed(Exp)} = 0.0033s$) and frequency ($f_{shed(Exp)} = 300Hz$) respectively. Both DNS domains give very similar

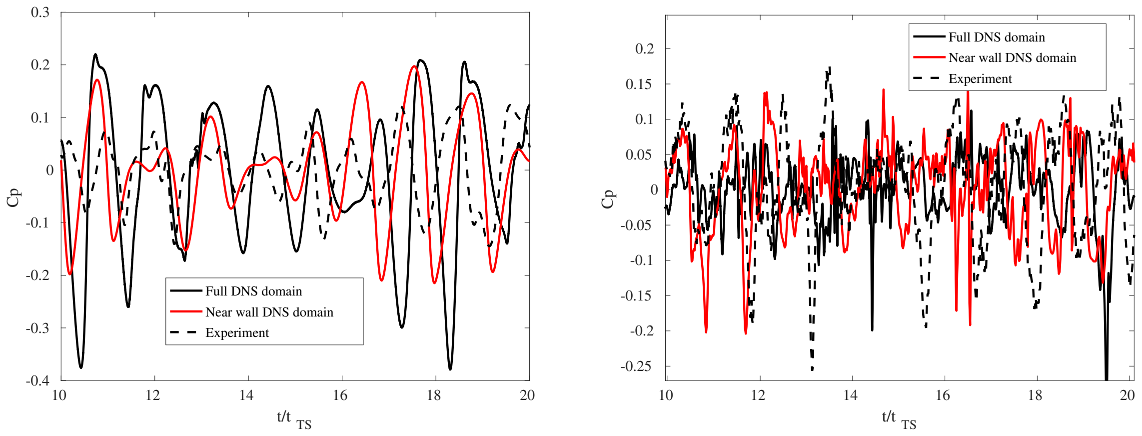

(A) x/c = 0.7 (B) x/c = 0.8

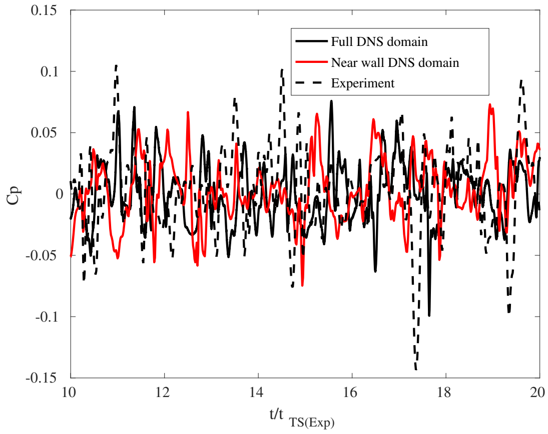

(C) x/c = 0.9

FIGURE 5.12: Comparison of computed and measured wall pressure coefficient, Re = 450, 000, U_∞ = 3 m/s

results especially at the region where strong periodic pressure fluctuations are observed ($0.6 < x/c < 0.7$). However, a slight difference can be observed from ($0.7 < x/c < 0.8$) due to the absence of LSB in full DNS domain; however, intermittent periodic fluctuations are observed in the pressure fluctuations of full DNS domain which is suspected as intermittent presence of LSB/ reattachment.

The spectral analysis of the full DNS domain Cp contour shows the presence of TS waves. The inception of TS waves induces a pressure wave that progressively growth in amplitude up to the flow transition, which is observed in both cases. However, because there is no inlet turbulence in the full DNS domain, the inception of TS waves is a little bit more chaotic, and advanced although it leads to the same behaviour as for the near wall domain, i.e. same period and location of transition

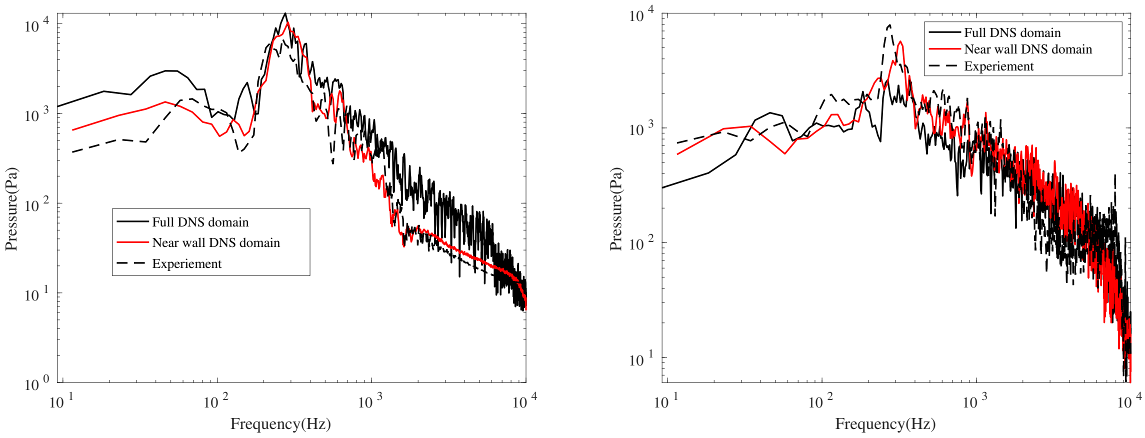

(A) x/c = 0.7 (B) x/c = 0.8

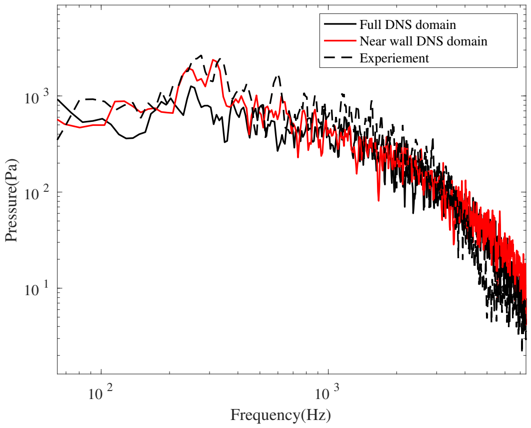

(C) x/c = 0.9

FIGURE 5.13: Spectral comparison of measured and DNS pressure signals for different chordwise locations, Re = 450,000

($x/c \approx 0.72$) and it is slightly distributed around $f/f_{TS(Exp)} = 1$ in both computations.

Fig.5.16 shows the comparison of spectra of V_x at three different locations along the chord ($x/c = 0.7, x/c = 0.8$ and $x/c = 0.9$) and It is obtained from monitor points located within the boundary layer, outside of the sub layer region. Overall a good comparison is observed in all the locations. Moreover, the peak at $x/c = 0.7$ demonstrates that the TS waves/ LSB shedding frequency match well. The velocity spectra at x/c = 1 shows the classical turbulent energy cascade law up to the finest cell size, that capture the smallest eddy, i.e; around $2\times\ 10^4$ Hz. (Fig.5.16(c)).

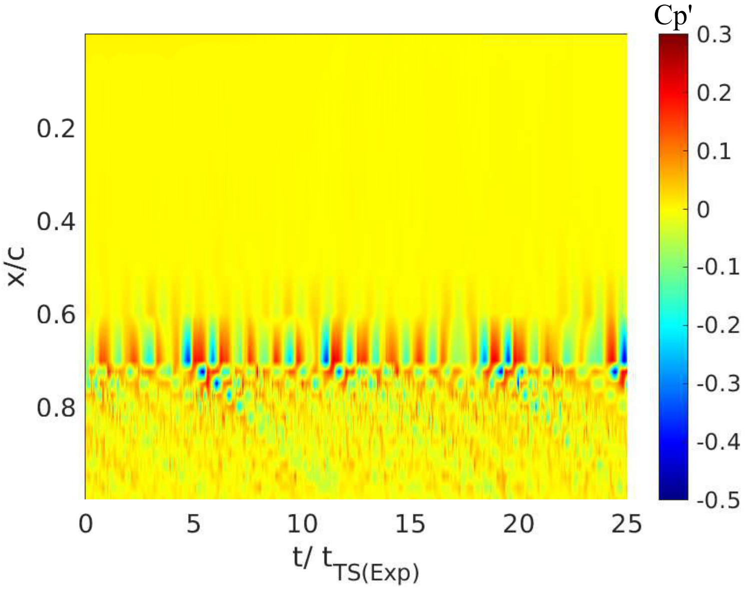

(A) Full DNS domain

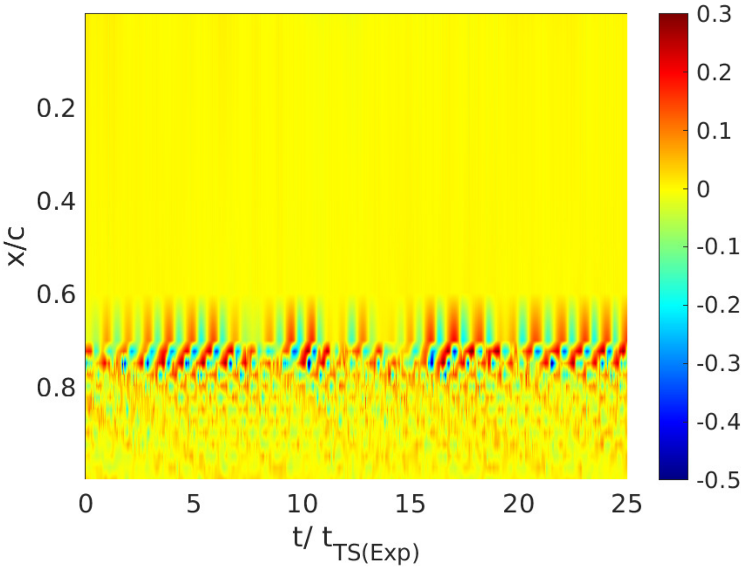

(B) Near wall DNS domain

FIGURE 5.14: Time evolution of computed wall pressure coefficient fluctuations along the chord of the hydrofoil, Re = 450, 000

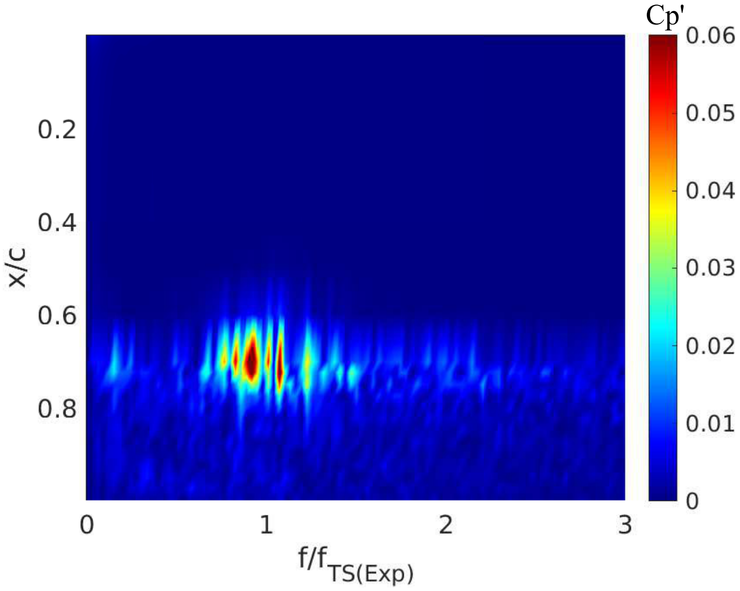

(A) Full DNS domain

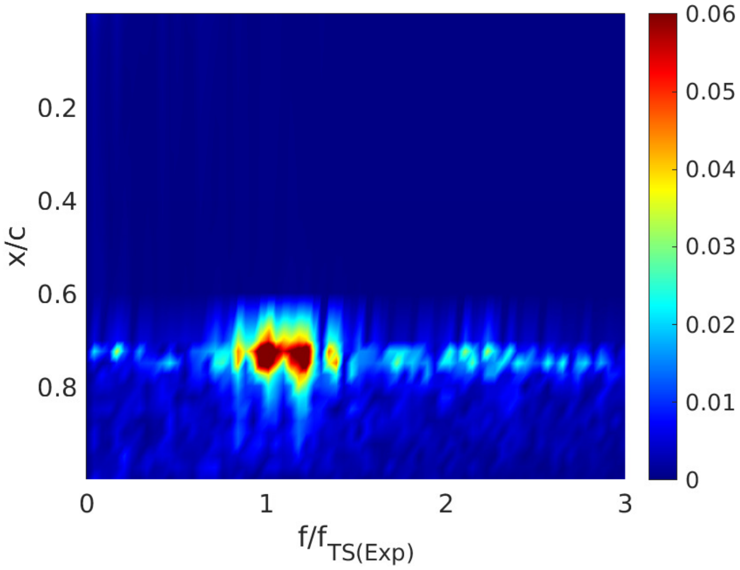

(B) Near wall DNS domain

FIGURE 5.15: Spectral analysis of time evolution of computed wall pressure coefficient fluctuations along the chord of the hydrofoil, Re = 450, 000

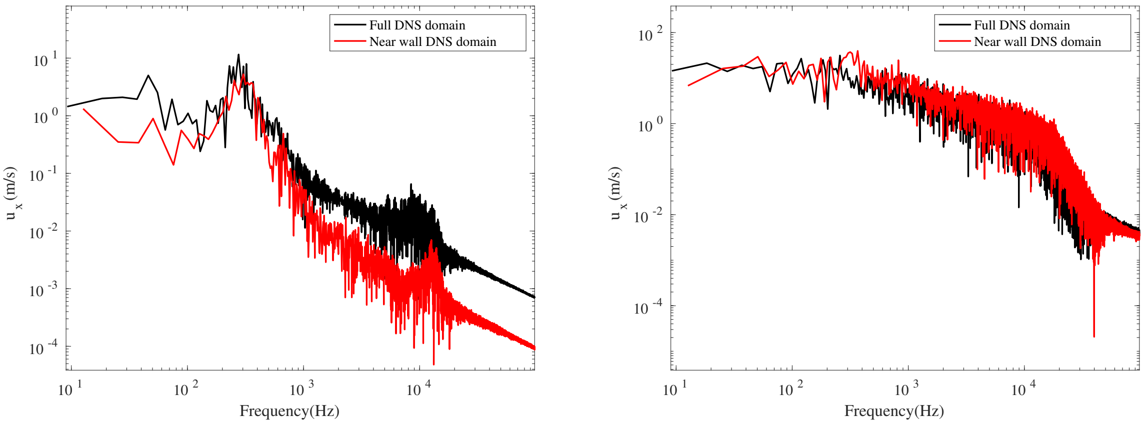

(A) x/c = 0.7 (B) x/c = 0.8

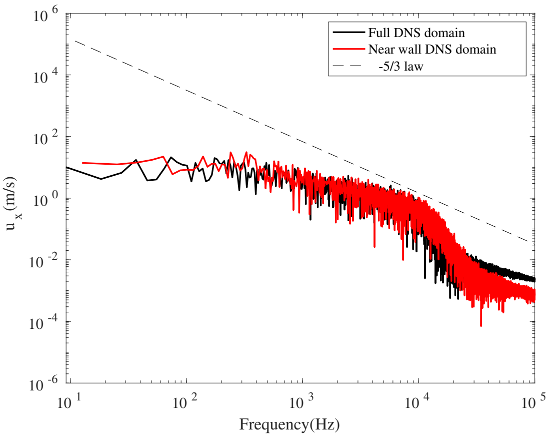

(C) x/c = 0.9

FIGURE 5.16: Spectra of U_x for three chord-wise locations at Re = 450, 000

5.3.2 Validation of Near Wall DNS boundary layer characteristics against Experiment

The boundary layer regime of the static NACA66 hydrofoil is investigated. The boundary layer characteristics obtained with the near wall DNS are compared to LDV experiments from Ducoin et al., 2012. The hydrofoil has the same section (NACA66), but the operating conditions are different, i.e $\alpha = 2°$, Re = 750,000 in experiment against $\alpha = 4°$, Re = 450,000 for the present numerical study.

TABLE 5.4: Comparison of boundary layer characteristics at $\alpha = 2°$, Re = 750,000 (Exp), $\alpha = 4°$, Re = 450,000 (Near wall DNS)

Location on the chord	H (Ducoin et al., 2012)	H (Near wall DNS)
Laminar	3.119	3.091
Laminar Seperation	4.050	4.080
In Core of LSB	4.548	4.669
Turbulent	1.593	1.555

Table 5.4 details the comparison of boundary-layer characteristics from laminar separation up to turbulent region and Fig.5.17 shows the corresponding boundary layer profiles. The numerical boundary layer profiles are averaged in time. From the comparison, we can conclude that the current near wall DNS domain is able to capture the boundary layer regime along the chord quite accurately. Although the operating conditions are different, the lower Reynolds number in the near wall DNS simulation is balanced by the higher angle of attack, which increases the adverse pressure gradient and moves the transition toward the leading edge, located in a thinner boundary layer. It results in equivalent boundary layer characteristics along the chord, in particular in the transition region.

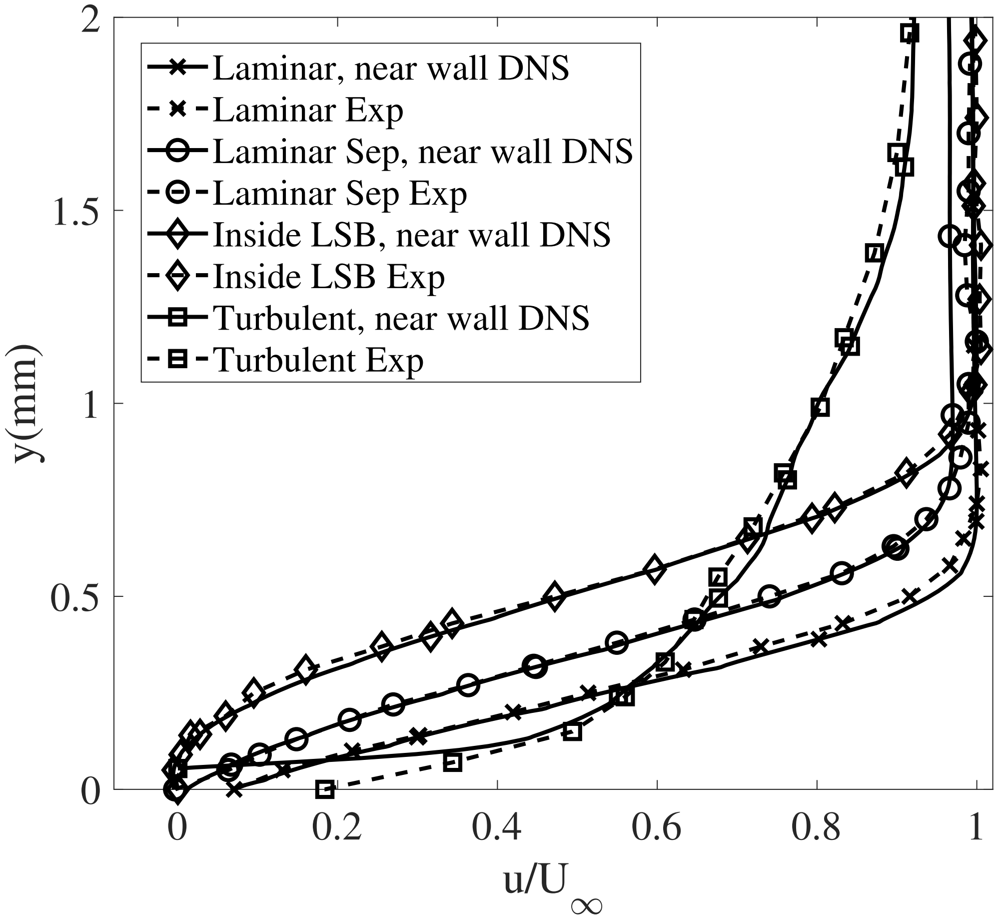

FIGURE 5.17: Comparison of mean velocity profiles between $\alpha = 2°$, Re = 750 000 (Exp, Ducoin et al., 2012) and $\alpha = 4°$, Re = 450 000 (near wall DNS) at different locations of chord.

5.3.3 Validation of FSI on NACA66 in Full DNS domain v/s Near Wall DNS

The confinement effects in the FSI computations can modify the structural behaviours such as the natural frequency of the hydrofoil, because it naturally adds an added mass component due to this numerical constrain. Thus, an appropriate correction is taken into account in the equation of motion to set the hydrofoil's natural frequency. In order to do that, a study on added mass effect at different confinement ratio is carried out.

Problem setup

In experiments, the hydrofoil is in a clamped free condition. The hydrofoil is assumed to be isotropic. In the cantilevered hydrofoil, flexibility increases as one moves from the root section up to the free tip section. Numerically, we focus on the flexibility of 5% portion of the full span towards the free end of the hydrofoil at z/s = 0.75, where s is the span of the foil and z is the coordinate along the spanwise direction. On the other hand, it allows to avoid the free tip of the hydrofoil, which is located close to the horizontal water tunnel wall. The structural parameters for 1 degree of freedom in pitch can be calculated from the shape functions(see, Appendix B). It has to be noted that although no measurements were performed on flexible hydrofoil at the considered Reynolds number (i.e. Re=450,000), the current numerical model is set in order to allow possible future experiments.

Two computational domains are shown in the Fig.5.18 and Fig.5.19, which are same as in the static cases except that a spring and damper is attached to the hydrofoil which having 1 DOF in pitch motion.

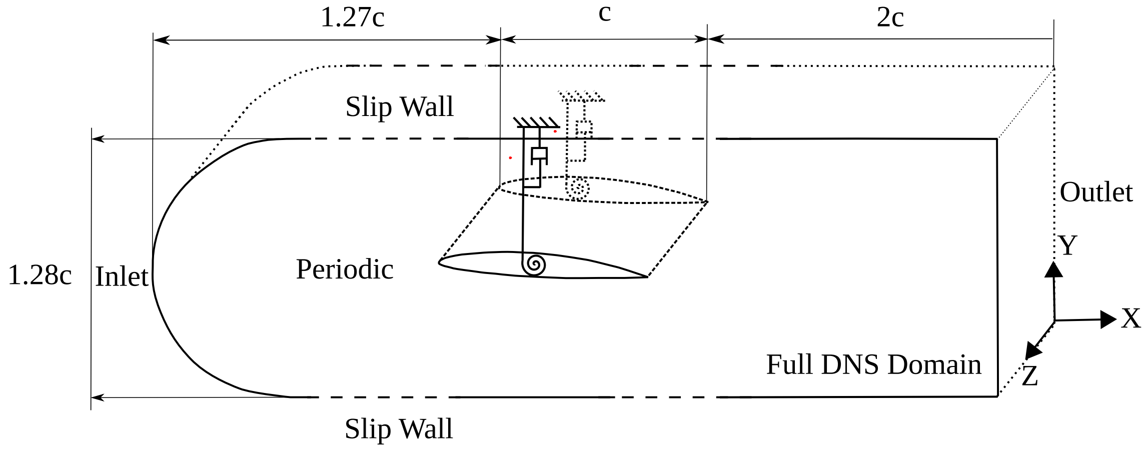

FIGURE 5.18: Computational setup for Full DNS domain of the FSI case

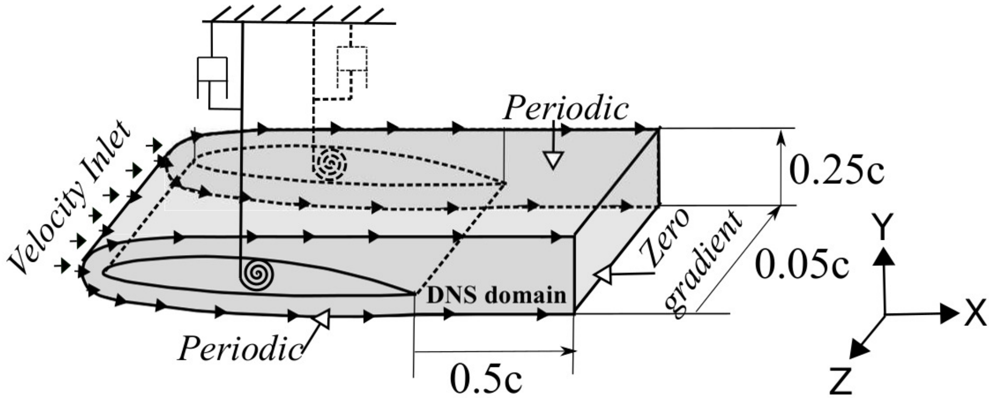

FIGURE 5.19: Computational setup for near wall DNS domain of the FSI case

The mesh is also the same as we have seen in Fig.5.4 and Fig.5.5. The structural parameters for both near wall and full DNS FSI cases are taken from the FSI A case (Table 5.1). Both cases are restarted from the corresponding converged static cases as we have seen in the previous section.

Added mass correction due to the near wall DNS domain

In order to make full resolution of DNS feasible, the fluid domain is restricted to an area smaller than the experimental test section. This numerical constraint contributes an additional added mass component in cases where the hydrofoil vibrates. To investigate the effect of this confinement on the added mass, a set of simulations were performed for a pitching NACA6612 hydrofoil, using Nek5000 at a range of confinement ratios (y/c). An analytical solution was also obtained as follows:

$$\tilde{m_a} = \pi \rho_l (c/2)^4 (1/8 + a^2) \tag{5.2}$$

where ρ_l is the density of the fluid, c is the chord and a is the distance between the center of pressure and the elastic axis.

The results of the simulations are compared to the analytical solution in Fig.5.20. Clearly, as the confinement ratio decreases, the added mass ratio increases. A value $\frac{m_a}{\tilde{m_a}} = 1$ corresponds to no confinement, i.e. the horizontal walls are at infinite distance. The green circle shows the value of added mass on the full DNS domain, or experimental domain; and the red circle shows the value of added mass on the current (near wall) domain, which is approximately 2.1 times greater. To account for this extra added mass, a correction factor is introduced into Eq. 2.20 as shown below.

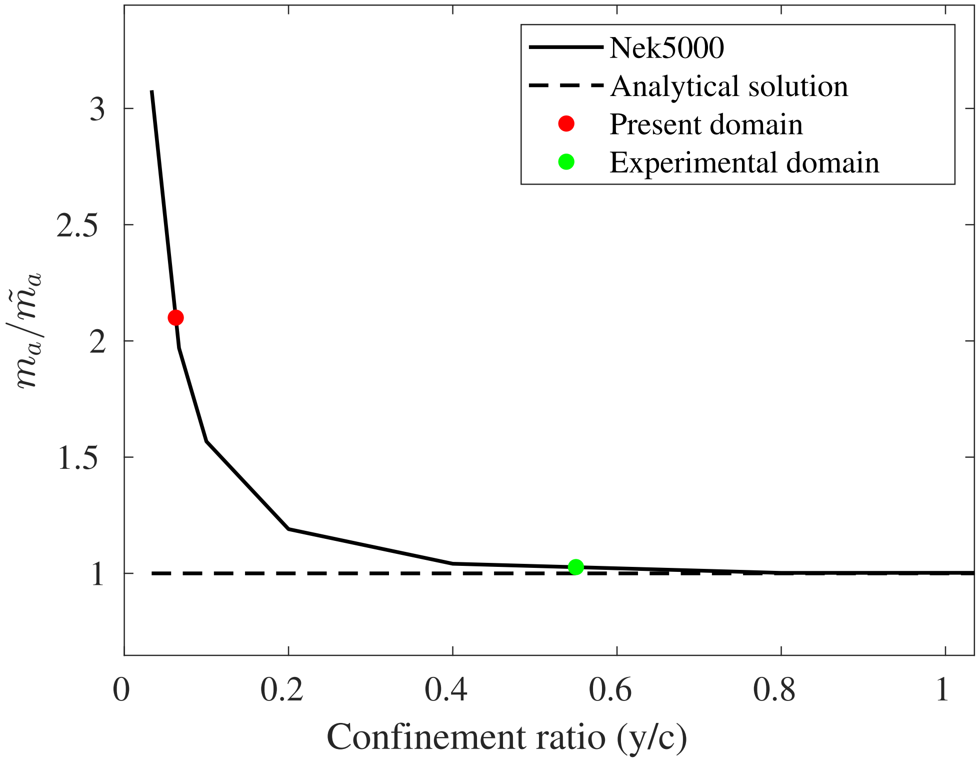

FIGURE 5.20: Comparison of added mass ratio at different confinement ratios (y/c), where y is the normal distance from the foil wall to the boundary. Here present domain is the Near wall DNS domain and Experimental domain is the Full DNS domain.

$$(I_\alpha + I_{corr})\ddot{\alpha} + D_\alpha\dot{\alpha} + K_\alpha\alpha = T_{EA} - T^0_{EA} \tag{5.3}$$

The expression for $I_{corr} = I_{a(FullDNS)} - I_{a(NearWallDNS)}$ where $I_{a(FullDNS)}$ and $I_{a(NearWallDNS)}$ are the added mass effect on foil inertia from Full DNS and Near Wall DNS domains, respectively. It is the difference between actual added mass effect in full DNS domain and the computed added mass in near wall DNS domain. If there was no correction term, the natural frequency of the system would be reduced due to the higher added mass. It is assumed that the added mass varies negligibly over time. Additionally, the term $-T^0_{EA,st}$ is intended to remove the mean torque calculated in the STATIC case. Hence, the static pitch deformation is removed and we are only analyzing the pitch fluctuations. This procedure is also applied to reduce the computational effort to converge to the static deformation, which should have a minor impact on the transition behaviour. It is interesting to remark that the confinement effect on added mass varies according to the type of degree of freedom (heaving, pitching etc..).

Wall pressure analysis

To show the response of the wall pressure to the hydrofoil pitching oscillations in both cases, the time averaged pressure coefficient along with instantaneous wall pressures are shown in Fig. 5.21. The pitching acceleration generates either a positive or negative pressure difference downstream and upstream of the elastic axis but it is not so evident in the current configurations due to the relative high rigidity of the hydrofoil. The pressure fluctuations (Cp') due to vibration in the laminar region of suction side is comparable in both cases. It proves that the acceleration of the near wall DNS domain hydrofoil is in good agreement with the full DNS domain. The difference in the transition is attributed to the absence of LSB in the full DNS simulation also the fluctuations are smoothened in the full DNS case because of the early transition.

A complete map of the wall pressure coefficients along the chord is shown in Fig. 5.22 for both cases. The pressure fluctuations due to the oscillation is weak between the leading edge ($x/c = 0$) and the transition region because of the low amplitude of foil oscillations. The maximum peak amplitude of fluctuations is observed in the transition region. The lower amplitude found in the full DNS domain is due to the absence of LSB (the LSB induces vortex shedding, then enhanced the pressures fluctuations). However, the amplitude of pressure fluctuations lies in the same order of magnitude.

.

FSI analysis

The aim of this section is to compare the input (Torque) to the hydrofoil's equation of motion and the corresponding velocity and pitch amplitudes in both configurations. The results are shown in Fig.5.23 and a good agreement is observed. A spectral analysis of velocity of the hydrofoil is also carried out and the comparison is shown in Fig.5.24. It is observed that the correction of added inertia in the near wall case has made the results comparable to the full DNS case in terms of velocity amplitude and frequency of oscillation. Because of the low amplitude of vibration set by the structural parameters, the hydrofoil vibrates at its natural frequency (F = 0.5), which is however modulated by the flow transition frequency.

As a conclusion for the validation of near wall domain v/s full DNS domain, the near wall DNS domain is chosen for further computations.

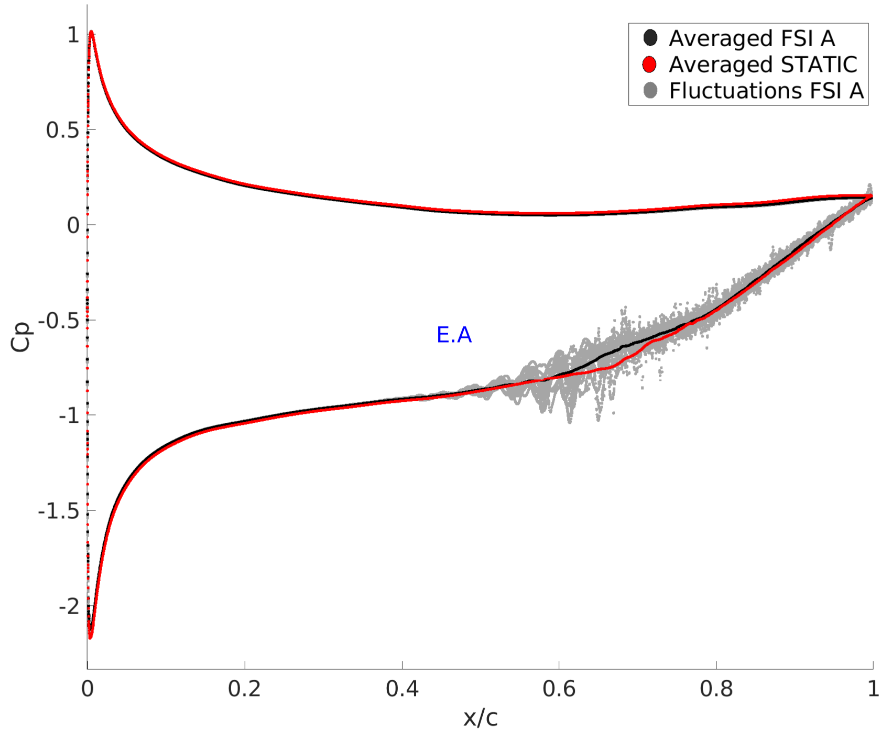

(A) Full DNS domain

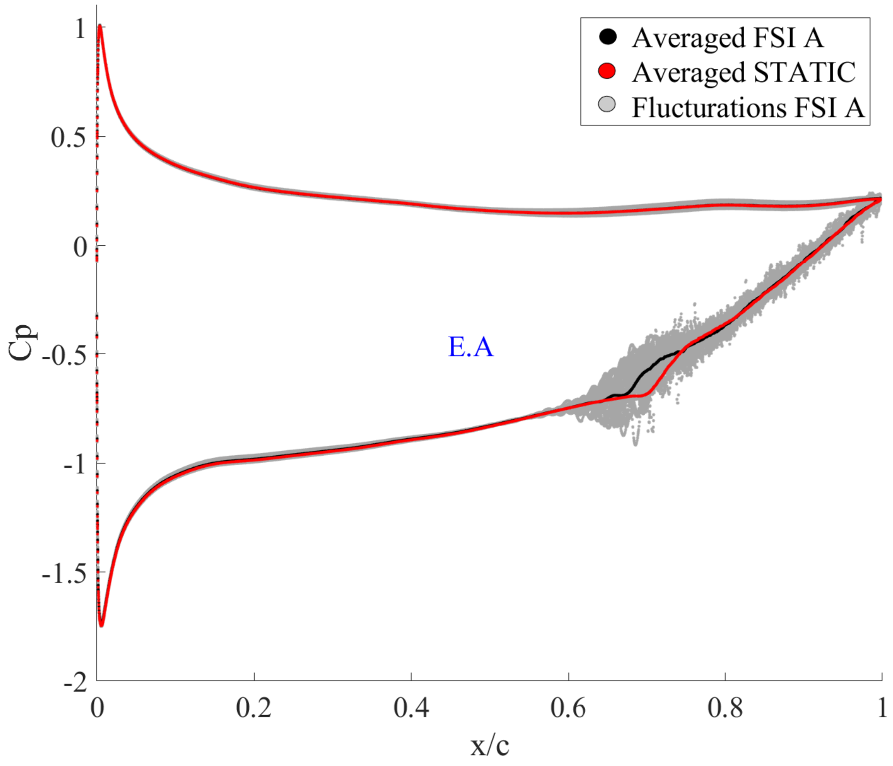

(B) Near wall DNS domain

FIGURE 5.21: Comparison of instantaneous and averaged coefficients of pressure between full DNS and near wall DNS domains.

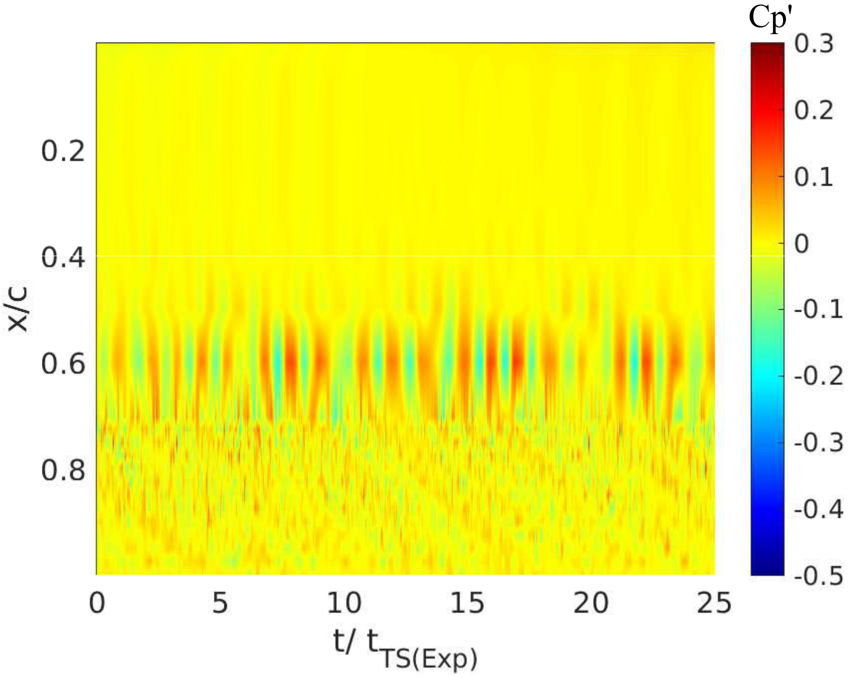

(A) Full DNS domain

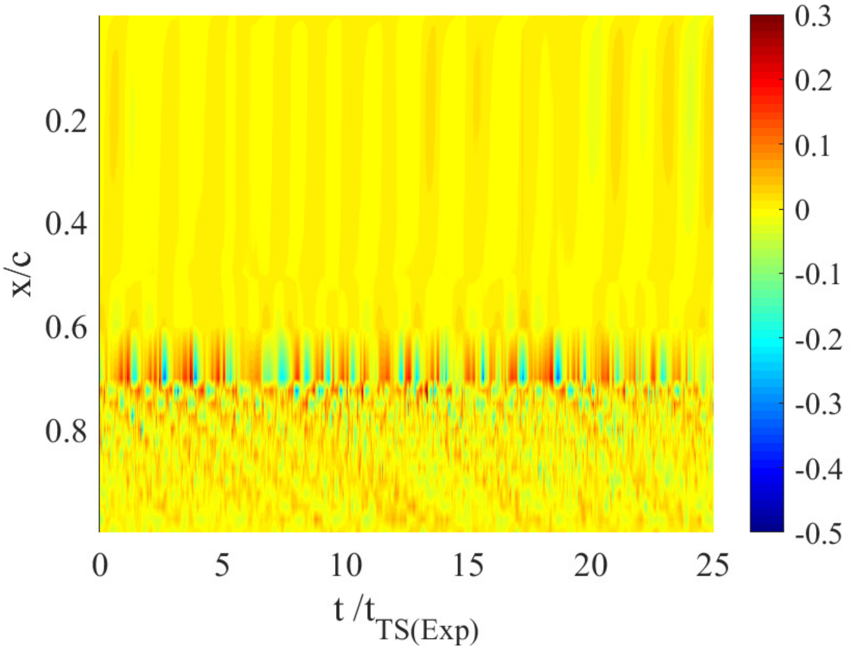

(B) Near wall DNS domain

FIGURE 5.22: Comparison of coefficient of pressure contour between full DNS and near wall DNS domains, flexible cases

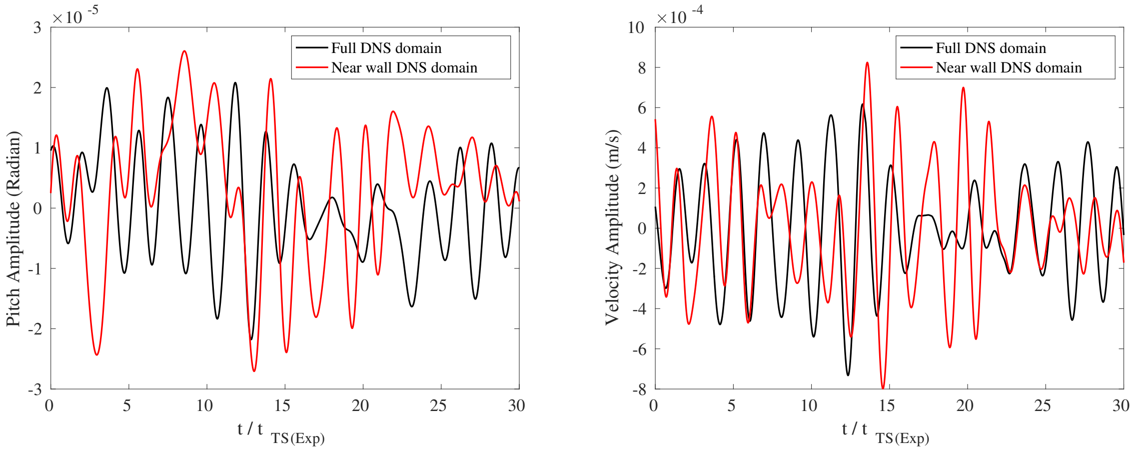

(A) Comparison of pitch amplitude

(B) Comparison of velocity amplitude

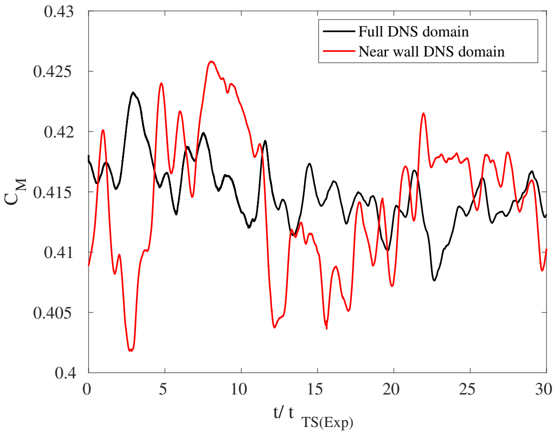

(C) Comparison of coefficient of moment

FIGURE 5.23: Comparison of FSI results from full DNS and near wall DNS domains

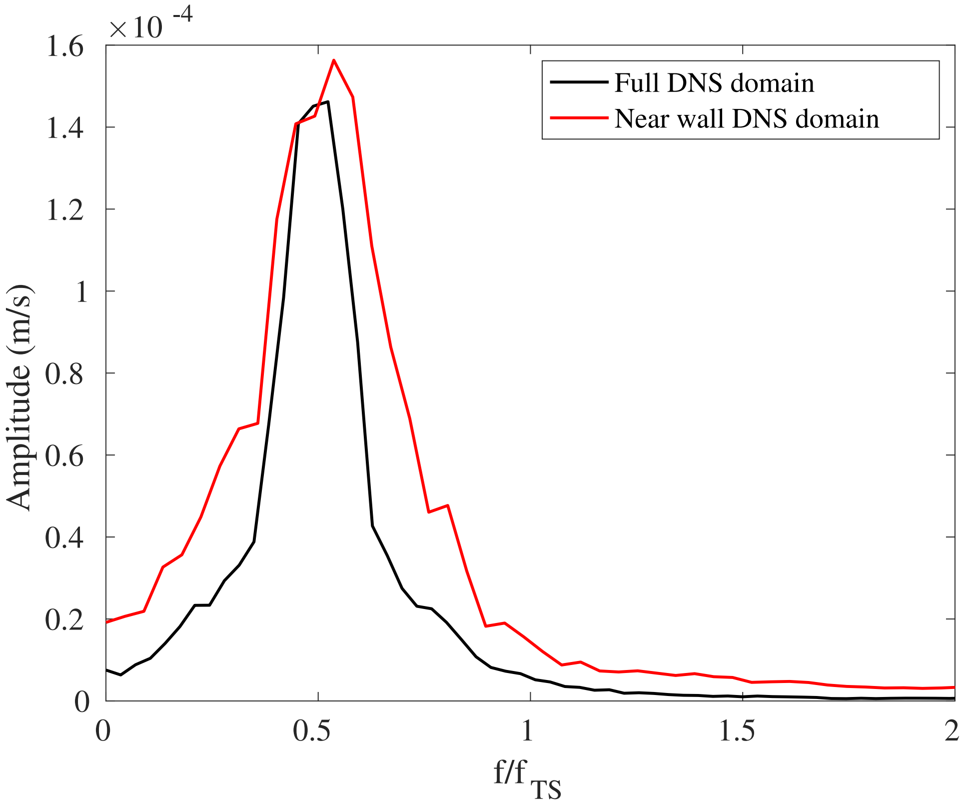

FIGURE 5.24: Comparison of spectral response of velocity magnitude from full DNS and near wall DNS domains

5.4 Results

A number of flexible cases are performed in this section namely FORCED A, FORCED B, FSI A, FSI B and FSI C. A prescribed maximum amplitude of oscillation, angular velocity and frequency is applied on FORCED cases by using Eq.4.1 whereas in FSI cases, Eq.**??** is used to allow the hydrofoil to pitch freely according to the fluid forces. All the flexible calculations are restarted from the converged static case.

Boundary layer flow analysis

In this section, we investigate the effect of the hydrofoil's vibrations on boundary layer characteristics and transition mechanism, comparing the coupled simulations to the static and forced-oscillation cases.

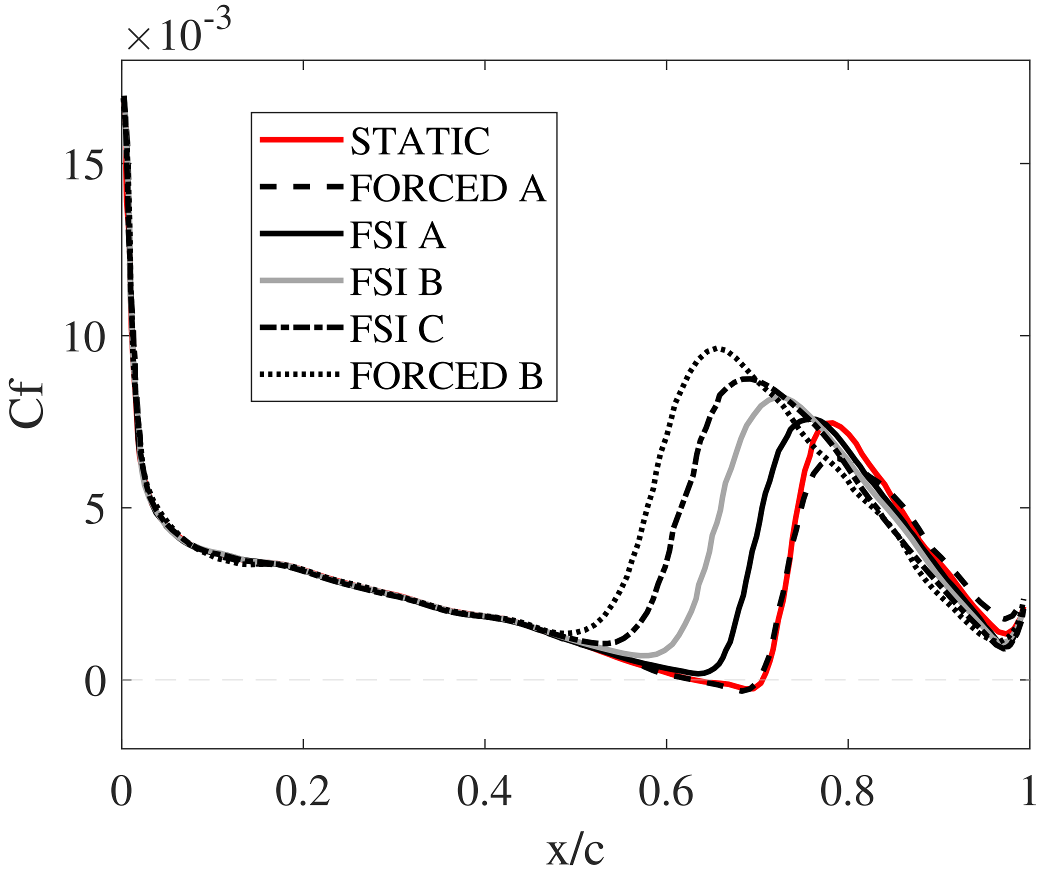

FIGURE 5.25: Comparison of skin friction coefficient between flexible and static cases at Re = 450, 000

Fig. 5.25 shows the spanwise, time-averaged friction coefficient in each case. The FORCED A simulation ($A_{\theta(max)} = 0.010$, $\dot{\alpha}^*_{(max)} = 0.0002$, $F = 0.5$) and static case show very similar behaviour, with laminar separation and reattachment of the flow occuring at $x/c = 0.62$ and $x/c = 0.71$ respectively. The transition is induced by the LSB. For higher values of ($A_{\theta(max)}$, $\dot{\alpha}^*_{(max)}$), the transition advances towards the leading edge, to a region of lower adverse pressure gradient, where C_f is always positive, corresponding to removal of the laminar separation and hence the LSB. It also results in a larger transition region. Indeed, the reduced size of the LSB over the NACA66 section renders it quite sensitive to small amplitude perturbations in the boundary layer. The transition location seems to be linearly dependent on ($A_{\theta(max)}$, $\dot{\alpha}^*_{(max)}$) as long as the frequency ratio F is maintained. In the case FSI C, whose frequency ratio is $F = 1.1$, the transition is advanced compared to FSI B, with $F = 0.5$. When the natural frequency is close to the transition frequency, the TS waves are seem more receptive to the hydrofoil's vibrations.

Fig.5.26 shows the boundary layer characteristics i.e. displacement thickness (δ_d), momentum thickness (θ_m) and shape coefficient ($H = \delta_d/\theta_m$). In the laminar region ($x/c < 0.5$), these characteristics are similar in all simulations; the shape coefficient, H, is approximately 3 in all cases. In the transition region ($0.5 < x/c < 0.8$), significant differences are observed: as flexibility increases, displacement thickness decreases. In the turbulent region ($x/c > 0.8$), increasing flexibility leads to an increase in δ_d and θ_m. In this region, H is approximately 1.5 in all cases.

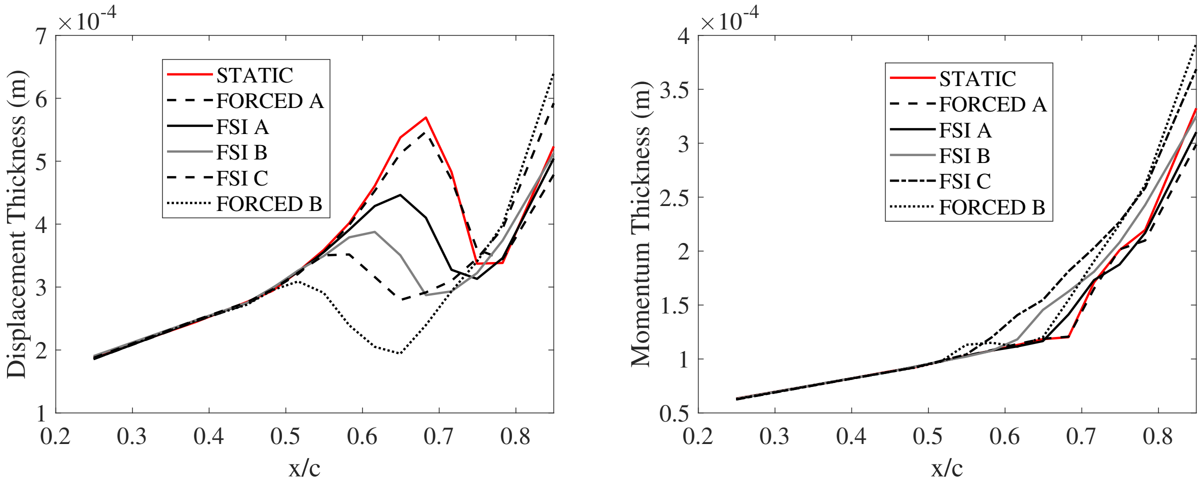

(A) Displacement Thickness v/s Chord

(B) Momentum Thickness v/s Chord

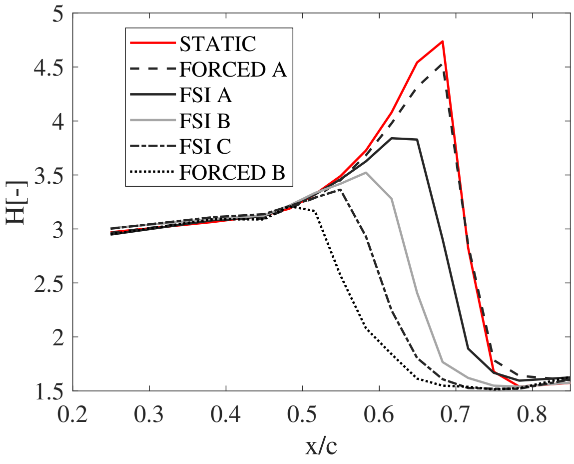

(C) Shape coefficient v/s Chord

FIGURE 5.26: Comparison of Boundary Layer Characteristics in flexible and static cases at Re = 450,000

Since the boundary layer characteristics are affected by the vibrations, the transition mechanism also changes. Fig.5.27 shows the iso-surfaces of λ_2 coloured with non-dimensional velocity (u/U_∞). Values of λ_2 are adjusted between the different cases to highlight the coherent structures. In the first stage of transition, spanwise deformation of the TS waves leads to formation of so-called, ”Hair-pin” structures; then turbulence develops up to the trailing edge ($x/c = 1$). As flexibility increases (higher A_θ, $\dot{\alpha}$), the transition position advances, which modifies the wave lengths of hairpin structures in chordwise and spanwise directions. Their shapes are also affected. The lower excitation cases (FSI A, FSI B and FORCED A) show similar coherent structures to the STATIC case. The FSI C case at F=1.1 is similar to the FORCED B case: both show quite sharp Λ structures, followed by an increase in turbulent mixing, corresponding to less flow periodicity after the breakdown. This highlights the effect of frequency ratio on the laminar-to-turbulent transition. The advance of transition leads to earlier establishment of the turbulent boundary layer. This is then subject to an adverse pressure gradient and trailing edge separation increases accordingly (blue contours). The same conclusion has been established experimentally in Ducoin and Astolfi, 2019, where an increase in Reynolds number led to an increase in low frequency pressure fluctuations associated with trailing edge separation.

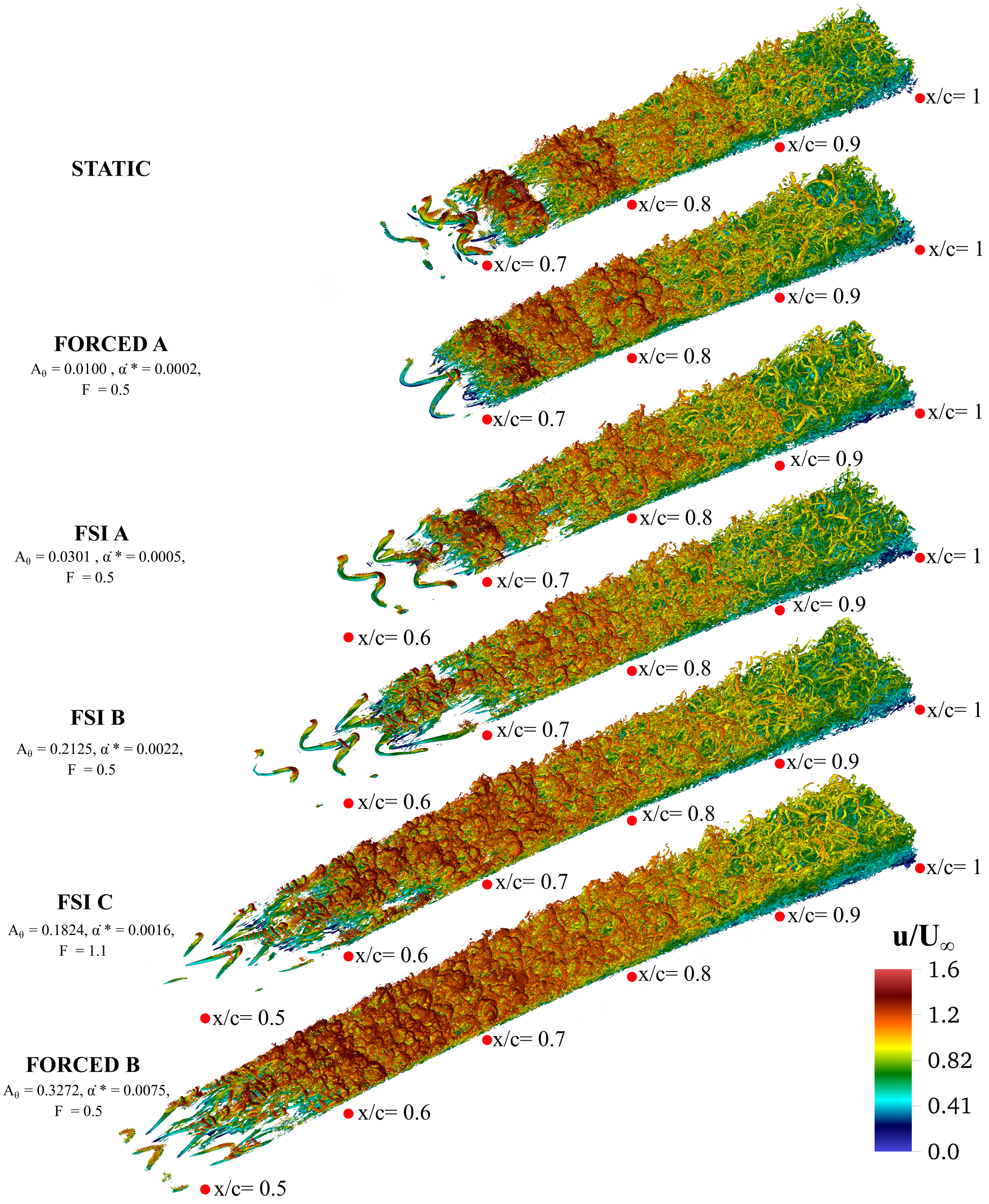

FIGURE 5.27: Comparison of instantaneous iso-surfaces of λ_2 coloured with velocity contours from flexible and static cases from transition to turbulent region at Re = 450,000

The hairpin(Λ) structures are compared qualitatively in Fig.5.28 and quantitatively in Table 5.5. As the transition advances, the hairpin structures are stretched in the chordwise direction, with increasing external velocity. In contrary, the spanwise wavelength decreases. A relationship is observed between the displacement thickness of the boundary layer (δ_d) and the spanwise dimension of the Λ structures (λ_z): λ_z decreases with decreasing δ_d. This results in a quasi-constant value of the ratio (λ_z/δ_d). It can be concluded that the spanwise wavelength of the hairpin structures is proportional to the boundary layer thickness.

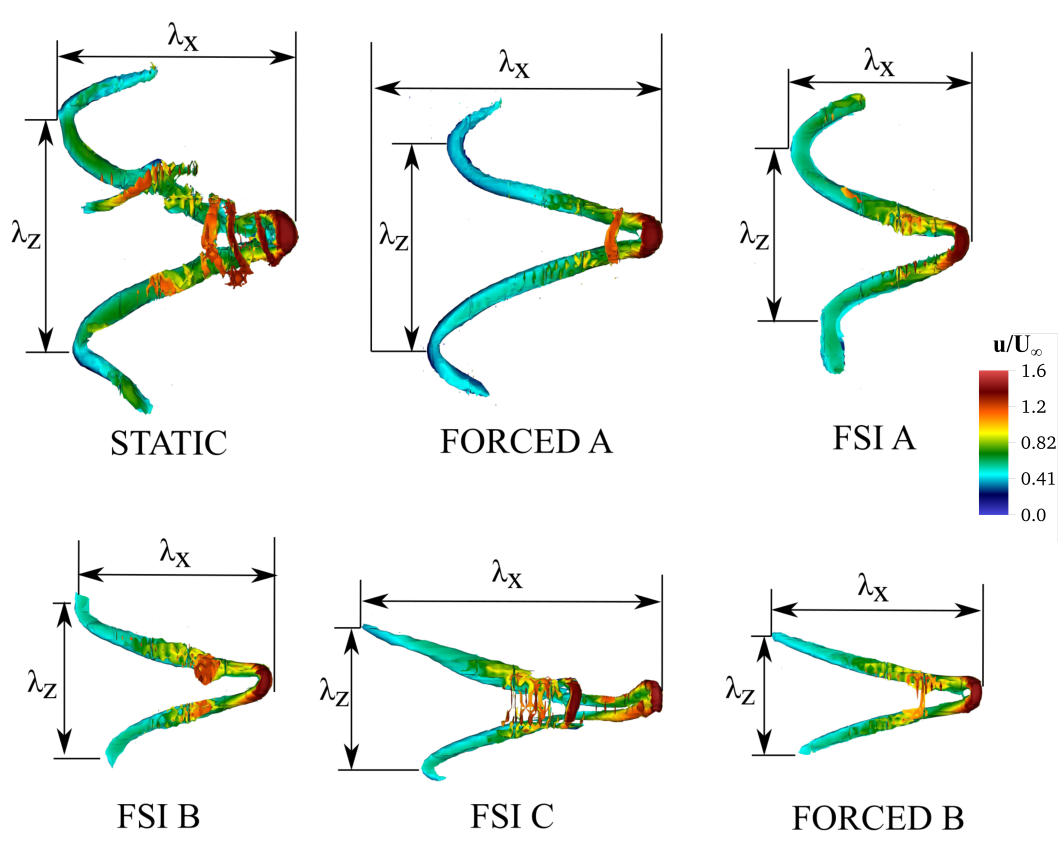

FIGURE 5.28: Comparison of λ_z dimension of iso-surfaces of Λ structures isolated from the flow in flexible and static cases at Re = 450, 000

TABLE 5.5: Relation between span-wise width of Λ structures (λ_z) and Displacement thickness (δ_d) in flexible and static cases

Cases	$\lambda_z(m)$	$\delta_d(m)$	λ_z/δ_d
STATIC	0.00449	0.000569	7.89
FORCED A	0.00422	0.000540	7.81
FSI A	0.00349	0.000446	7.82
FSI B	0.00302	0.000387	7.80
FSI C	0.00278	0.000351	7.92
FORCED B	0.00240	0.000308	7.79

Wall pressure analysis

To show the response of the wall pressure to the hydrofoil pitching oscillations, time-averaged and instantaneous pressure coefficients are shown in Fig.5.29. For hydrofoils of increasing flexibility, the pitching acceleration generates either a positive or negative pressure difference downstream and upstream of the elastic axis; however, the time-averaged pressure coefficients remain quite similar to the static case. As ($A_{\theta(max)}$, $\dot{\alpha}^*_{(max)}$) and frequency ratio (F) increase, the pressure plateau disappears with the LSB. Finally, when $F = 1.1$, TS waves appear upstream of the elastic axis (see Fig.5.29(e)), i.e. in the laminar region. Again, this suggests that the TS waves are receptive to the vibration, particularly when their periods become similar, which enhances the interactions.

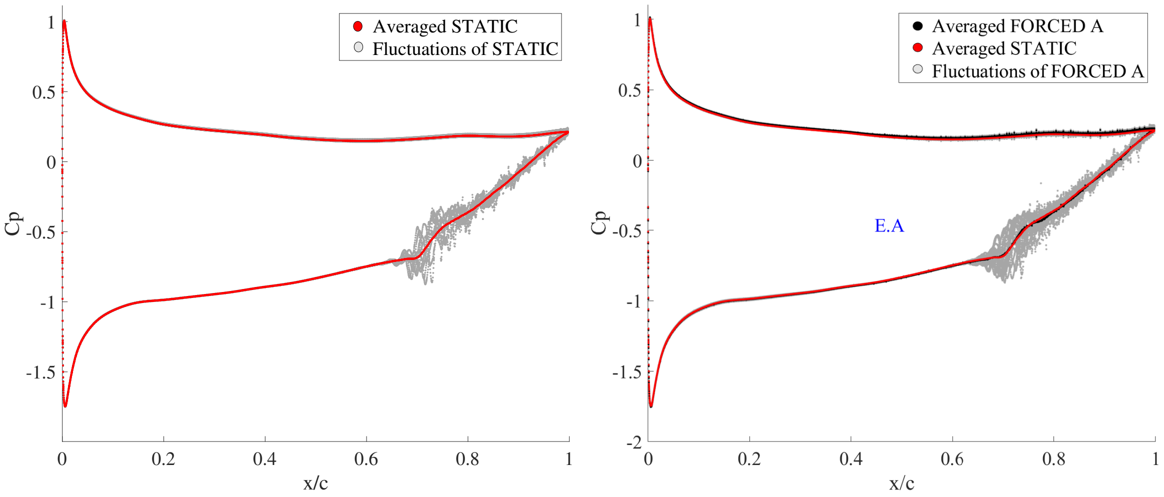

(A) Cp STATIC (B) Cp FORCED A

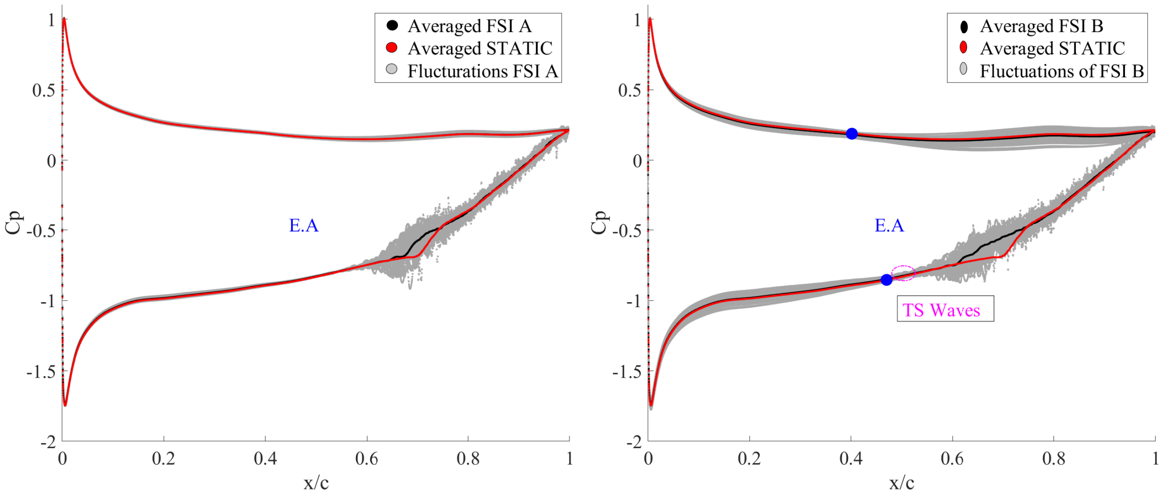

(C) Cp FSI A (D) Cp FSI B

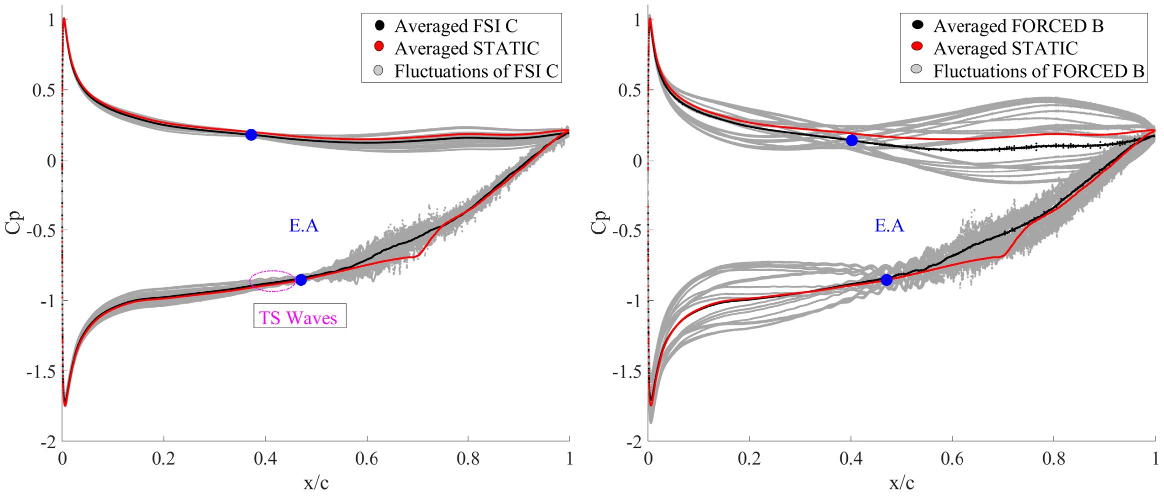

(E) Cp FSI C (F) Cp FORCED B

FIGURE 5.29: Comparison of instantaneous and time-averaged pressure coefficients at Re = 450, 000

To investigate the effect of pitching on TS pressure waves, the pressure coefficient fluctuations are shown in Fig.5.30. In order to facilitate comparison of the length (x/c) and the intensity of the pressure wave, the chord location of the inception of the wave is taken to be 0. The static case is characterised by a high-amplitude sinusoidal fluctuation after the inception of the TS wave associated with the flapping of the LSB. After reaching maximum amplitude, the flow starts to transition to turbulence. Similar behaviour is observed in the FORCED A case. As flexibility increases and the transition point advances, the pressure fluctuation intensity decreases progressively, so that the first stage of transition (2D laminar TS waves) is extended. This is due to the larger disturbance induced by vibrations, which advance the TS waves and incept in a lower local Reynolds number (Re_X) region.

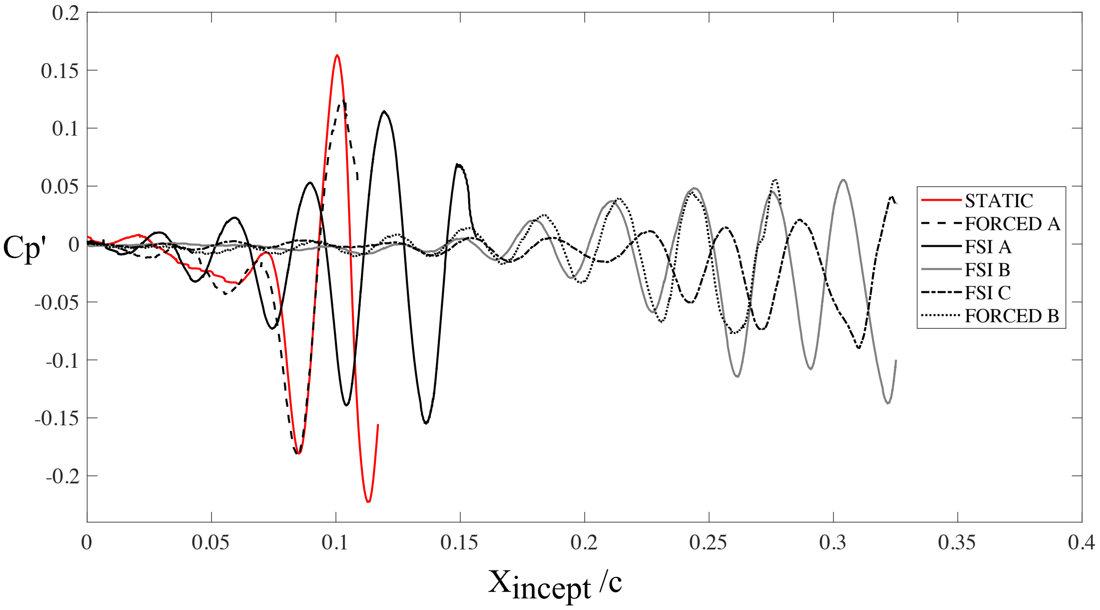

FIGURE 5.30: Comparison of pressure coefficient fluctuation due to TS waves at the suction side in flexible and static cases at Re = 450,000.

Exhaustive wall pressure data is presented in Fig.5.31. In all flexible simulations, pressure fluctuations due to the oscillation are observed between the leading edge ($x/c = 0$) and the onset of development of turbulence. In the transition region, the maximum peak amplitude is located in the early development of hairpin structures. As hydrofoil flexibility increases:

- pressure fluctuations due to the hydrofoil's acceleration increase, and in the most flexible cases, eventually overlap the turbulent pressure fluctuations (Fig.5.31 ((d), (e) and (f)). The contour plots reveal a clear difference between the forced and the free pitch cases, in that the forced pitch cases are characterised by a purely sinusoidal response, whereas free pitch clearly interacts with the flow.
- the intensity of pressure fluctuations decreases in the transition region, which becomes longer chordwise.
- for the FORCED B case ($A_{\theta(max)}$ = 0.3272, $\dot{\alpha}^*_{(max)}$ = 0.0075, $F = 0.5$), the acceleration induced by the forced pitch oscillation clearly dominates the wall pressure.

Fig.5.32 shows the spectral analysis of wall pressure fluctuations along the chord. Note that the scale varies between figures, reflecting the differing magnitude of periodic pressure fluctuations. As expected, the static simulation has a principal frequency peak in the transition region ($x/c = 0.7$, $f/f_{TS} = 1$). In FORCED A (Fig.5.32(b)), an additional local frequency peak of low magnitude is observed in the transition region around $f/f_{TS} = 0.5$, $0 < x/c < 0.6$ suggesting a first effect of the pitch on the pressure response. With a much larger $\dot{\alpha}^*_{(max)}$, FORCED B shows a local peak along the length of the chord at $f/f_{TS} = 0.5$, as well as its harmonic at $f/f_{TS} = 1$.

FSI A, despite having a pitch oscillation of similar order of magnitude to FORCED A ($\dot{\alpha}^*_{(max)} = 0.0005$), shows a quite different response. The free motion induces a large band frequency of excitation between $0.2 < f/f_{TS} < 1.2$, visible in the laminar region ($0 < x/c < 0.5$). The maximum peak still occurs at $f/f_{TS} = 0.5$, i.e. at the natural frequency ($F = 0.5$). As flexibility increases (Fig.5.32 (d) and (e)), the natural frequency components are more visible along the chord, whereas the transition frequencies are more localised, suggesting a direct effect of the pitch oscillation on the transition. It can also be observed that in the FSI C case ($F = 1.1$) the transition frequency is enhanced compared to the FSI B case ($F = 0.5$). The pitch acceleration is consequently enhanced, i.e. it shows a larger band frequency response (see figure 5.32 (e), $0.2 < F < 1.3$ for $0 < x/c < 0.4$) whereas the maximum peak amplitude have slightly decreases.

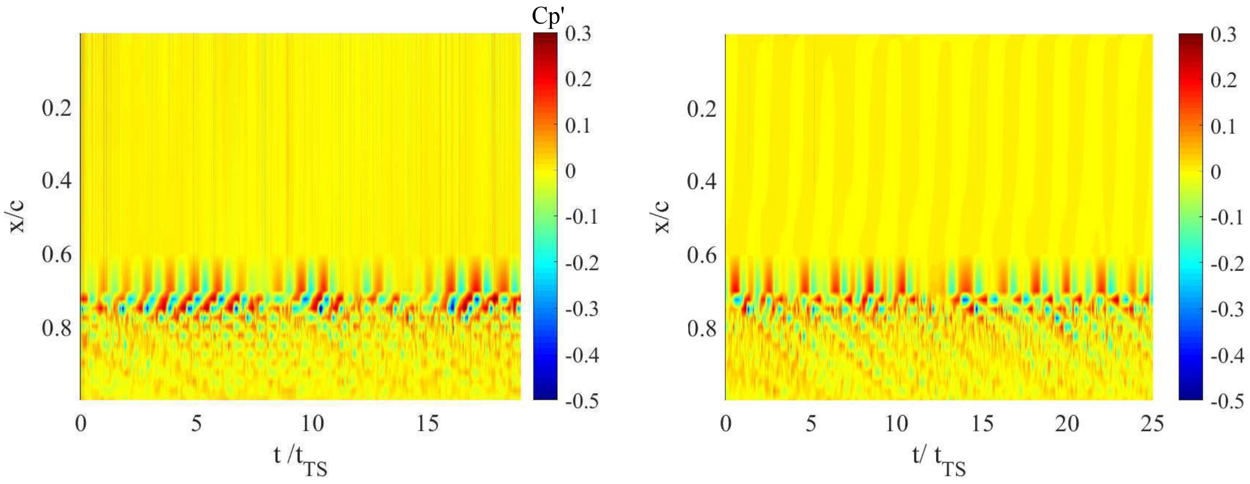

(A) Wall pressure contour in STATIC

(B) Wall pressure contour in FORCED A

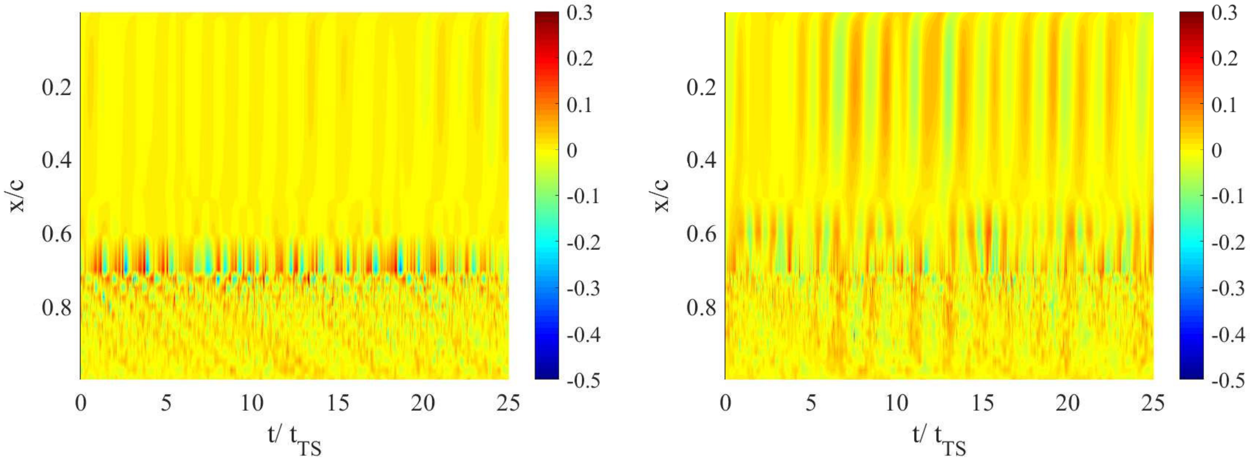

(C) Wall pressure contour in FSI A

(D) Wall pressure contour in FSI B

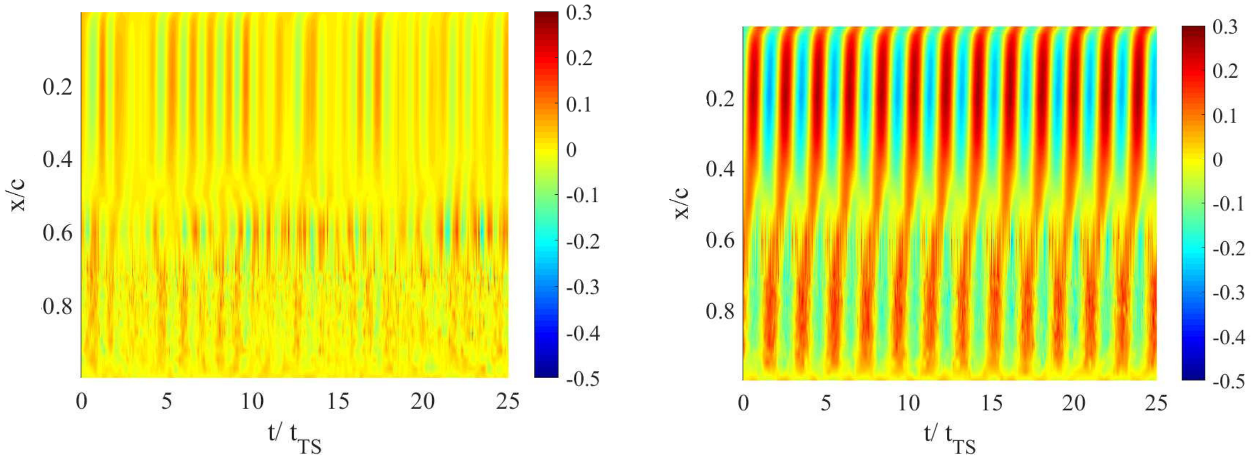

(E) Wall pressure contour in FSI C

(F) Wall pressure contour in FORCED B

FIGURE 5.31: Time evolution of computed wall pressure coefficient fluctuations along the chord of the hydrofoil in flexible and static cases, Re = 450, 000

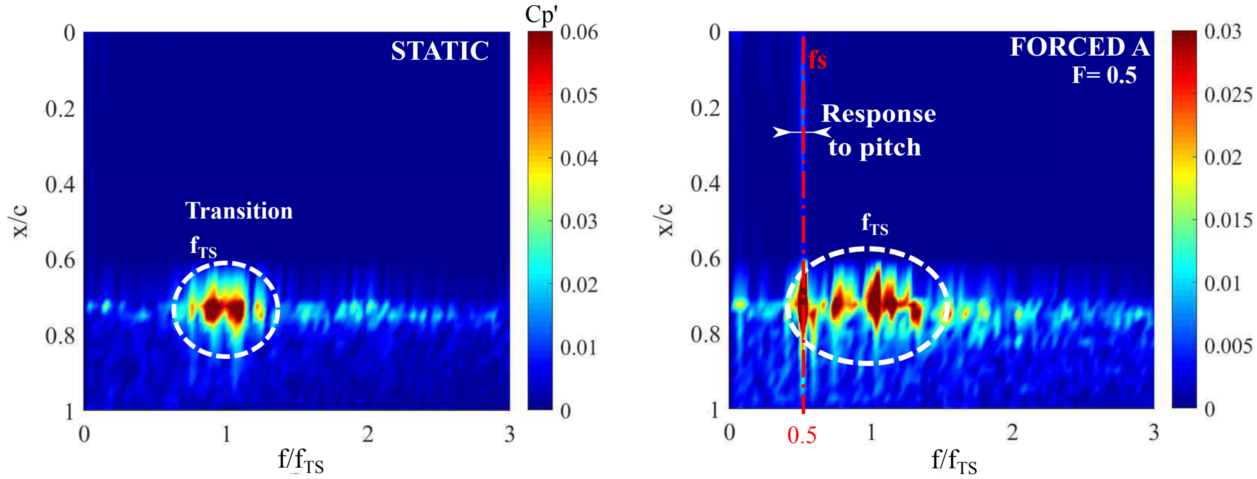

(A) Frequency spectra of Cp contour in STATIC

(B) Frequency spectra of Cp contour in FORCED A (F = 0.5)

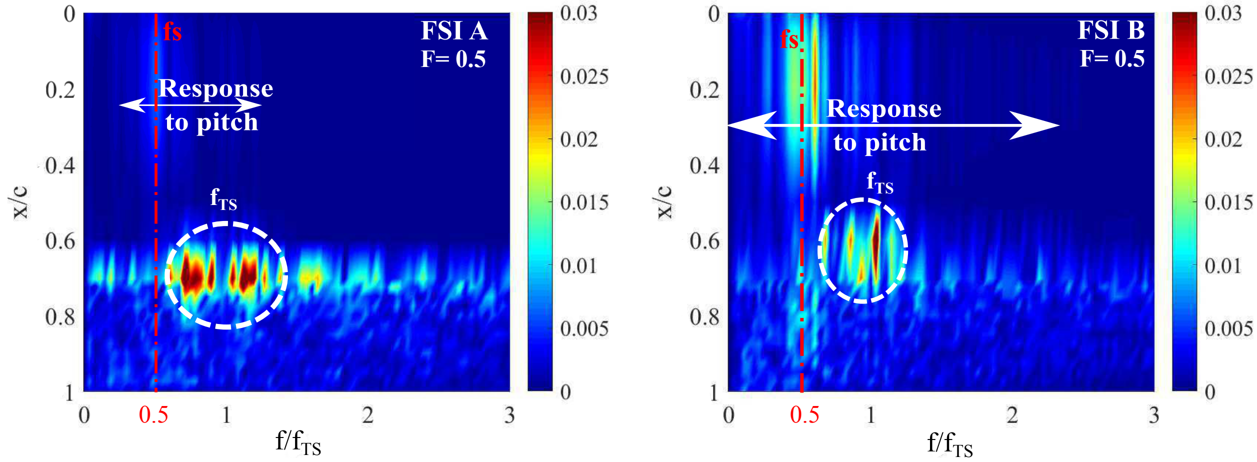

(C) Frequency spectra of Cp contour in FSI A (F = 0.5)

(D) Frequency spectra of Cp contour in FSI B (F = 0.5)

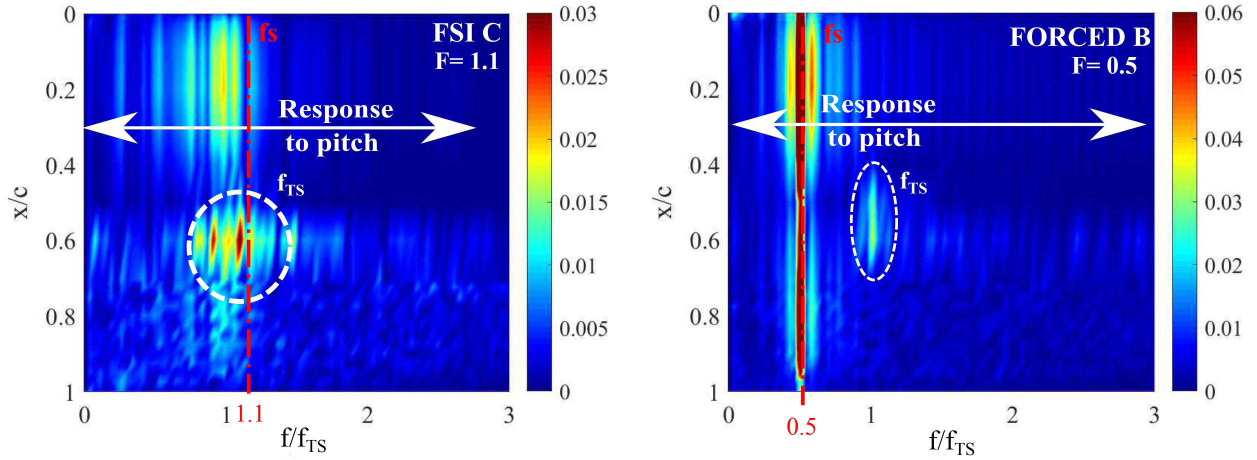

(E) Frequency spectra of Cp contour in FSI C (F = 1.1)

(F) Frequency spectra of Cp contour in FORCED B (F = 0.5)

FIGURE 5.32: Spectra of computed wall pressure coefficient fluctuations v/s Frequency ratio (f/f_{TS}) in flexible and static cases, Re = 450, 000

FSI analysis

In the last section of the results, FSI simulation results are compared to highlight fluid-structure interactions between the pitching mode and the transition. Fig.5.33 shows the non-dimensional pitch amplitude (A_θ) compared to the moment coefficient (C_M).

For FSI A ($F = 0.5$), there is little correlation between the torque and pitch response. The amplitude of pitch angle is small. The foil motion and the flow are not coupled. For FSI B ($F = 0.5$), the pitch response is larger, due to the higher flexibility, which induces a correlation with the moment coefficient; that is, the pitch induced an additional torque fluctuation. For FSI C, whose $A_{\theta(max)}$ and $\dot{\alpha}^*_{(max)}$ are similar to FSI B, the frequency ratio close to 1 ($F = 1.1$) leads to strong correlation between pitch angle and torque.

Fig.5.34 shows the pitching velocity spectra for the coupled calculations. It has been smoothed to highlight the main frequency peaks. In FSI A ($F = 0.5$), a dominant peak is observed at the natural frequency $(f/f_{TS} = 0.5)$. The transition frequency is not visible because hydrofoil is too rigid. The interaction between the transition and natural frequencies are not observed in this case. However, the flow field is slightly altered which has been already discussed before in this thesis. In FSI B ($F = 0.5$), the dominant peak still occurs at $(f/f_{TS} = 0.5)$ but with a larger amplitude of vibration due to the higher flexibility. An inception of a transition frequency at $f/f_{TS} = 1$ is also observed. In FSI C, a multi-scaled frequency response is observed between $0.35 < f/f_{TS} < 1$, whose maximum amplitude occurs at the transition frequency $(f/f_{TS} = 1)$. A similar multi-scaled frequency response was observed experimentally by Ducoin et al., 2012 at $\alpha_0 = 4°$ and Re = 900,000 to 1,100,000 (see, Figure 5). This suggests that when the frequency ratio is close to 1, the transition is more receptive to the hydrofoil's vibrations, and it mechanism is then disturbed.

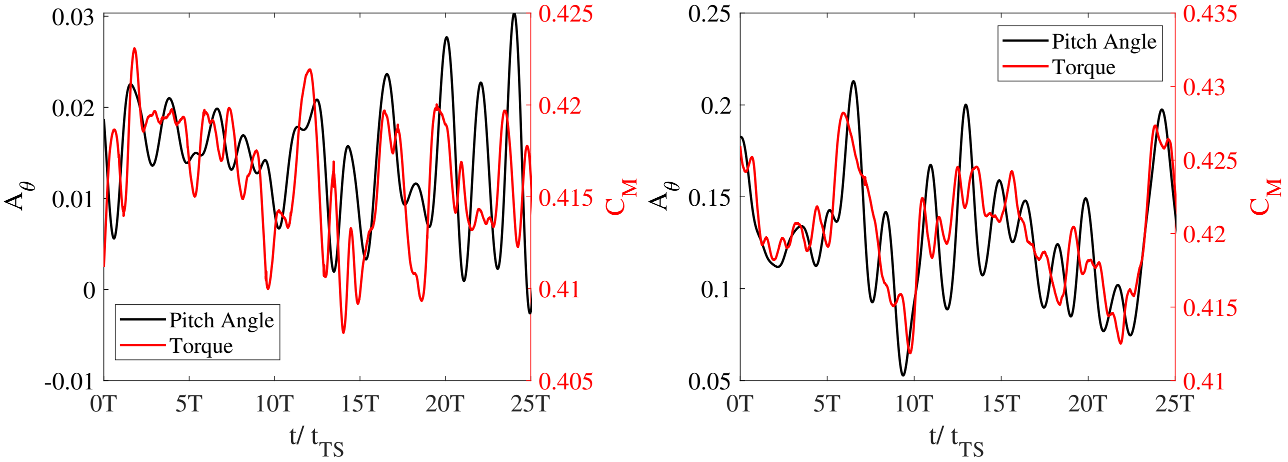

(A) Time evolution of pitch angle in FSI A

(B) Time evolution of pitch angle in FSI B

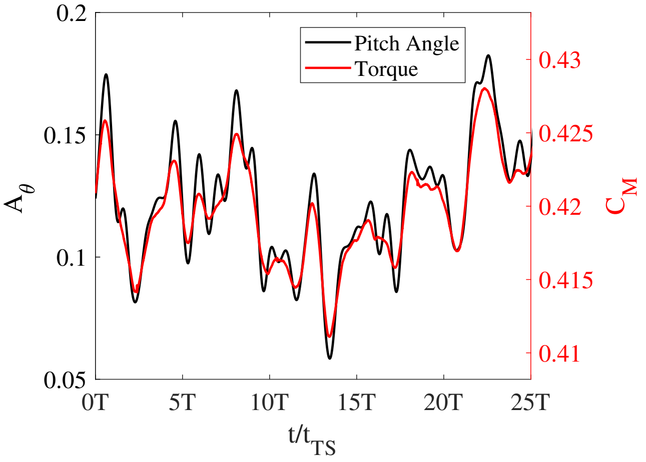

(C) Time evolution of pitch angle in FSI C

FIGURE 5.33: Comparison of flexible hydrofoil pitch angle and moment coefficient in FSI A ($A_{\theta(max)} = 0.0301$), FSI B ($A_{\theta(max)} = 0.2125$) and FSI C ($A_{\theta(max)} = 0.1824$) at Re = 450, 000

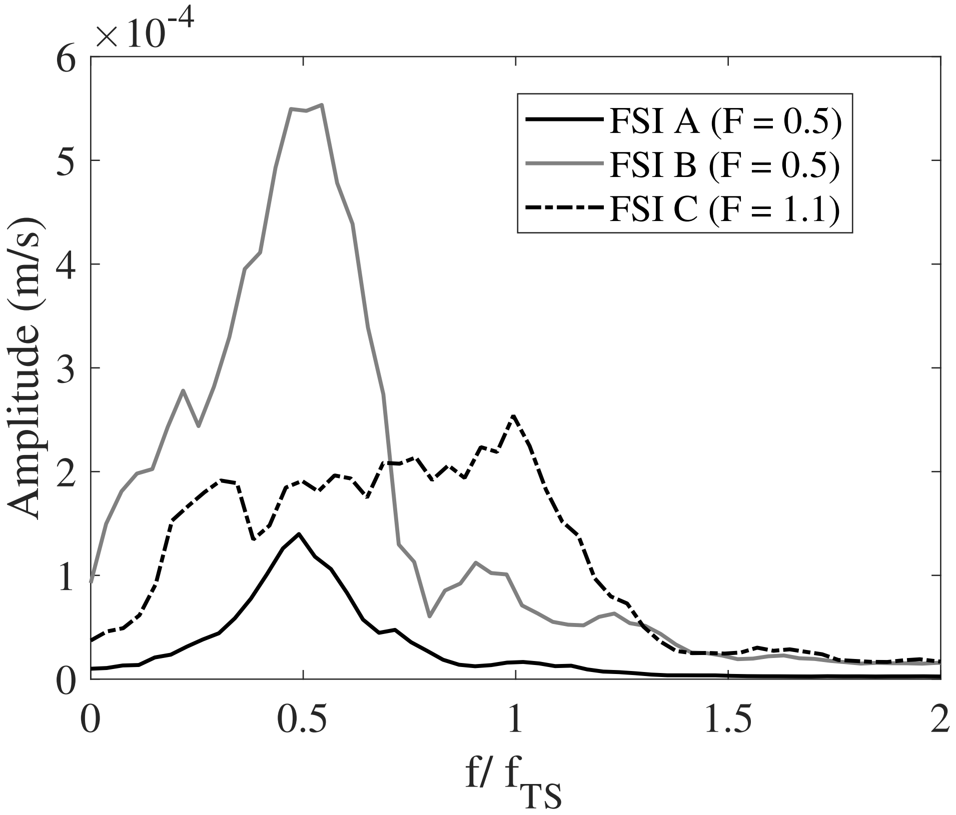

FIGURE 5.34: Comparison of flexible hydrofoil velocity spectra in FSI A ($A_{\theta(max)} = 0.0301$, $\dot{\alpha}^*_{(max)} = 0.0005$), FSI B ($A_{\theta(max)} = 0.2125$, $\dot{\alpha}^*_{(max)} = 0.0022$) and FSI C ($A_{\theta(max)} = 0.1824$, $\dot{\alpha}^*_{(max)} = 0.0016$) at Re = 450, 000

5.5 Conclusion

In this section, a 1-DOF DNS coupling of a NACA66 propeller section subjected to laminar to turbulent transition at Re=450,000 is investigated. A set of non-dimensional parameters are derived to characterize the FSI. Finally, following conclusions are made :

- The spatial location of transition point is proportional to the amplitude of pitch A_θ, velocity($\dot{\alpha}^*$) and frequency ratio (F). As the degree of flexibility increases, the transition occurs earlier. It is also observed that the span-wise wavelength of the hair-pin structures is proportional to the displacement thickness.
- The pressure gradient is affected by the motion of the foil. However, the averaged pressure plateau of the static and flexible hydrofoils cases are quite similar except in the transition region. The amplitude of pressure fluctuations in the transition region were decreased, as the location of transition advances conversely the length of transition region is increased.The TS waves are sensitive to the natural/ vibration frequency of the system especially if the frequency ratio (F) is close to 1.
- The transition frequency does not make much effect on the vibration frequency of the foil especially in FSI A and FSI B. However, an inception of transition frequency is observed in the foil vibration of FSI B. The FSI C is more complex case and some extra intermittent/ transient behaviour is observed in its pitch response and the corresponding spectra.

Conclusion

In this thesis work, a first attempt is made to investigate the dynamic of transition induced vibration over a flexible hydrofoil, derived from a marine propeller section. For that purpose a DNS-1DOF coupling has been developed. The spectral element code Nek5000 is used to solve the fluid flow and it is coupled with an equation of motion, derived for the pitching of rigid hydrofoil. The foil's motion reproduces the torsional deformations of one section of a clamped free hydrofoil. The Reynolds number is significantly high, i.e. Re=450,000, in order to be able to match with experiments in tunnel test section, which can be possibly conducted in the near future.

First, a series of validation with existing literature was performed on different cases, with increasing complexity from VIV over a cylinder, to limit cycle oscillation of a NACA0012 hydrofoil in transitional flows. It shows the ability of the current method (DNS - 1DOF coupling) to efficiently simulate fluid structure interaction problems with different flow dynamics.

In the investigated case, an original technique was developed in order to reduce the computational expense. DNS domain is reduced to the near wall region of the hydrofoil, along with stationary velocity boundary conditions from a full DNS domain that were set at the inlet and the top and bottom walls. Hence, the current domain was validated by comparing the results to a full DNS domain for both rigid and coupled configurations. Also, the span length of the DNS domain is set to 0.05c which is slightly greater than the minimum value required to capture the 3D boundary layer flow in the transition region, particularly the hair-pin structures.

Followed by the validation studies, the transition induced vibration on the NACA66 hydrofoil is then investigated. A parametric study, consisting of two forced oscillations (FORCED A and FORCED B) and 3 free oscillations (FSI A, FSI B ,and FSI C) allowed to analyze the change in the boundary layer flow, in wall pressures and in the hydrofoil structural behaviour due to fluid structure interactions. In this thesis, an attempt to characterize the fluid structure interaction in transitional flows is performed, with non dimensional parameters based on boundary layer quantities in the transitional region of the boundary layer, and the hydrofoil response. The structural properties of the 1DOF model were chosen in order to match the one with existing experiments (case FSI A), and different degrees of flexibility in terms of pitch amplitude (A_θ), velocity ($\dot{\alpha}^*$) and frequency ratio (F) were set to investigate transition induced vibration numerically.

From the boundary layer flow analysis, it was observed that the spatial location of the transition point is proportional to the amplitude of pitch, velocity, and frequency ratio. As the degree of flexibility increases, the transition advances spatially along the chord. The boundary layer characteristics are affected even by oscillations of very small amplitude. It was also observed that the spanwise wavelength of the hairpin structures is proportional to the displacement thickness. The pressure gradient was affected by the motion of the foil, but the time-averaged pressure coefficients of the static and flexible cases showed good agreement outside of the transition region. The spatial advancement of the transition point reduced the amplitude of periodic pressure fluctuations in the transition region. Additionally, the length of the transition region was increased. The generation of TS waves is sensitive to the amplitude of vibration and frequency ratio of the system, being observed earlier in the case where F = 1.1 (FSI C) than where F = 0.5 (FSI B), even with low amplitude of vibration. The transition frequency did not have much effect on the vibration frequency of the foil, especially when the frequency ratio was $F = 0.5$ (FSI A and B). Moreover, no transition frequency was observed on the vibrations of FSI A, due to its higher rigidity. The frequency ratio F = 1.1 (FSI C) induced a multi-scaled frequency response due to the enhanced interaction between transition and pitch oscillation. Some similarities with a previous experimental study were suggested. A nonlinear coupling between the torsional mode of the hydrofoil and the transition process may occurs.

As it is a purely numerical study, it has to be noted that we can’t state that the investigated physic is not free from numerical effects. For instance, the natural transition can be influenced by numerical instabilities upstream, and the strong assumptions on the boundary conditions (i.e. periodic boundary condition in spanwise direction and reduced DNS domain) can somehow change the behaviour of the natural transition. Hence, more experimental and numerical works are needed to confirm the main conclusions of this thesis.

Perspectives

In order to end up this thesis work, we are stating some perspective. It is divided into three research areas.

Experimental works

One of the main contribution of this thesis work is the observation of change in the boundary layer regime and wall pressures behaviour due to vibration, in particular when the frequency ratio is close to 1 ($F = 1.1$), where the hydrofoil's vibration seems to be affected by the flow. This is the evidence of a transition induced vibration phenomenon. However, a direct experimental observation is required to confirm it. For technical reasons, it is not possible to experimentally measure both the wall pressures (by using piezoelectric transducers), and the vibrations/deformations of a flexible, plastic hydrofoil. We believe that an experimental setup, based on aeroelastic studies could be designed. It would consist of a rigid hydrofoil fixed on both sides of a water/wind tunnel test section by a system of torsional spring and dampers, which properties are set to reproduce small amplitudes vibrations seen in this thesis work. The vibrations can hence be fully controlled, then measured by using Laser Doppler Vibrometry, and correlated with direct measurement of the pitch at the elastic axis. This setup could be also designed together with wall pressures transducers, which appears to be crucial to investigate the effect of transition induced vibration on the hydrodynamic loading.

Numerical works

Although the effect of small amplitude vibration on the transition behavior has been clearly observed in this thesis work, more research is needed, in particular to characterize the fluid structure interaction effects. To obtain a complete map of the change in boundary layer transition mechanism as function of the amplitude and frequency of the pitch oscillation (such as the one shown in Figure 1.1 obtained in the work of PRASANTH and MITTAL, 2007 for the VIV on a cylinder), an extension of the parametric study is necessary. It seems important to perform more simulations near $F = 1$ and for different reduced amplitude A_θ to determine in which condition(s) the system can be submitted to lock-in. Also, the current developed 1 DOF-DNS model can be extended by including the effect of heave motion, and/or extended to a 3D simulation, which could corresponds to the experimental configuration of the measurements performed at IRENav, by using the generalized bending and torsional shape functions. Finally, a higher Reynolds number case can be considered to confirm the experimental behavior analyzed in Ducoin et al., 2012.

Applications

As a mid to long term perspective, this research work can provide a reference data set to develop flexible marine propellers. This includes the prediction of laminar to turbulent transition along the blades, and to take into account the full effect of flexibility on the boundary layer flow on the blades, including the change in regimes and the interaction with turbulence. A preliminary work has been published by our research team at LHEEA (Jing and Ducoin, 2020) on the boundary layer transitional flow on a full rigid propeller blade, by using DNS with Nek5000 (see, Figure 5.35). The developed FSI model can hence be extended to this 3D case in the future to take into account for the flexibility. As the computational effort is at least one order of magnitude larger than the simulation conducted in this thesis, it would requires activating a LES (Large Eddy Simulation) model in Nek5000, which has been already tested on a wind turbine blade, but still needing further improvements.

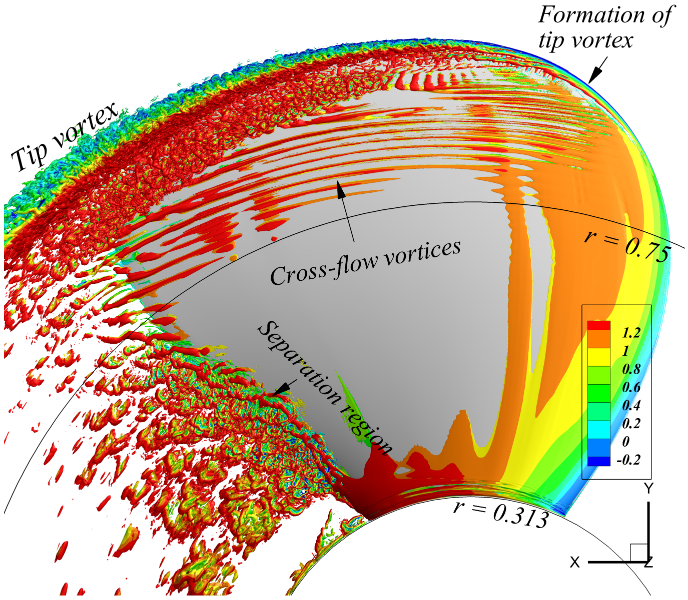

FIGURE 5.35: Iso-surface of the λ_2 criterion on suction side, colored by velocity in Z-direction on a marine propeller blade, Jing and Ducoin, 2020

Finally, the DNS data set obtain on transition induced vibration could be implemented in the hydrodynamic models based on transitional URANS or hybrid RANS/LES calculations currently used in the commercial CFD codes for engineering applications

Appendix A

Synthetic Turbulence

The following equations, figures and algorithms are taken from Davidson, 2015. The fluctuating velocity field is written as function of N random Fourier modes:

$$u_i'(x_j) = 2\sum_{n=1}^{N} \hat{u}^n \cos\left(\kappa_j^n x_j + \psi^n\right)\sigma_i^n \tag{A.1}$$

where $\hat{u}^n$ is the amplitude of velocity fluctuations, ψ^n is the phase of the Fourier mode n and σ_i^n is the direction of the Fourier mode n. The synthesized turbulence at one time step is generated as shown in the Algorithm 2.

$$E(\kappa) = \alpha \frac{u_{rms}^2}{\kappa_e} \frac{(\kappa/\kappa_e)^4}{\left[1+(\kappa/\kappa_e)^2\right]^{17/6}} e^{\left[-2(\kappa/\kappa_\eta)^2\right]} \tag{A.2}$$

where $\kappa = (\kappa_i \kappa_i)^{1/2}$ and $\kappa_\eta = \varepsilon^{1/4}\nu^{-3/4}$

$p(\varphi^n) = 1/(2n)$	$0 \le \varphi^n \le 2\pi$
$p(\psi^n) = 1/(2n)$	$0 \le \psi^n \le 2\pi$
$p(\theta^n) = 1/2\sin(\theta)$	$0 \le \theta^n \le \pi$
$p(\alpha^n) = 1/(2\pi)$	$0 \le \alpha^n \le 2\pi$

TABLE A.1: Probability distributions of the random angles and variables(φ^n, α^n, ψ^n and θ^n)

Algorithm 1 Algorithm to generate isotropic inlet turbulence

```
Generate random angles $\varphi^n, \alpha^n$ and $\theta^n$ for each Fourier mode n along with random phase $\psi^n$. Table ?? sets the probability and its range for each angles and phase.
Define the wave numbers as follows based on the given mesh resolution
    $\kappa_{max} = 2\pi/(2\Delta); \kappa_l = \kappa_e/p; \kappa_e = \alpha 9\pi/(55L_t)$
    where $\kappa_{max}$ is the highest wave number, $\kappa_l$ is the lowest wave number, $\Delta$ is the mesh spacing, $L_t$ is the turbulent length scale, $\alpha = 1.453$ and p is taken as 2 to make maximum scales bigger than the p of $\kappa_e$.
Divide the wavenumber space, $\kappa_{max}$ -$\kappa_1$, into N modes with equally large and of size $\Delta\kappa$.
Compute the wave number vector ($\kappa_j^n$) using Fig.A.1.
Unit vectors, $\sigma_i^n$ and $\kappa_j^n$ should be orthogonal in order to maintain the continuity. In addition to that, the $\sigma_3^n$ is randomly selected to be parallel with $\kappa_i^n$ and $\alpha^n$ as shown in Fig.A.2.
The amplitude of velocity fluctuations $(\hat{u}^n)$ of each mode can be derived from $\hat{u}^n = \left(E\left(|\, k_j^n \,|\right)\Delta k\right)^{1/2}$ where $E(k)$ is the modified Von Karman spectrum (see Eq.A.2 and Fig.A.3)
Now using all the parameters such as $\hat{u}^n$, $\kappa_j^n$, $\sigma_i^n$ and $\psi^n$ we can compute the velocity fluctuations using Eq.A.1.
```

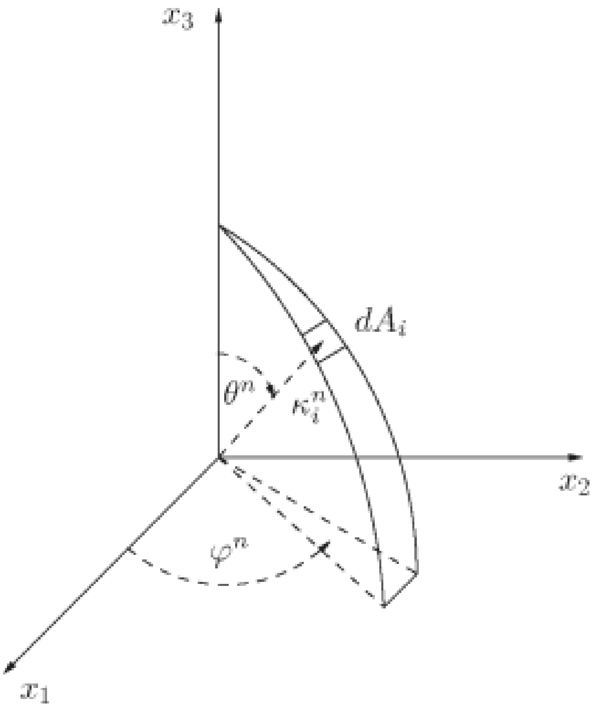

FIGURE A.1: The relation of φ^n, θ^n with respect to the wave number on a small area of dA_i on the surface of a sphere, Davidson, 2015

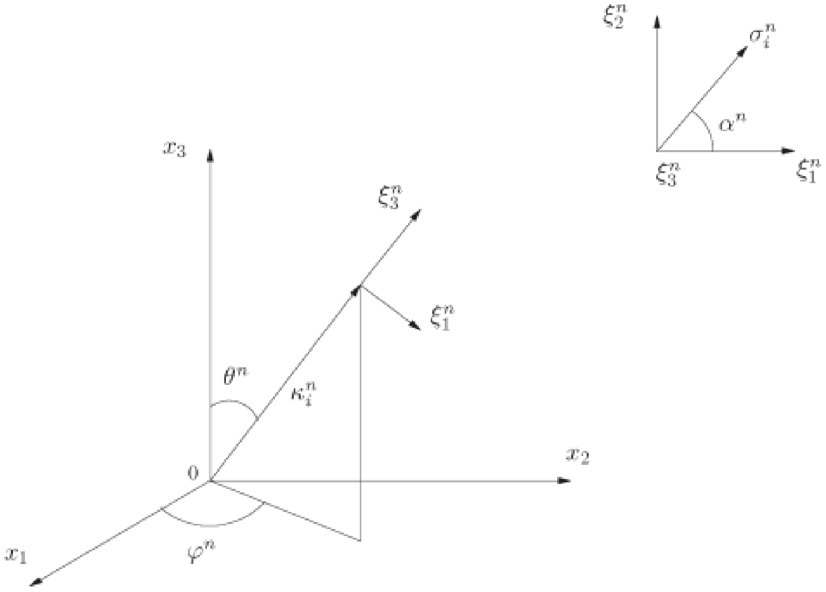

FIGURE A.2: The relation of α^n, ψ^n and θ^n with respect to the wave number and the unit velocity vector σ_i^n, Davidson, 2015

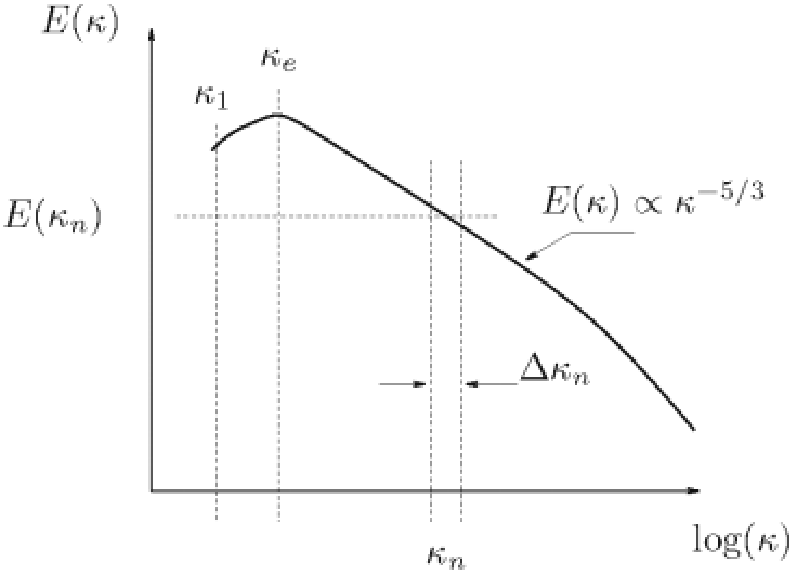

FIGURE A.3: Modified von Kármán spectrum, Davidson, 2015

The generated fluctuating velocity field is has no correlation with each other, i.e they are independent which in not the reality. So a correlation in time has to be calculated. The new fluctuating velocity fields, u'_x,u'_y,u'_z, are :

$$
\begin{aligned}
(u_x{}')^i &= a\left(u'_x\right)^{i-1} + b\left(u'_x\right)^i \\
(u_y{}')^i &= a\left(u'_y\right)^{i-1} + b\left(u'_y\right)^i \\
(u_z{}')^i &= a\left(u'_z\right)^{i-1} + b\left(u'_z\right)^i
\end{aligned}
\tag{A.3}
$$

where i is the time step and $a = exp(\text{-}\Delta t/T)$ where $\Delta t/T$ is the ratio of time step to the current time. The another coefficient $b = (1\text{-}a^2)^{0.5}$. Finally, the inlet turbulence can be integrated in to the inlet velocity as shown in Eq.A.4.

$$\bar{u} = U_{in} + u'_{in} \tag{A.4}$$

where $\bar{u}$ is the resultant inlet velocity, U_{in} is the actual inlet velocity and u'_{in} is the velocity fluctuations (inlet turbulence).

Appendix B

Structural parameters of NACA66

Let us a consider a hydrofoil of rotational degree of freedom in 2D. It is important to remark that, in 3D it is a section of a cantilevered hydrofoil. The 3D structural parameters are extrapolated using a shape function g(s) from the 2D structural parameters which is shown in the Table B.1. The equation of shape function is shown below (see Eq. B.1) and the graph is shown in Fig. 2.5. This normalized shape function is integrated from the clamped end to desired length of the span to calculate the s_{gg} and multiplied it with the 2D structural quantity to obtain the 3D parameters. More details about this approach can be found in Ducoin and Young, 2013; Akcabay et al., 2014; Chae et al., 2017.

$$g(s) = sin(\pi s/2) \tag{B.1}$$

$$s_{gg} = \int_0^s g(s)ds \tag{B.2}$$

TABLE B.1: The structural parameters of NACA6612 hydrofoil which is made of POM (polyacetate foil), Akcabay et al., 2014

Chord (c)	0.15m
Span (s)	0.191m
Max. Thickness	0.18m
$2-DMass(m'_s)$	2.94 kg/m
2-D Moment of Inertia (I'_α)	3.70 x 10^{-3} kg m
Torsion natural frequency in air (f^a_α)	361 Hz
3-D Mass (m_s)	0.148 kg
3-D Moment of Inertia I_α	3.37 x 10^{-4} kg m^2
3-D Torsion Stiffness K_α	1729 N m
3-D Damping factor of torsion (D_{factor})	0.04

The generalized structural parameters of the flexible NACA6612 hydrofoil can be written as :

$$I_\alpha = \int_0^s I'_\alpha (g(s))^2 dz = I'_\alpha \int_0^s (g(z))^2 dz = I'_\alpha s_{gg} \tag{B.3}$$

$$K_\alpha = \int_0^s G_s J' \left(\frac{dg(s)}{ds} \right)^2 ds = I_\alpha \left(2\pi f^a_\alpha \right)^2 = I'_\alpha \mathrm{s_{gg}} \left(2\pi f^a_\alpha \right)^2 \tag{B.4}$$

$$C_\alpha = \int_0^s C'_\alpha (g(s))^2 ds = 2D_{factor} I_\alpha \left(2\pi f^a_\alpha \right) = 2D_{factor} I'_\alpha \left(2\pi f^a_\alpha \right) s_{gg} \tag{B.5}$$

$$T_{EA} = T'_{EA} s_{gg} \tag{B.6}$$

where T'_{EA} is the torque imposed on the solid by the fluid with respect to the elastic axis in 2-D where as T_{EA} is in 3-D. G_s is the torsional rigidity of the hydrofoil; J' is the torsion constant of the hydrofoil cross section along elastic axis. All the structural parameters with (″ ′ ″) represent the structural quantity in 2-D (per unit span).

Bibliography

Açıkel, Halil Hakan and Mustafa Serdar Genç (2018). “Control of laminar separation bubble over wind turbine airfoil using partial flexibility on suction surface”. In: *Energy* 165, pp. 176 –190.

Akcabay, Deniz Tolga et al. (2014). “Cavity induced vibration of flexible hydrofoils”. In: *Journal of Fluids and Structures* 49, pp. 463 –484.

Andersen, Poul, Jens Julius kappel, and Eugen Spangenberg (2009). “Aspects of Propeller Developements for a Submarine”. In: pp. 551–561.

Arab, Fatiha et al. (Nov. 2019). “Morphing Hydrofoil Model Driven by Compliant Composite Structure and Internal Pressure”. In: *Journal of Marine Science and Engineering* 7, p. 423. DOI: `10.3390/jmse7120423`.

Barnes, Caleb J. and Miguel Visbal (2016). “High-Fidelity LES Simulations of Self-Sustained Pitching Oscillations on a NACA0012 Airfoil at Transitional Reynolds Numbers”. In: *54th AIAA Aerospace Sciences Meeting*.

Barnes, Caleb J. and Miguel R. Visbal (2018). “On the role of flow transition in laminar separation flutter”. In: *Journal of Fluids and Structures* 77, pp. 213 –230.

— (2019). “Stiffness effects on laminar separation flutter”. In: *Journal of Fluids and Structures* 91, p. 102767.

Carlton, J.S. (2012). “Chapter 3 - Propeller Geometry”. In: *Marine Propellers and Propulsion (Third Edition)*. Ed. by J.S. Carlton. Third Edition. Oxford: Butterworth-Heinemann, pp. 29 –46.

Chae, Eun Jung, Deniz Tolga Akcabay, and Yin Lu Young (2017). “Influence of flow-induced bend–twist coupling on the natural vibration responses of flexible hydrofoils”. In: *Journal of Fluids and Structures* 69, pp. 323 –340.

Davidson, Lars (2015). “Fluid Mechanics, turbulent flow and turbulence modelling”. In:

de Langre, E. (2001). “Fluides et Solides”. In: *Editions de l’Ecole Polytechnique, First Edition*.

De Nayer, G., M. Breuer, and J.N. Wood (2020). “Numerical investigations on the dynamic behavior of a 2-DOF airfoil in the transitional Re number regime based on fully coupled simulations relying on an eddy-resolving technique”. In: *International Journal of Heat and Fluid Flow* 85, p. 108631.

Delafin, P.L., F. Deniset, and J.A. Astolfi (2014). “Effect of the laminar separation bubble induced transition on the hydrodynamic performance of a hydrofoil”. In: *European Journal of Mechanics - B/Fluids* 46, pp. 190 –200.

Deville, M. O., P. F. Fischer, and E. H. Mund (2002). “Frontmatter”. In: Cambridge Monographs on Applied and Computational Mathematics, pp. i–viii.

Ducoin, A. (2018). “Cours d’interaction fluide structure”. In: *Centrale Nantes, option OCEAN*.

Ducoin, A. and J.A. Astolfi (2019). “Wall-pressure fluctuations of laminar separation bubble based on direct numerical simulation and experiments over a hydrofoil at Re = 450,000”. In: *European Journal of Mechanics - B/Fluids* 76, pp. 132 –144. ISSN: 0997-7546. DOI: `https://doi.org/10.1016/j.euromechflu.2019.02.001`. URL: `http://www.sciencedirect.com/science/article/pii/S0997754618302784`.

Ducoin, A., J.-Ch. Loiseau, and J.-Ch. Robinet (2016). “Numerical investigation of the interaction between laminar to turbulent transition and the wake of an airfoil”. In: *European Journal of Mechanics - B/Fluids* 57, pp. 231 –248.

Ducoin, Antoine and Yin L. Young (2013). “Hydroelastic response and stability of a hydrofoil in viscous flow”. In: *Journal of Fluids and Structures* 38, pp. 40 –57.

Ducoin, Antoine et al. (2009). “Computational and experimental investigation of flow over a transient pitching hydrofoil”. In: *European Journal of Mechanics - B/Fluids* 28.6, pp. 728 –743.

Ducoin, Antoine, Jacques André Astolfi, and Marie-Laure Gobert (2012). “An experimental study of boundary-layer transition induced vibrations on a hydrofoil”. In: *Journal of Fluids and Structures* 32, pp. 37 –51.

Durand, Mathieu (Oct. 2012). “Light and flexible Fluid/Structure Interaction, application to sailing boats”. In: URL: `https://hal.archives-ouvertes.fr/tel-01203748`.

Ezkurra, Mikel et al. (Apr. 2018). “Analysis of One-Way and Two-Way FSI Approaches to Characterise the Flow Regime and the Mechanical Behaviour during Closing Manoeuvring Operation of a Butterfly Valve”. In: *World Academy of Science, Engineering and Technology, International Journal of Mechanical and Materials Engineering* 12, pp. 313–319.

Farhat, C. and M. Lesoinne (2000). “Two efficient staggered algorithms for the serial and parallel solution of three-dimensional nonlinear transient aeroelastic problems”. In: *Computer Methods in Applied Mechanics and Engineering* 182.3, pp. 499 –515.

Fischer, Paul, Martin Schmitt, and Ananias Tomboulides (2017). “Recent Developments in Spectral Element Simulations of Moving-Domain Problems”. In: *Fields Institute Communications*, pp. 213–244.

Fischer, Paul F (1997). “An Overlapping Schwarz Method for Spectral Element Solution of the Incompressible Navier–Stokes Equations”. In: *Journal of Computational Physics* 133.1, pp. 84 –101.

Galbraith, Marshall and Miguel Visbal (2009). “Implicit Large Eddy Simulation of Low Reynolds Number Flow Past the SD7003 Airfoil”. In: *46th AIAA Aerospace Sciences Meeting and Exhibit*. DOI: `10.2514/6.2008-225`. eprint: `https://arc.aiaa.org/doi/abs/10.2514/6.2008-225`. URL: `https://arc.aiaa.org/doi/abs/10.2514/6.2008-225`.

Genç, M. Serdar, İlyas Karasu, and H. Hakan Açıkel (2012). “An experimental study on aerodynamics of NACA2415 aerofoil at low Re numbers”. In: *Experimental Thermal and Fluid Science* 39, pp. 252 –264.

Gordnier, R.E. (2009). “High fidelity computational simulation of a membrane wing airfoil”. In: *Journal of Fluids and Structures* 25.5, pp. 897 –917.

GOVARDHAN, R. and C. H. K. WILLIAMSON (2000). “Modes of vortex formation and frequency response of a freely vibrating cylinder”. In: *Journal of Fluid Mechanics* 420, pp. 85–130.

Ho, Lee (Aug. 2005). “A Legendre spectral element method for simulation of incompressible unsteady free-surface flows”. In:

Hosseini, S.M. et al. (2016). “Direct numerical simulation of the flow around a wing section at moderate Reynolds number”. In: *International Journal of Heat and Fluid Flow* 61, pp. 117 –128.

Hübner, Björn, Elmar Walhorn, and Dieter Dinkler (2004). “A monolithic approach to fluid–structure interaction using space–time finite elements”. In: *Computer Methods in Applied Mechanics and Engineering* 193.23, pp. 2087 –2104.

Idelsohn, Sergio R. and Eugenio Oñate (2006). “To mesh or not to mesh. That is the question...” In: *Computer Methods in Applied Mechanics and Engineering* 195.37, pp. 4681 –4696.

Jing, Z. and A. Ducoin (2020). “Direct numerical simulation and stability analysis of the transitional boundary layer on a marine propeller blade”. In: *Physics of Fluids* 32.12, p. 124102. DOI: `10.1063/5.0030070`. eprint: `https://doi.org/10.1063/5.0030070`. URL: `https://doi.org/10.1063/5.0030070`.

Jumper, E.J., S.J. Schreck, and R.L. Dimmick (1987). “Lift-curve characteristics for an airfoil pitching at constant rate”. In: *Journal of Aircraft* 24.10, pp. 680–687. DOI: `10.2514/3.45507`. eprint: `https://doi.org/10.2514/3.45507`. URL: `https://doi.org/10.2514/3.45507`.

Kanchi, Harish and Arif Masud (2007). “A 3D adaptive mesh moving scheme”. In: *International Journal for Numerical Methods in Fluids* 54.6-8, pp. 923–944. DOI: `10.1002/fld.1512`. eprint: `https://onlinelibrary.wiley.com/doi/pdf/10.1002/`

fld.1512. URL: https://onlinelibrary.wiley.com/doi/abs/10.1002/fld.1512.

KARMAN, TH. VON (1937). "The Fundamentals of the Statistical Theory of Turbulence". In: *Journal of the Aeronautical Sciences* 4.4, pp. 131–138. DOI: 10.2514/8.350. eprint: https://doi.org/10.2514/8.350. URL: https://doi.org/10.2514/8.350.

Kenneth and Kenneth Jansen (1995). "Preliminary large-eddy simulations of flow around a NACA 4412 airfoil using unstructured grids". In:

Kim, Woojin and Haecheon Choi (2019). "Immersed boundary methods for fluid-structure interaction: A review". In: *International Journal of Heat and Fluid Flow* 75, pp. 301 –309.

Koopmann, G. H. (1967). "The vortex wakes of vibrating cylinders at low Reynolds numbers". In: *Journal of Fluid Mechanics* 28.3, 501–512. DOI: 10.1017/S0022112067002253.

KREISS, HEINZ-OTTO and JOSEPH OLIGER (1972). "Comparison of accurate methods for the integration of hyperbolic equations". In: *Tellus* 24.3, pp. 199–215. DOI: 10.1111/j.2153-3490.1972.tb01547.x. eprint: https://onlinelibrary.wiley.com/doi/pdf/10.1111/j.2153-3490.1972.tb01547.x. URL: https://onlinelibrary.wiley.com/doi/abs/10.1111/j.2153-3490.1972.tb01547.x.

Lapointe, S. and G. Dumas (2011). "Large eddy simulations of self-sustained oscillations of a naca0012 at transitional reynolds number". In: *Conference Paper, CASI AERO11*.

LEE, T. and P. GERONTAKOS (2004). "Investigation of flow over an oscillating airfoil". In: *Journal of Fluid Mechanics* 512.

Leroyer, A. and M. Visonneau (2005). "Numerical methods for RANSE simulations of a self-propelled fish-like body". In: *Journal of Fluids and Structures* 20.7, pp. 975 –991.

Lian, Yongsheng and Wei Shyy (2007). "Laminar-Turbulent Transition of a Low Reynolds Number Rigid or Flexible Airfoil". In: *AIAA Journal* 45.7, pp. 1501–1513.

Lin, Ching-Chieh, Ya-Jung Lee, and Chu-Sung Hung (2009). "Optimization and experiment of composite marine propellers". In: *Composite Structures* 89.2, pp. 206 –215.

Liu, Zhanke and Yin L. Young (2009). "Utilization of bend–twist coupling for performance enhancement of composite marine propellers". In: *Journal of Fluids and Structures* 25.6, pp. 1102 –1116.

Lohner, R. and C. Yang (1996). "Improved ALE mesh velocities for moving bodies". In: *Commun.Numer.Metch.Engng* 12.10, pp. 599–608.

Lombardi, M., N. Parolini, and A. Quarteroni (2013). “Radial basis functions for inter-grid interpolation and mesh motion in FSI problems”. In: *Computer Methods in Applied Mechanics and Engineering* 256, pp. 117 –131.

Maday, Y., Anthony T. Patera, and Einar M. Rnquist (1990). “An Operator-integration-factor splitting method for time-dependent problems: Application to incompressible fluid flow”. In: *Journal of Scientific Computing* 5.4, pp. 263–292.

Masud, Arif and Thomas J.R. Hughes (1997). “A space-time Galerkin/least-squares finite element formulation of the Navier-Stokes equations for moving domain problems”. In: *Computer Methods in Applied Mechanics and Engineering* 146.1, pp. 91 –126.

McCROSKEY, W.J. and J.J. PHILIPPE (1975). “Unsteady Viscous Flow on Oscillating Airfoils”. In: *AIAA Journal* 13.1, pp. 71–79. DOI: `10.2514/3.49633`. eprint: `https://doi.org/10.2514/3.49633`. URL: `https://doi.org/10.2514/3.49633`.

Motley, Michael R. and Yin L. Young (2011). “Performance-based design and analysis of flexible composite propulsors”. In: *Journal of Fluids and Structures* 27.8, pp. 1310 –1325.

Nati, A. et al. (2015). “Dynamic pitching effect on a laminar separation bubble”. In: *Experiments in Fluids* 56.9, p. 172.

Negi, P.S. et al. (2018). “Unsteady aerodynamic effects in small-amplitude pitch oscillations of an airfoil”. In: *International Journal of Heat and Fluid Flow* 71, pp. 378 –391.

Nobari, M.R.H. and H. Naderan (2006). “A numerical study of flow past a cylinder with cross flow and inline oscillation”. In: *Computers & Fluids* 35.4, pp. 393 –415.

Offermans, Nicolas et al. (2016). “On the Strong Scaling of the Spectral Element Solver Nek5000 on Petascale Systems”. In: EASC ’16. DOI: `10.1145/2938615.2938617`. URL: `https://doi.org/10.1145/2938615.2938617`.

Oliveira, S.P. and G. Seriani (2011). “Effect of Element Distortion on the Numerical Dispersion of Spectral Element Methods”. In: *Communications in Computational Physics* 9.4, pp. 937–958.

O’Meara, M. M. and T. J. Mueller (1987). “Laminar separation bubble characteristics on an airfoil at low Reynolds numbers”. In: *AIAA Journal* 25.8, pp. 1033–1041. DOI: `10.2514/3.9739`. eprint: `https://doi.org/10.2514/3.9739`. URL: `https://doi.org/10.2514/3.9739`.

Orszag, Steven A (1980). “Spectral methods for problems in complex geometries”. In: *Journal of Computational Physics* 37.1, pp. 70 –92.

Pascazio, M. et al. (1996). “Unsteady boundary-layer measurement on oscillating airfoils - Transition and separation phenomena in pitching motion”. In: *34th Aerospace Sciences Meeting and Exhibit*.

Patera, Anthony T (1984). “A spectral element method for fluid dynamics: Laminar flow in a channel expansion”. In: *Journal of Computational Physics* 54.3, pp. 468 –488. ISSN: 0021-9991. DOI: `https://doi.org/10.1016/0021-9991(84)90128-1`. URL: `http://www.sciencedirect.com/science/article/pii/0021999184901281`.

Paul F. Fischer, James W. Lottes and Stefan G. Kerkemeier (2008). “nek5000 Web page”. In: http://nek5000.mcs.anl.gov.

Pauley, Laura L., Parviz Moin, and William C. Reynolds (1990). “The structure of two-dimensional separation”. In: *Journal of Fluid Mechanics* 220, 397–411. DOI: `10.1017/S0022112090003317`.

Pernod, Laetitia et al. (2019). “Experimental and numerical investigation of the fluid-structure interaction on a flexible composite hydrofoil under viscous flows”. In: *Ocean Engineering* 194, p. 106647.

Piperno, Serge and Charbel Farhat (2001). “Partitioned procedures for the transient solution of coupled aeroelastic problems – Part II: energy transfer analysis and three-dimensional applications”. In: *Computer Methods in Applied Mechanics and Engineering* 190.24, pp. 3147 –3170.

Piperno, Serge, Charbel Farhat, and Bernard Larrouturou (1995). “Partitioned procedures for the transient solution of coupled aroelastic problems Part I: Model problem, theory and two-dimensional application”. In: *Computer Methods in Applied Mechanics and Engineering* 124.1, pp. 79 –112.

Placzek, Antoine, Jean-François Sigrist, and Aziz Hamdouni (2009). “Numerical simulation of an oscillating cylinder in a cross-flow at low Reynolds number: Forced and free oscillations”. In: *Computers & Fluids* 38.1, pp. 80 –100.

Pluciński, M.M., Yin Lu Young, and Zhanke Liu (Jan. 2007). “Optimization of a self-twisting composite marine propeller using genetic algorithms”. In: *ICCM International Conferences on Composite Materials*.

Poirel, D. and F. Mendes (2014a). “Experimental Small-Amplitude Self-Sustained Pitch–Heave Oscillations at Transitional Reynolds Numbers”. In: *AIAA Journal* 52.8, pp. 1581–1590.

— (2014b). “Experimental Small-Amplitude Self-Sustained Pitch–Heave Oscillations at Transitional Reynolds Numbers”. In: *AIAA Journal* 52.8, pp. 1581–1590. DOI: `10.2514/1.J052541`. eprint: `https://doi.org/10.2514/1.J052541`. URL: `https://doi.org/10.2514/1.J052541`.

Poirel, D. and W. Yuan (2010). “Aerodynamics of laminar separation flutter at a transitional Reynolds number”. In: *Journal of Fluids and Structures* 26.7, pp. 1174 –1194.

Poirel, D., Y. Harris, and A. Benaissa (2008). "Self-sustained aeroelastic oscillations of a NACA0012 airfoil at low-to-moderate Reynolds numbers". In: *Journal of Fluids and Structures* 24.5, pp. 700 –719.

Poirel, D., V. Métivier, and G. Dumas (2011). "Computational aeroelastic simulations of self-sustained pitch oscillations of a NACA0012 at transitional Reynolds numbers". In: *Journal of Fluids and Structures* 27.8, pp. 1262 –1277.

PRASANTH, T. K. and S. MITTAL (2007). "Vortex-induced vibrations of a circular cylinder at low Reynolds numbers". In: *Journal of Fluid Mechanics* 594, pp. 463–491.

Rahromostaqim, M., A. Posa, and E. Balaras (2016). "Numerical Investigation of the Performance of Pitching Airfoils at High Amplitudes". In: *AIAA Journal* 54.8, pp. 2221–2232.

Rhie, C. M. and W. L. Chow (1983). "Numerical study of the turbulent flow past an airfoil with trailing edge separation". In: *AIAA Journal* 21.11, pp. 1525–1532. DOI: `10.2514/3.8284`. eprint: `https://doi.org/10.2514/3.8284`. URL: `https://doi.org/10.2514/3.8284`.

Shan, Hua, Li Jiang, and Chaoqun Liu (2005). "Direct numerical simulation of flow separation around a NACA 0012 airfoil". In: *Computers & Fluids* 34.9, pp. 1096 –1114.

Sharma, S. and A. Ducoin (2018). "Direct numerical simulation of the effect of inlet isotropic turbulence on centrifugal instabilities over a curved wall". In: *Computers & Fluids* 174, pp. 1 –13.

Sotiropoulos, Fotis and Xiaolei Yang (2014). "Immersed boundary methods for simulating fluid–structure interaction". In: *Progress in Aerospace Sciences* 65, pp. 1 – 21.

Tani, Itiro (1964). "Low-speed flows involving bubble separations". In: *Progress in Aerospace Sciences* 5, pp. 70 –103. ISSN: 0376-0421. DOI: `https://doi.org/10.1016/0376-0421(64)90004-1`. URL: `http://www.sciencedirect.com/science/article/pii/0376042164900041`.

Theodorsen, Theodore (1934). "General Theory of Aerodynamic Instability and the Mechanism of Flutter". In: *University of North Texas Libraries, UNT Digital Library*.

Tufo, H.M and P.F Fischer (2001). "Fast Parallel Direct Solvers for Coarse Grid Problems". In: *Journal of Parallel and Distributed Computing* 61.2, pp. 151 –177.

Tumkur, Ravi Kumar R. et al. (2013). "Computational study of vortex-induced vibration of a sprung rigid circular cylinder with a strongly nonlinear internal attachment". In: *Journal of Fluids and Structures* 40, pp. 214 –232.

Vinuesa, Ricardo et al. (May 2018). “Turbulent boundary layers around wing sections up to Rec = 1,000,000”. In: *International Journal of Heat and Fluid Flow* 72, pp. 86–99. DOI: `10.1016/j.ijheatfluidflow.2018.04.017`.

Virot, Emmanuel, Xavier Amandolese, and Pascal Hémon (2016). “Coupling between a flag and a spring-mass oscillator”. In: *Journal of Fluids and Structures* 65, pp. 447 –454. ISSN: 0889-9746. DOI: `https://doi.org/10.1016/j.jfluidstructs.2016.06.014`. URL: `http://www.sciencedirect.com/science/article/pii/S0889974615300505`.

Visbal, Miguel R. (2014). “Analysis of the Onset of Dynamic Stall Using High-Fidelity Large-Eddy Simulations”. In: *52nd Aerospace Sciences Meeting*. DOI: `10.2514/6.2014-0591`. eprint: `https://arc.aiaa.org/doi/pdf/10.2514/6.2014-0591`. URL: `https://arc.aiaa.org/doi/abs/10.2514/6.2014-0591`.

Williamson, C.H.K. and A. Roshko (1988). “Vortex formation in the wake of an oscillating cylinder”. In: *Journal of Fluids and Structures* 2, 355–381.

W.N.W. Hussin F.N. Harun, M.H. Mohd and M.A.A. Rahman (2017). “Analytical modelling prediction by using wake oscillator model for vortex induced vibrations”. In: *Journal of mechanical engineerin and sciences* 11.4, pp. 3116–3128.

Young, Yin L. et al. (2018). “Load-dependent bend-twist coupling effects on the steady-state hydroelastic response of composite hydrofoils”. In: *Composite Structures* 189, pp. 398 –418. ISSN: 0263-8223. DOI: `https://doi.org/10.1016/j.compstruct.2017.09.112`. URL: `http://www.sciencedirect.com/science/article/pii/S0263822317317130`.

Young, Yin Lu, Eun Jung Chae, and Deniz Tolga Akcabay (2012a). “Hybrid algorithm for modeling of fluid-structure interaction in incompressible, viscous flows”. In: *Acta Mechanica Sinica* 28.4, pp. 1030–1041.

— (2012b). “Hybrid algorithm for modeling of fluid-structure interaction in incompressible, viscous flows”. In: *Acta Mechanica Sinica* 28.4, pp. 1030–1041.

Young, Y.L. (2008). “Fluid–structure interaction analysis of flexible composite marine propellers”. In: *Journal of Fluids and Structures* 24.6, pp. 799 –818.

Yuan, Weixing, Dominique Poirel, and Baoyuan Wang (2013). “Simulations of Pitch–Heave Limit-Cycle Oscillations at a Transitional Reynolds Number”. In: *AIAA Journal* 51.7, pp. 1716–1732. DOI: `10.2514/1.J052225`. eprint: `https://doi.org/10.2514/1.J052225`. URL: `https://doi.org/10.2514/1.J052225`.

Yuan, Weixing et al. (2015). “Effect of Freestream Turbulence on Airfoil Limit-Cycle Oscillations at Transitional Reynolds Numbers”. In: *Journal of Aircraft* 52.4, pp. 1214–1225.

Yvin, C. et al. (2018a). “Added mass evaluation with a finite-volume solver for applications in fluid–structure interaction problems solved with co-simulation”. In: *Journal of Fluids and Structures* 81, pp. 528 –546.

— (2018b). “Added mass evaluation with a finite-volume solver for applications in fluid–structure interaction problems solved with co-simulation”. In: *Journal of Fluids and Structures* 81, pp. 528–546.

Zarruk, Gustavo A. et al. (2014). “Experimental study of the steady fluid–structure interaction of flexible hydrofoils”. In: *Journal of Fluids and Structures* 51, pp. 326 –343.

Zhang, Wei and Ravi Samtaney (2016). “Assessment of spanwise domain size effect on the transitional flow past an airfoil”. In: *Computers & Fluids* 124, pp. 39 –53.

CENTRALE
NANTES

Titre : **Simulation Numérique Directe de la Transition Laminaire Turbulent sur un Hydrofoil Flexible**

Mots clés : Hydrofoil, Transition, DNS, 1 Degré de liberté, IFS, Ondes TS

Résumé : Dans cette thèse, les vibrations induites par la transition laminaire turbulent sur un hydrofoil NACA66 à un nombre de Reynolds Re=450 000 sont étudiées. Des simulations numériques directes (DNS) sont mises en place afin de prédire un écoulement de couche limite incompressible, qui sont couplées avec un hydrofoil en mouvement de rotation libre. Ainsi, un couplage fluide structure de type implicite est développé dans le code Nek5000. Du fait du caractère très amont de cette méthode, de nombreux cas de validations sont effectués, menant au cas des vibrations induites par la transition. Ensuite, les recherches se basent sur une étude paramétrique, consistant à mener des cas d'oscillation forcées (rotations imposées) et d'oscillations libres (mouvements du au chargement induit par l'écoulement). Cela permet d'analyser finement les interactions entre les vibrations de l'hydrofoil et son écoulement de couche limite transitionnel. A ce titre, de nouveaux paramètres adimensionnels sont mis en place, permettant de caractériser les interactions fluides structures sur ce type d'écoulement. Du point de vue de l'écoulement de couche limite, il a été observé que la localisation du point de transition est proportionnelle à l'amplitude des mouvements de rotation de l'hydrofoil, de sa vitesse de rotation ainsi que du ratio fréquentiel entre la fréquence Naturelle du système et la fréquence de lâchers tourbillonnaire liée à la transition. La génération d'ondes TS (premier pas vers la transition de couche limite) est aussi sensible aux vibrations. Ensuite, les résultats ont montré que les structures cohérentes formées en aval de ces ondes TS, subissent une évolution spatiale dont la longueur d'onde transversale est proportionnelle à l'épaisseur de déplacement de la couche limite. Le déplacement de la région transitionnelle vers le bord d'attaque tend à réduire les fluctuations de pressions périodiques liées à cette transition, tandis que de celle-ci devient plus étendue dans la direction de l'écoulement. Finalement, lorsque la fréquence naturelle de l'hydrofoil se rapproche de la fréquence de lâcher du bulbe (ratio fréquentiel proche de 1), il a été observé une réponse multi-fréquentielle, liée à une forte interaction entre la transition et les vibrations de l'hydrofoil. L'étude suggère que dans ce cas précis, les interactions fluides structures tendent à perturber le comportement spatio-temporel de la transition laminaire turbulent. Cette analyse doit être confirmée expérimentalement. Cependant ce phénomène a déjà été identifié lors d'une campagne de mesure menée en tunnel hydrodynamique à l'Institut de Recherche de l'École Navale (IRENav), à un nombre de Reynolds cependant plus élevé.

Title : **Direct Numerical Simulation of Transition Induced Vibration over a Flexible Hydrofoil Section**

Keywords : Hydrofoil, Transition, DNS, 1 Degree of Freedom, FSI, TS waves

Abstract: The laminar to turbulent transition induced vibration over a NACA66 hydrofoil at Re = 450000 is investigated in this thesis. DNS is used to simulate the 3D incompressible boundary layer flow, and it is coupled with a freely pitching hydrofoil. An implicit coupling is developed within the fluid solver Nek5000. A number of cases are performed to validate this method, which lead to study the transition induced vibration. Then, a parametric study consisting of two forced and three free oscillations allowed analyzing the interactions between the vibration and the boundary layer transitional flow. A set of specific non-dimensional parameters are set, which aim at characterize the fluid structure interactions in such flow regime. From the boundary layer flow analysis, it was observed that the spatial location of the transition point is proportional to the amplitude of pitch, velocity, and frequency ratio. The generation of TS waves (the first stage of laminar to turbulent transition) is also influenced by the vibrations. It was also observed that the span-wise wavelength of coherent structures (so called "hair-pin" structures" that form downstream of the TS waves) is proportional to the displacement thickness. The spatial advancement of the transition point reduces the amplitude of periodic pressure fluctuations in the transition regime. In addition, the length of the transition region is increased. Finally, a multi-scaled frequency response is observed due to the enhanced interaction between transition and pitch oscillation when the transition and natural frequencies are close to each other. The study suggests that in this case, the fluid structure interaction tends to disturb the spatio-temporal behavior of laminar to turbulent transition. Although it has to be confirmed, this phenomenon has already identified experimentally through measurements performed at the Naval Academy Research Institute (IRENav) in hydrodynamic tunnel for a higher Reynolds number case.